

Doctoral Dissertation

Electrochemical Properties and Applications of
Graphene Oxide

March 2015

Hikaru Tateishi

Graduate School of Science and Technology

KUMAMOTO UNIVERSITY

PREFACE

Graphene have been intensively researched to open up new devices in physical field thank to have unique electronic structure and electron transport capabilities. Graphene oxide (GO) prepared by exfoliating graphite oxide in solution had been studied as the precursor material of graphene and tried to obtain graphene by reducing it until a few years ago due to be able to easily synthesize in large scale. However, reduced GO (rGO) is different from intrinsic graphene and exist many defects and remained a little oxygen functional groups. GO and rGO exhibit various interesting chemical properties due to its heterogeneous chemical and electronic structures and chemists are increasingly drawn to GO and rGO.

In the present study, we focus on elucidation of electrochemical properties of GO and rGO. We take particular note of two electrochemical properties: (1) electrochemical capacitance properties and (2) oxygen reduction reaction (ORR) properties. rGO has attracted significant interest as an electrode material for electrochemical double layer capacitors due to its high electrical conductivity and high surface area. Also, rGO is covered with functional groups on the sheet surface and these functional groups work as a source of pseudocapitance. Thus, rGO has potential for electrode materials of electrochemical capacitor. As other properties, GO exhibit negative charge and hydrophilic property owing to many oxygen functional groups of sheet surface. GO can easily combine with other materials such as metal cation, metal complex, and hydrophilic nanomaterials. The hybrid materials after reduction lead up to development of new electrocatalytic materials. Moreover, multilayered GO film (GO paper) exhibits relatively high proton conduction. Applying GO paper to electrolyte, we developed two novel cells: (1) graphene oxide fuel cell (GOFC) and (2) graphene oxide lead battery (GOLB).

The thesis is composed of 7 chapters.

Chapter 1 narrates the general backgrounds, preparation method, properties, and

application of GO.

Chapter 2 presents the electrochemical properties of GO prepared by the new electrochemical method. We present a new electrochemical oxidation method for preparing GO, in which a high oxidation voltage is applied at the carbon electrode in pure water. This electrochemical oxidation method can be easily controlled oxidation degree. After electrochemical reduction of GO, the rGO has three electrochemical properties: high electrochemical capacitance, photoelectrochemical property, and electrocatalytic activity for ORR. These electrochemical properties of rGO are due to the CH defects and/or OH groups from rGO.

Chapter 3 presents the electrochemical capacitance of GO. We focus on the effects of the electrochemical oxidation/reduction cycle of GO on its composition and electrochemical capacitance. C=C bonds are produced from CH defects by the electrochemical re-oxidation of rGO, while COC bonds are produced from carbon materials by the first electrochemical oxidation. The electrochemical capacitance of rGO is increase with the electrochemical oxidation/reduction cycle because of the increase of the surface area of rGO. Moreover, we discuss effects of other reduction method on the electrochemical capacitance of GO by using of X-ray photoelectron spectroscopy. The electrochemical capacitance of rGO is increase with the ratio of CH defects.

Chapter 4 presents the electrocatalytic activity for ORR of GO. The novel iron phthalocyanine/GO (FePc/GO) hybrid is prepared by self-assembly. The FePc/rGO hybrid prepared by electrochemical reduction of FePc/GO hybrid exhibits excellent electrocatalytic activity for ORR compared with the commercial Pt/C catalysts in alkaline medium.

Chapter 5 presents the application of GO as an electrolyte in fuel cell. We studied the performance of fuel cell with GO paper as the electrolyte at low relative humidity and room temperature. This fuel cell showed more excellent fuel cell performance than that of fuel cell with Nafion membrane as the electrolyte. Our study opens up GOFC for a cost-effective next generation

fuel cell system.

Chapter 6 presents the application of GO as an electrolyte in lead battery. We fabricated the lead battery with GO paper as the solid electrolyte. This lead battery demonstrated comparable performance to lead battery using H_2SO_4 solution electrolyte. Thus, GOLB suggests the high potential for development of a small-sized dry lead battery.

Chapter 7 gives the general conclusion of the thesis.

CONTENT

PREFACE

CHAPTER-1

Introduction

1.1 General background	1
1.2 Preparing method of GO	1
1.2-1 Preparation of GO	2
1.2-2 Reduction of GO	3
1.3 Properties of GO	3
1.3-1 Electrochemical capacitance properties	4
1.3-2 ORR properties	4
1.4 Application of GO	5
1.4-1 Graphene oxide fuel cell (GOFC)	6
1.4-2 Graphene oxide lead battery (GOLB)	6
1.5 Objective and scope of this thesis	6
References	

CHAPTER-2

Electrolytic Graphene Oxide and its Electrochemical Properties

2.1 Introduction	17
2.2 Experimental	18
2.2-1 Preparation of materials	18
2.2-2 Characterization and electrochemical measurement	19
2.3 Results and Discussion	20
2.3-1 Electrolytic graphene oxide	20
2.3-2 Capacitance properties	24
2.3-3 Photoelectrochemical properties	26
2.3-4 Oxygen reduction reaction properties	27
2.4 Conclusions	29
References	

CHAPTER-3

Effect of the Reduction Method and Electrochemical Oxidation/Reduction Cycle on the electrochemical capacitance of Graphene Oxide

3.1 Introduction.....	46
3.2 Experimental.....	48
3.2-1 Preparation of materials.....	48
3.2-2 Oxidation/reduction cycle.....	48
3.2-3 XPS measurement.....	48
3.2-4 Characterization and electrochemical measurement.....	49
3.3 Results and Discussion	50
3.3-1 Analysis of GO and rGO by XPS	50
3.3-2 Effect of reduction methods.....	51
3.3-3 Effect of oxidation/reduction cycle and reaction mechanism.....	52
3.4 Conclusions.....	57
References	

CHAPTER-4

A Self-Assembly Route to an Iron Phthalocyanine/Reduced Graphene Oxide Hybrid Electrocatalyst Affording an Ultrafast Oxygen Reduction Reaction

4.1 Introduction.....	75
4.2 Experimental.....	78
4.2-1 Preparation of the FePc/GO hybrid by self-assembly	78
4.2-2 Preparation of the FePc/rGO hybrid.....	78
4.2-3 Preparation of rGO and FePc electrode.....	79
4.2-4 Preparation of FePc/rGO bilayer	79
4.2-5 Preparation of the standard Pt/C electrode	79
4.2-6 Characterization.....	80
4.2-7 Electrochemical analysis	80
4.3 Results and Discussion	81
4.3-1 Self-assembly and electrochemical reduction of FePc on GO.....	81
4.3-2 ORR properties of FePc/rGO hybrid.....	82
4.3-3 Raman and XPS studies of self-assembled FePc on GO and rGO obtained by electrochemical reduction and other reduction methods.....	84
4.4 Conclusions.....	87
References	

CHAPTER-5

Graphene Oxide Fuel Cell (GOFC)

5.1 Introduction.....	103
5.2 Experimental.....	104
5.2-1 Synthesis of GO and nanoGO	104
5.2-2 Preparation of GO paper as the electrolyte.....	106
5.2-3 Measurement of the proton conductivity of the GO paper	106
5.2-4 Fabrication of the GOFC	106
5.2-5 Fuel cell performance tests	107
5.3 Results and Discussion	107
5.3-1 Proton conduction of GO paper.....	107
5.3-2 Performance of GOFC.....	108
5.4 Conclusions.....	110
References	

CHAPTER-6

Graphene Oxide Lead Battery (GOLB)

6.1 Introduction.....	119
6.2 Experimental.....	120
6.2-1 Synthesis of GO paper	120
6.2-2 Fabrication and tests of the GOLB	120
6.3 Results and Discussion	121
6.4 Conclusions.....	123
References	

CHAPTER-7

General conclusions.....	129
--------------------------	-----

ACKNOWLEDGEMENTS

CHAPTER-1

Introduction

1.1 General background

Graphene, which consists of a one-atom-thick nanosheet comprising an sp^2 -bonding carbon structure, has been attracted many physicist due to its unique structure and properties, including zero band gap structure, a large specific surface area ($2630 \text{ m}^2 \text{ g}^{-1}$), high electron mobility ($200000 \text{ cm}^2 \text{ V}^{-1} \text{ s}^{-1}$), good thermal conductivity ($4000\sim 5000 \text{ W mK}^{-1}$) [1-5]. Graphene can be prepared by various methods, including mechanical exfoliation from graphite [1], epitaxial growth on SiC [6, 7], or chemical vapor deposition on metal substrate [8, 9]. As the one of the method to obtain in large scale, there is a chemical method that exfoliation of graphite oxide in solution followed by reduction of exfoliated graphite oxide, i.e. graphene oxide (GO) [10-12]. Many chemists have been challenged to remove oxygen functional groups completely [13-21]. In either approach, reducing GO into intrinsic graphene is impossible, reduced GO (rGO) differ from intrinsic graphene in chemical structure and rGO has many defective site and a little remained oxygen functional groups (Figure 1-1). However, thanks to a better understanding of GO, it is not only just material “as precursor” anymore but also novel material with various interesting chemical properties attracting many chemists [22-25].

1.2 Preparing method of GO

In generally, GO is prepared via a two-step solution process as illustrated in Figure 1-1. First, graphite oxide is prepared by oxidizing graphite in solution. Second, GO is prepared by exfoliating graphite oxide in solution. GO is electrically insulating materials due to its disrupted sp^2 bonding networks. Using GO as electrode materials, electrical conductivity is required to recover its

sp² networks by reducing GO. The reduction methods can be achieved by chemical [14-17], thermal [18, 19], electrochemical [20, 26] and photo reduction [21, 27]. Because the properties of rGO are affected by reduction methods, its reduction method is one of the most important reactions [13, 22, 28]. The following session explain the history about oxidation method and typical reduction reaction.

1.2-1 Preparation of GO

GO can be prepared by chemically oxidizing graphite and then exfoliating graphite oxide. The history about oxidation method of graphite is very old and many methods are reported [10-12]. The first oxidation method is discovered by Brodie and this method is used fuming HNO₃ and KClO₃ as oxidant of graphite (Brodie's method) [10]. In 1898, the other oxidation method, which is the way of oxidizing graphite by using potassium in concentrated H₂SO₄ and HNO₃ mixture, is discovered by Staudenmaier (Staudenmaier's method) [11]. Due to this method require long time and dangerousness of explosion for rapid oxidation, this method was improved to obtain graphite oxide in a short time by Hummers and Offeman in 1958 [12]. This method is the most common oxidation method, i.e. Hummers' method. The method is below.

Graphite powder (2.0 g), NaNO₃ (2.0 g), and concentrated H₂SO₄ (92 mL) is mixed in an ice-bath. KMnO₄ (12 g) is added very slowly and then the mixture is heated at 95°C to oxidize the graphite powder. The resulting mixture is diluted with distilled water and added 30% H₂O₂ to neutralize any remaining KMnO₄. The product mixture is washed with 5% HCl following distilled water by centrifuging several times, and dried in an oven at 70°C. Thus, graphite oxide is obtained.

GO is prepared by exfoliating of graphite oxide. The van der Waals force between adjacent layers is weaken by introducing oxygen functional groups in interlayer and graphite oxide can be easily exfoliated into individual GO. As the exfoliation method, ultrasonic irradiation or using of separating agent such as tetrabutylammonium is reported. The ultrasonic irradiation method is

below.

Graphite oxide is suspended in distilled water by ultrasonic bath for 2 h and the suspension is ultracentrifuged at 10000 rpm.

Additionally, we developed new oxidation method which is the way of electrochemically oxidizing the surface of carbon electrode in pure water^[26]. This method is very simple and free from impurities in room temperature. The detail is described in CHAPTER 2.

1.2-2 Reduction of GO

Recently, various reduction methods have been reported^[13-21, 26, 27]. As typical reduction method, chemical^[14-17] and thermal reduction is reported^[18, 19]. We discovered the new photoreduction method^[21, 27, 29], where GO is reduced by irradiating UV lamp. Moreover, we succeed photo patterning of GO using TEM grid as mask^[29]. This suggests the potential as the one of the new method of designing electronic circuitry on the surface of single GO sheet. Additionally, the photoreduction can easily obtain rGO with no contamination in room temperature. The difference of reduction method affect to the difference of rGO structure and properties such as electrochemical capacitance^[30]. This is explained in CHAPTER 3.

1.3 Properties of GO

GO exhibit various interesting chemical properties due to its heterogeneous chemical and electronic structures^[23-26, 31, 32]. Additionally, GO is able to combine nanomaterials such as metal oxide/hydroxide, metal complex, and functional polymer due to its oxygen functional groups of GO surface^[33-39]. Moreover, rGO is suitable for various electrode materials because rGO is electronic conductor. The following session described about electrochemical properties, particularly electrochemical capacitance properties and oxygen reduction reaction (ORR) properties, of GO and rGO.

1.3-1 Electrochemical capacitance properties

GO has a high specific surface area due to two-dimensional sheet material. GO can transmute into high electric conductive materials by reducing it. These two properties are important for an electrode of electrochemical double layer capacitor (EDLC). The study in this field has been intensively researched [40-46]. The first study of EDLC using rGO as electrodes was reported by R. S. Ruoff *et al.* in 2008 [47]. In this study, the rGO electrode of EDLC was prepared by chemically reducing GO with hydrazine monohydrate as reducing agent. This EDLC exhibited specific capacitance of 135 F/g in aqueous electrolyte. In 2011, this group developed more porous rGO electrode (specific surface area: 3100 m²/g) by treating a simple activation with KOH of GO and then the rGO electrode exhibited more excellent EDLC properties [48].

Moreover, GO has oxygen functional groups, such as carbonyl and hydroxyl; provide pseudocapacitance as a complement to EDLC. Z. Lin *et al.* [49] were reported larger specific capacitance of 276 F/g in aqueous electrolyte. As the other approach, due to surface oxygen functional groups can anchor metal cation firmly to GO surface, the GO-based hybrid materials have pseudocapacitance properties derive from the metal oxide and/or hydroxide. The studies about GO-based pseudocapacitance have been intensively reported. Ni(OH)₂, MnO₂, and Co₃O₄ are known as GO-based pseudocapacitor [34, 50-53]. We tried to develop new GO-based electrochemical capacitance electrode by conducting of oxidation/reduction cycle (Figure 1-2) [54] and then the detail is described in CHAPTER 3.

1.3-2 ORR properties

The studies about ORR properties of GO have been researched. Typically, three type of Pt-free ORR catalyst are reported: (1) metal oxide/rGO hybrid catalyst [33, 35, 55-58], (2) heteroatom-doped graphene catalyst [59-63], and (3) Fe-N-C bonding compound/rGO catalyst [36, 64, 65].

The researches of metal oxide/rGO (Co₃O₄/rGO, Mn₃O₄/rGO etc.) hybrid catalysts, which

form metal oxide nanoparticle on rGO surface, have been researched. Although these catalysts can fabricate in a simple method such as hydrothermal or chemical reduction, these catalysts is not suitable for ORR catalysts in acid medium due to these metal oxide is dissolved in that.

The studies of heteroatom (N, S, P, B, etc.) doping into sp^2 carbon bonding structure also have been intensively researched. In the case of graphene, L. Dai *et al.* [59] reported N-doped graphene for the first time. By doping it into graphene structure, the disruption in surface charge and spin asymmetry is introduced into the structure due to the difference of the bond length and electronegativity between heteroatom and carbon, which improves ORR activity [66-68]. Additionally, binary-doping is able to more improve ORR activity [61, 63] and J. S. Yu *et al.* [62] reported ternary-doping rGO has more excellent ORR activity than that of the commercial Pt/C in alkaline medium.

As the third approach, the researches of Fe-N-C bonding compound/rGO (iron phthalocyanine/rGO and others) hybrid catalysts, which use rGO as support material of these compounds with ORR activity, have been studied. The ORR activity of these catalysts can be improved by immobilizing these compounds on rGO support in high dispersion condition. We focused on this point and developed new iron phthalocyanine/rGO (FePc/rGO) hybrid catalyst prepared by a self-assembly process (Figure 1-3) [36]. The study is described in CHAPTER 4.

1.4 Application of GO

In our recent study, we found multi-layered GO (GO paper) exhibit high proton conduction. The epoxide (COC) of GO surface acts as the site for proton transfer even at low relative humidity and room temperature [31]. In this point, we developed new fuel cell [69] and lead battery [70] with GO as the electrolyte (Figure 1-4, 5). The following session explained about these cells.

1.4-1 Graphene oxide fuel cell (GOFC)

As noted above, GO paper has proton conduction. Additionally, GO paper does not pass H₂ and O₂ gasses, but in interlayer between GO can pass H₂O molecules ^[71]. Therefore, GO paper is suitable as an electrolyte for fuel cell. Moreover, inexpensive GO paper can be facile fabricated. This point leads to development of the cost-effective fuel cell (Figure 1-4) ^[69]. The detail is described CHAPTER 5.

1.4-2 Graphene oxide lead battery (GOLB)

Lead batteries has some demerits, which are the dangerousness of liquid spill and low gravity energy density, due to containing a concentrated H₂SO₄ solution as electrolyte ^[72-75]. GO paper has potential for working as solid electrolyte due to its proton conduction and dried-paper. Trying to develop the lead battery with GO paper as solid electrolyte, these problems are defused, which lead to development of the small-sized dry lead battery (Figure 1-5) ^[70]. The study is described CHAPTER 6.

1.5 Objective and scope of this thesis

A most important and attractive aspect of GO is abundance of unique properties from heterogeneous structure. Thanks to its oxygen functional groups, GO has various chemical properties and is easily able to combine the other nanomaterials. Additionally, because GO can make from natural graphite, which exists in great abundance on the earth, GO is able to produce in large volume at low cost. Therefore, it is important for us to investigate its properties in detail and then to open up the new field. In the present study, we focus on electrochemical properties of GO in its various chemical properties. The Main goals this study are states as below;

- The investigation of electrochemical properties of GO prepared by the new electrochemical method in facile and controllable of its oxidation degree
- The research about effect of the reduction method and the electrochemical oxidation/reduction cycle on the electrochemical capacitance of GO
- The study of a new self-assembly route to an FePc/rGO hybrid catalyst affording an ultrafast ORR
- Development of GOFC and GOLB

References

- [1] K. S. Novoselov, A. K. Geim, S. V. Morozov, D. Jiang, Y. Zhang, S. V. Dubonos, I. V. Grigorieva and A. A. Firsov, *Science* **2004**, 306, 666.
- [2] Y. Zhang, Y. Tan, H. L. Stormer and P. Kim, *Nature* **2005**, 438, 201.
- [3] K. I. Bolotin, K. J. Sikes, Z. Jiang, M. Klima, G. Fudenberg, J. Hone, P. Kim and H. L. Stormer, *Solid State Commun.* **2008**, 146, 351.
- [4] A. A. Balandin, S. Ghosh, W. Bao, I. Calizo, D. Teweldebrhan, F. Miao and C. N. Lau, *Nano Lett.* **2008**, 8, 902.
- [5] R. R. Nair, P. Blake, A. N. Grigorenko, K. S. Novoselov, T. J. Booth, T. Stauber, N. M. R. Peres and A. K. Geim, *Science*, **2008**, 320, 1308.
- [6] C. Faugeras, A. Nerrire, M. Potemski, A. Mahmood, E. Dujardin, C. Berger, W. A. De-Heer, *Appl. Phys. Lett.* **2008**, 92 Article number 011914.
- [7] K. S. Subrahmanyam, S. R. C. Vivekchand, A. Govindaraj, C. N. R. Rao, *J. Mater. Chem.* **2008**, 18, 1517
- [8] Bae, S.; Kim, H.; Lee, Y.; Xu, X.; Park, J. S.; Zheng, Y.; Balakrishnan, J.; Lei, T.; Kim, H. R.; Song, Y. I.; Kim, Y. J.; Kim, K. S.; Ozyilmaz, B.; Ahn, J. H.; Hong, B. H.; Iijima, S. *Nat. nanotech.* **2010**, 5, 574.
- [9] D. Wei, Y. Liu, Y. Wang, H. Zhang, L. Huang, G. Yu, *Nano Lett.* **2009**, 9, 1752.
- [10] B. C. Brodie, *Phil. Trans.* **1859**, 149, 249.
- [11] L. Staudenmaier, *Ber. Dtsch. Chem. Ges.* **1898**, 31, 1481.
- [12] W.S. Hummers, R.E. Offeman, *J. Am. Chem. Soc.* **1958**, 80, 1339.
- [13] S. Pei, H.-M. Cheng, *Carbon* **2012**, 50, 3210.
- [14] S. Stankovich, D. A. Dikin, R. D. Piner, K. A. Kohlhaas, A. Kleinhammers, Y. Jia, Y. Wu, S. T. Nguyen, R. S. Ruoff, *Carbon* **2007**, 45, 1558.

- [15] S. Park, R. S. Ruoff, *Nat. nanotechnol.* **2009**, 4, 217.
- [16] H. J. Shin, K. K. Kim, A. Benayad, S. M. Yoon, H. K. Park, I. S. Jung, M. H. Jin, H. K. Jeong, J. M. Kim, J. Y. Choi, Y. H. Lee, *Adv. Funct. Mater.* **2009**, 19, 1987.
- [17] V. C. Tung, M. J. Allen, Y. Yang, R. B. Kaner, *Nat. Nanotechnol.* **2009**, 4, 25.
- [18] M. J. McAllister, J. L. Li, D. H. Adamson, H. C. Schniepp, A. A. Abdala, J. Liu, M. Herrera-Alonso, D. L. Milius, R. Car, R. K. Prud'homme, I. A. Aksay, *Chem. Mater.* **2007**, 19, 4396.
- [19] H. C. Schniepp, J.-L. Li, M. J. McAllister, H. Sai, M. Herrera-Alonso, D. H. Adamson, R. K. Prud'homme, R. Car, D. A. Saville, I. A. Aksay, *J. Phys. Chem. B* **2006**, 110, 8535.
- [20] H. L. Guo, X. F. Wang, Q. Y. Qian, F. B. Wang, X. H. Xia, *ACS Nano* **2009**, 3, 2653.
- [21] Y. Matsumoto, M. Morita, S. Y. Kim, Y. Watanabe, M. Koinuma, S. Ida, *Chem. Lett.* **2010**, 39, 750.
- [22] D. R. Dreyer, S. Park, C. W. Bielawski, R. S. Ruoff, *Chem. Soc. Rev.* **2010**, 39, 228.
- [23] K. P. Loh, Q. Bao, G. Eda, M. Chhowalla, *Nat. Chem.* **2010**, 2, 1015.
- [24] Y. Huang, J. Liang, Y. Chen, *Small* **2012**, 8, 1805.
- [25] Y. Liang, Y. Li, H. Wang, H. Dai, *J. Am. Chem. Soc.* **2013**, 135, 2013.
- [26] Y. Matsumoto, H. Tateishi, M. Koinuma, Y. Kamei, C. Ogata, K. Gezuhara, K. Hatakeyama, S. Hayami, T. Taniguchi, A. Funatsu, *J. Electroanal. Chem.* **2013**, 704, 233.
- [27] Y. Matsumoto, M. Koinuma, S. Y. Kim, Y. Watanabe, T. Taniguchi, K. Hatakeyama, H. Tateishi, Shintaro Ida, *ACS Appl. Mater. Interfaces* **2010**, 2, 3461.
- [28] A. Ambrosi, A. Bonanni, Z. Sofer, J. S. Cross, M. Pumera, *Chem. Eur. J.* **2011**, 17, 10763.
- [29] Y. Matsumoto, M. Koinuma, S. Ida, S. Hayami, T. Taniguchi, K. Hatakeyama, H. Tateishi, Y. Watanabe, S. Amano, *J. Phys. Chem. C* **2011**, 115, 19280.

- [30] M. Koinuma, H. Tateishi, K. Hatakeyama, S. Miyamoto, C. Ogata, A. Funatsu, T. Taniguchi, Y. Matsumoto, *Chem. Lett.* **2013**, 42, 924.
- [31] K. Hatakeyama, M. R. Karim, C. Ogata, H. Tateishi, A. Funatsu, T. Taniguchi, M. Koinuma, S. Hayami, Y. Matsumoto, *Angew. Chem. Int. Ed.* **2014**, 53, 6997.
- [32] C. Ogata, M. Koinuma, K. Hatakeyama, H. Tateishi, M. Z. Asrori, T. Taniguchi, A. Funatsu, Y. Matsumoto, *Scientific Reports*, **2014**, 4, Article Number 3647.
- [33] Y. Liang, Y. Li, H. Wang, J. Zhou, J. Wang, T. Regier, H. Dai, *Nat. Mater.* **2011**, 10, 780.
- [34] H. Wang, H. S. Casalongue, Y. Liang, H. Dai, *J. Am. Chem. Soc.* **2010**, 132, 7472.
- [35] Z.-S. Wu, S. Yang, Y. Sun, K. Parvez, X. Feng, K. Müllen, *J. Am. Chem. Soc.* **2012**, 134, 9082.
- [36] T. Taniguchi, H. Tateishi, S. Miyamoto, K. Hatakeyama, C. Ogata, A. Funatsu, S. Hayami, Y. Makinose, N. Matsushita, M. Koinuma, Y. Matsumoto, *Part. Part. Syst. Charact.* **2013**, 30, 1063.
- [37] M. Jahan, Q. Bao, K. P. Loh, *J. Am. Chem. Soc.* **2012**, 134, 6707.
- [38] Y. Xu, Z. Lin, X. Huang, Y. Liu, Y. Huang, X. Duan, *ACS Nano* **2013**, 7, 4042.
- [39] X. Liu, F. Wang, R. Aizen, O. Yehezkeli, I. Willner, *J. Am. Chem. Soc.* **2013**, 135, 11832.
- [40] M. F. El-Kady, V. Strong, S. Dubin, R. B. Kaner, *Science* **2012**, 335, 1326.
- [41] X. Yang, C. Cheng, Y. Wang, L. Qiu, D. Li, *Science* **2013**, 341, 534.
- [42] Z.-S. Wu, K. Parvez, X. Feng, K. Mullen, *Nat. Commun.* **2013**, 4, Article Number 2487.
- [43] K. Sheng, Y. Sun, C. Li, W. Yuan, G. Shi, *Scientific Reports* **2012**, 2, Article Number 247.
- [44] Y. Tao, X. Xie, W. Lv, D.-M. Tang, D. Kong, Z. Huang, H. Nishihara, T. Ishi, B. Li, D. Golberg, F. Kang, T. Kyotani, Q.-H. Yang, *Scientific Reports* **2013**, 3, Article Number 2975.
- [45] J. J. Yoo, K. Balakrishnan, J. Huang, V. Meunier, B. G. Sumpter, A. Srivastava, M. Conway, A. L. M. Reddy, J. Yu, R. Vajtai, P. M. Ajayan, *Nano Lett.* **2011**, 11, 1423.
- [46] J. Luo, H. D. Jang, J. Huang, *ACS Nano* **2013**, 7, 1464.

- [47] M. D. Stoller, S. Park, Y. Zhu, J. An, R. S. Ruoff, *Nano Lett.* **2008**, 8, 3498.
- [48] Y. Zhu, S. Murali, M. D. Stoller, K. J. Ganesh, W. Cai, P. J. Ferreira, A. Pirkle, R. M. Wallace, K. A. Cychoz, M. Thommers, D. Su, E. A. Stach, R. S. Ruoff, *Science* **2011**, 332, 1537.
- [49] Q. Wu, Y. Xu, Z. Yao, A. Liu, G. Shi, *ACS Nano* **2010**, 4, 1963.
- [50] G. Yu, L. Hu, N. Liu, H. Wang, M. Vosgueritchaian, Y. Yang, Y. Cui, Z. Bao, *Nano Lett.* **2011**, 11, 4438.
- [51] Y. Cheng, S. Lu, H. Zhang, C. V. Varanasi, J. Liu, *Nano Lett.* **2012**, 12, 4206.
- [52] L. Peng, X. Peng, B. Liu, C. Wu, Y. Xie, G. Yu, *Nano Lett.* **2013**, 13, 2151.
- [53] X. Xia, D. Chao, Z. Fan, C. Guan, X. Cao, H. Zhang, H. J. Fan, *Nano Lett.* **2014**, 14, 1651.
- [54] H. Tateishi, M. Koinuma, S. Miyamoto, Y. Kamei, K. Hatakeyama, C. Ogata, T. Taniguchi, A. Funatsu, Y. Matsumoto, *Carbon* **2014**, 76, 40.
- [55] Y. Liang, H. Wang, J. Zhou, Y. Li, J. Wang, T. Regier, H. Dai, *J. Am. Chem. Soc.* **2012**, 134, 3517.
- [56] S. Li, D. Wu, C. Cheng, J. Wang, F. Zhang, Y. Su, X. Feng, *Angew. Chem. Int. Ed.* **2013**, 52, 12105.
- [57] J. Duan, Y. Zheng, S. Chen, Y. Tang, M. Jaroniec, S. Qiao, *Chem. Commun.* **2013**, 49, 7705.
- [58] H. Zhu, S. Zhang, Y.-X. Huang, L. Wu, S. Sun, *Nano Lett.* **2013**, 13, 2947.
- [59] L. Qu, Y. Liu, J.-B. Baek, L. Dai, *ACS Nano* **2010**, 4, 1321.
- [60] Y. Li, W. Zhou, H. Wang, L. Xie, Y. Liang, F. Wei, J.-C. Idrobo, S. J. Pennycook, H. Dai, *Nat. nanotechnol.* **2012**, 7, 394.
- [61] S. Wang, L. Zhang, Z. Xia, A. Roy, D. W. Chang, J.-B. Baek, L. Dai, *Angew. Chem. Int. Ed.* **2012**, 51, 4209.
- [62] F. Razmiooei, K. P. Singh, M. Y. Song, J.-S. Yu, *Carbon* **2014**, 78, 257.

- [63] H. Fei, R. Ye, Y. Gong, Z. Peng, X. Fan, E. L. Samuel, P. M. Ajayan, J. M. Tour, *ACS Nano* **2014**, 8, 10837.
- [64] H. Yin, C. Zhang, F. Liu, Y. Hou, *Adv. Funct. Mater.* **2014**, 24, 2930.
- [65] Z. Xiang, Y. Xue, D. Cao, L. Huang, J.-F. Chen, L. Dai, *Angew. Chem. Int. Ed.* **2014**, 53, 2433.
- [66] L. Zhang, Z. Xia, *J. Phys. Chem. C* **2011**, 115, 11170.
- [67] Y. Jiao, Y. Zheng, M. Jaroniec, S. Zhang, Qiao, *J. Am. Chem. Soc.* **2014**, 136, 4394.
- [68] T. Xing, Y. Zheng, L. H. Li, B. C. C. Cowie, D. Gunzelmann, S. Z. Qiao, S. Huang, Y. Chen, *ACS Nano* **2014**, 8, 6856.
- [69] H. Tateishi, K. Hatakeyama, C. Ogata, K. Gezuhara, J. Kuroda, A. Funatsu, M. Koinuma, T. Taniguchi, S. Hayami, Y. Matsumoto, *J. Electrochem. Soc.* **2013**, 160, F1175.
- [70] H. Tateishi, T. Koga, K. Hatakeyama, A. Funatsu, M. Koinuma, T. Taniguchi, Y. Matsumoto, *ECS Electrochem. Lett.* **2014**, 3, A19.
- [71] R. R. Nair, H. A. Wu, P. N. Jayaram, I. V. Grigorieva, and A. K. Geim, *Science*, **2012**, 335, 442.
- [72] K. Nakamura, M. Shiomi, K. Takahashi, M. Tsubota, *J. Power Sources* **1996**, 59, 153.
- [73] M. Shiomi, T. Funato, K. Nakamura, K. Takahashi, M. Tsubota, *J. Power Sources* **1997**, 64, 147.
- [74] D. Pavlov, P. Nikolov, T. Rogachev, *J. Power Sources* **2011**, 196, 5155.
- [75] D. Pavlov, *Lead-Acid Batteries: Science and Technology*, Elsevier, **2011**.

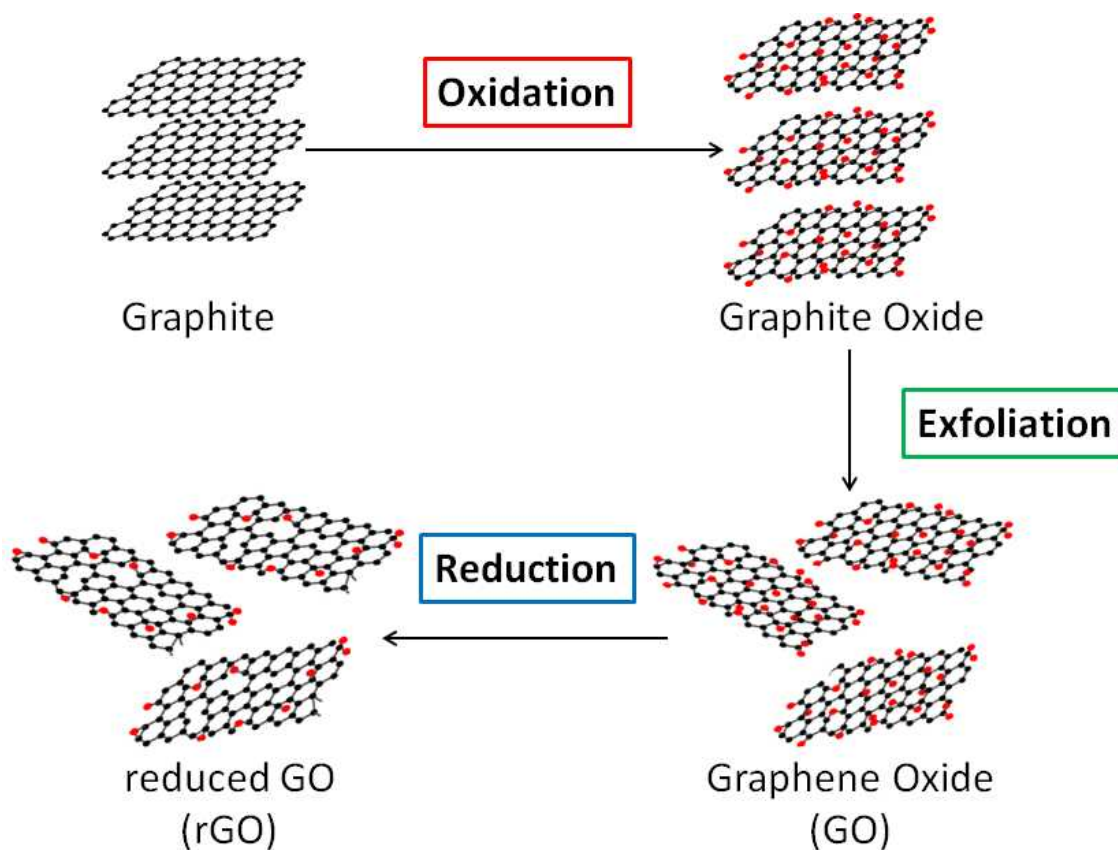


Figure 1-1. Schematic for preparing rGO.

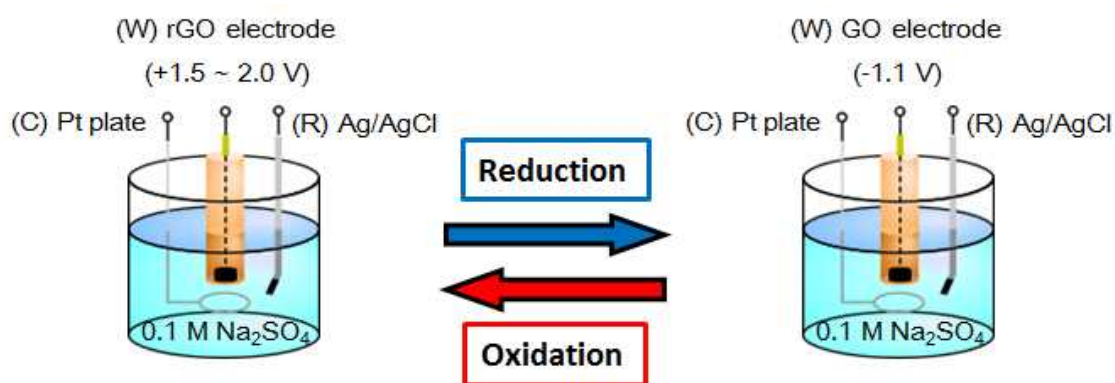


Figure 1-2. Schematic of electrochemical oxidation/reduction cycle.

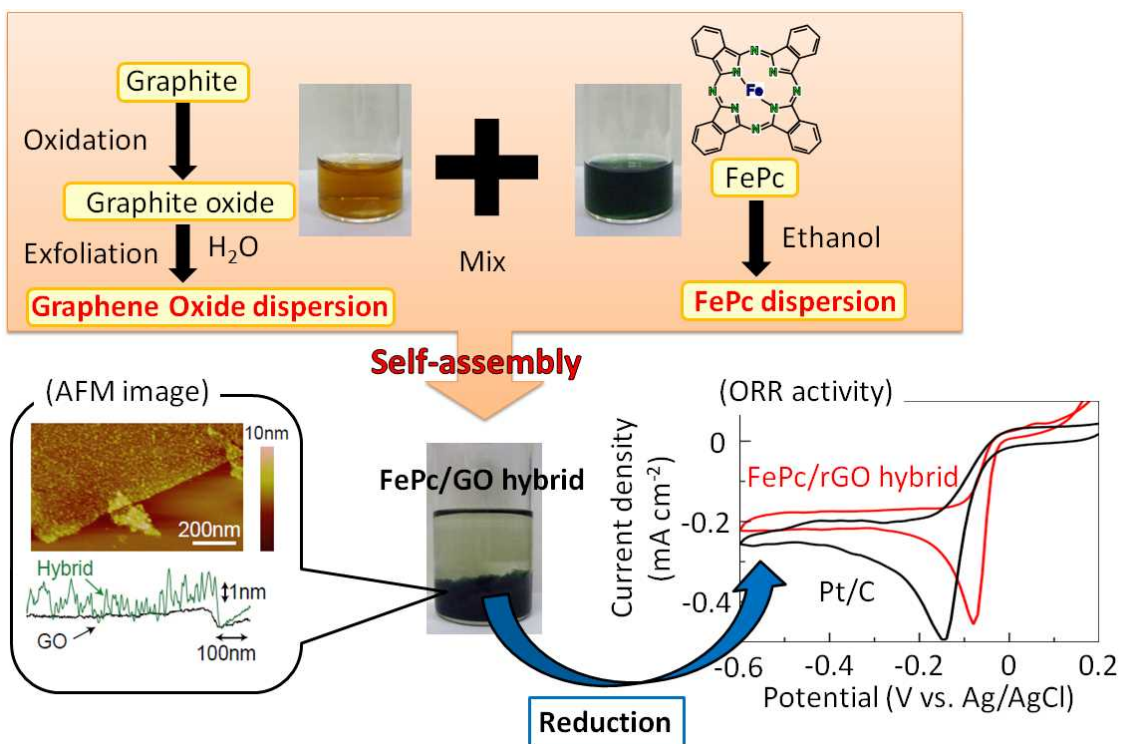


Figure 1-3. Novel FePc/rGO hybrid catalyst prepared by a self-assembly process and its ORR activity.

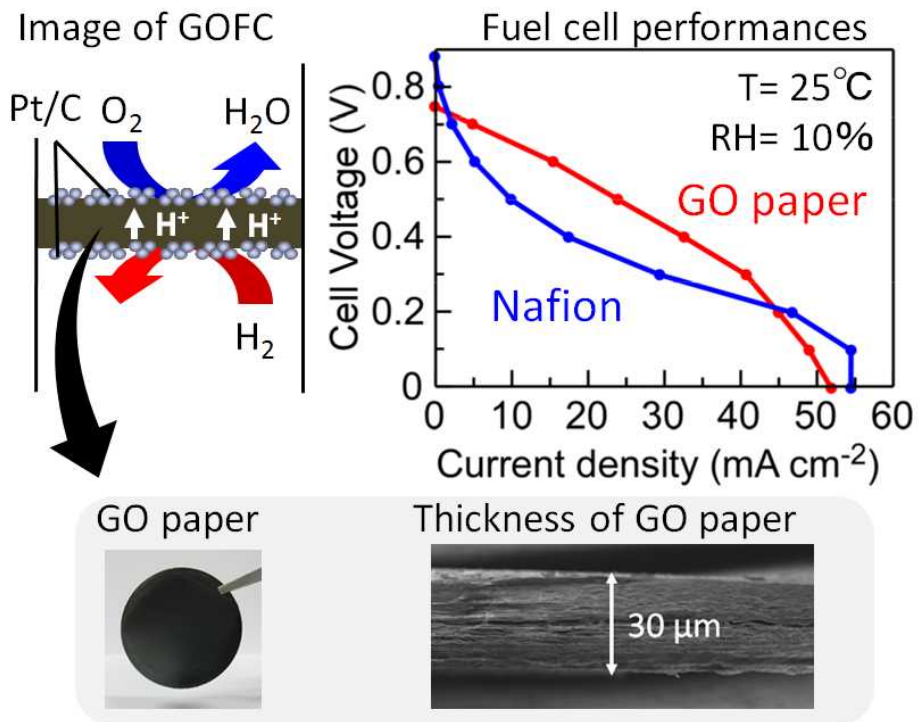


Figure 1-4. GOFC

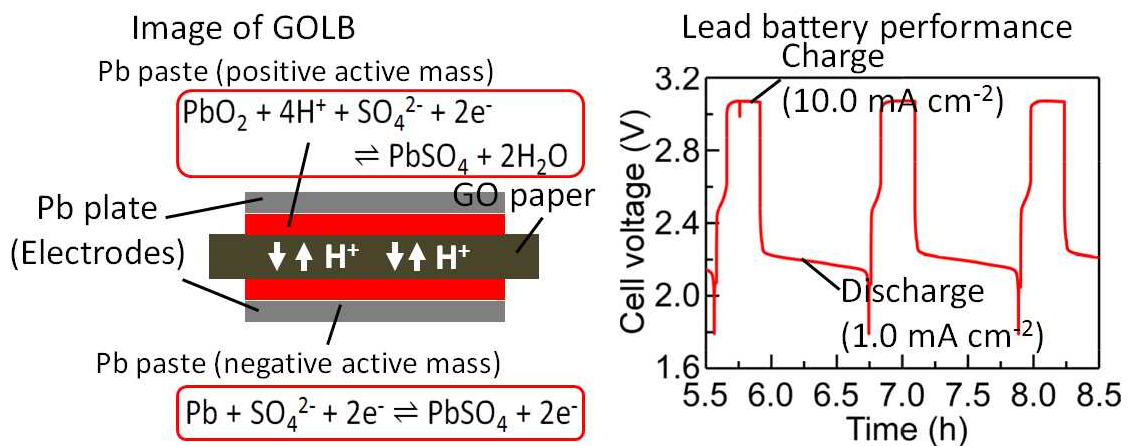


Figure 1-5. GOLB

CHAPTER-2

Electrolytic Graphene Oxide and its Electrochemical Properties

Overview

Low-cost graphene oxide (GO) and related materials are considered supermaterials because of their unique and excellent properties for many applications that are greatly affected by oxidation degree and dopants (impurities). Conventional GO prepared by the multistep Hummers' method is unable to control degree of the oxidation and impurities. In this chapter, we demonstrate a facile one-step method for preparing pure GO on graphite substrates [i.e. glassy carbon (GC), highly oriented pyrolytic graphite-basal plane surface (HOPG-b), and highly oriented pyrolytic graphite-edge surface (HOPG-e)] by electrolysis in pure water under high voltage; the resultant GO is called electrolytic GO (eGO). The degree of oxidation in eGO can be easily controlled by adjusting the applied voltage and the electrolysis time, and small-sized eGO can be obtained by using a counter tip electrode on the substrate during the electrolysis. Photoelectrochemically reduced eGO (r-eGO) had a large electrochemical capacitance and high electrocatalytic activity for the oxygen reduction reaction (ORR), and acted as an n-type semiconductor electrode. The r-eGO formed on HOPG-b had larger capacitance and higher activity for ORR than that on HOPG-e. The excellent properties of r-eGO were due to carbon defects and/or OH groups produced by the reduction of epoxide groups formed at the basal plane, as evidenced by X-ray photoelectron spectroscopy and Raman spectroscopy. The photoelectrochemical deposition of metal oxides or hydroxides on r-eGO increased the capacitance and catalytic activity of the material.

2.1 Introduction

Graphite oxide or aggregated graphene oxide (GO) is a supermaterial, because it has many unique and excellent properties; however, the degree of oxidation greatly affects its properties. GO is usually synthesized from graphite powders by the Hummers' method ^[1], although other synthesis methods ^[2, 3] have been reported. These methods entail complex steps using strong acids and/or oxidants such as manganese peroxide, and are unable to control the degree of oxidation in GO. Some impurities are contained in GO prepared by conventional methods, and so only a method that produces pure GO should be used for the evaluation of GO properties. Some electrochemical methods ^[4-6] using ionic solutions have also been reported, but these have been used for preparing graphene rather than for GO sheets exfoliated from graphite.

In this chapter, we present a new electrochemical oxidation method for preparing GO, in which a high oxidation voltage (~150 V) is applied at the graphite electrode in pure water. The current flow is meager in pure water owing to the insulating property of pure water; however, in this method, a sufficiently high oxidation voltage is applied at the interface between graphite and water to produce GO at the graphite surface. The degree of oxidation in the produced GO [here after called electrolytic GO (eGO)] can be easily controlled by adjusting the applied voltage and electrolysis time. In addition, note that compared with the Hummers' method, the proposed method for preparing eGO is simple and requires only a short time (<1 h), and the prepared eGO is "pure" (i.e. contamination free) because no acids or oxidants are used in the process.

The eGO films formed on graphite strongly adhere to the graphite substrate and so are not exfoliated from the substrate even under extreme electrochemical conditions, indicating that eGO is the best electrode material for fundamental electrochemical testing of GO. For use in fuel cells and electrochemical capacitors, GO and related materials are promising because they are inexpensive electrode materials with high specific surface area and high catalytic activity for the oxygen

reduction reaction (ORR). Reduced GO (rGO) [7–15] electrodes, and doped [16–19] and metal oxide hybrid [20–29] rGO electrodes, have high electrocatalytic activity for ORR and large capacitance in aqueous solutions. In this chapter, the characterization of eGO and its fundamental electrochemical properties are reported, together with its excellent electrode properties for ORR and electrochemical capacitor applications.

2.2 Experimental

2.2-1 Preparation of materials

Two types of GO were prepared, one by Hummers' method [1] and other by the high-voltage electrolysis, denoted as hGO and eGO, respectively. The hGO was prepared with 98% graphite powder (Wako Ltd., 2% was almost oxygen) as the starting material and was mainly used as reference for the characterization and electrochemical measurement of eGO. eGO was prepared by applying a bias (3~150 V) between the graphite anode (0.07 cm²) made either of glassy carbon (GC), highly oriented pyrolytic graphite-basal plane surface (HOPG-b), or highly oriented pyrolytic graphite-edge surface (HOPG-e) (BAS Ltd.) and a Au cathode (plate (1.5 cm × 2 cm) or tip (diameter 0.2 mm)) in pure water (>1.8 × 10⁷ Ω cm). All the GO electrodes were reduced in 0.1 M Na₂SO₄ solution at -1.1 V vs Ag/AgCl for 30 min under illumination using a 500 W Hg lamp to produce reduced eGO (r-eGO) or hGO (r-hGO). In the hGO/GC electrode fabrication, hGO was deposited on the GC electrode by an electrophoretic technique in hGO suspension (20 mg in 20 mL), where GC and Au were respectively used as the anode (hGO deposited electrode) and cathode at 3 V for 10 min (the distance between the two electrodes was 1 cm). Electrochemical reduction was carried out under irradiation, unless otherwise stated, because the electrode properties involved in the catalytic activity of ORR and capacitance were always slightly higher under irradiation than in the dark. On the other hand, MO_x/r-eGO/GC and MO_x/r-hGO/GC electrodes were prepared under

the same conditions as those for the photoelectrochemical reduction stated above, but in solutions containing metal cations such as Ni^{2+} , Co^{2+} , Ca^{2+} , Mn^{2+} , Fe^{2+} , and Ce^{3+} (10^{-3} M, as nitrate salts).

2.2-2 Characterization and electrochemical measurement

X-ray photoelectron spectroscopy (XPS; Thermo Scientific, SigmaProbe) was used to analyze the surfaces of all the GO samples. A monochromatized X-ray source ($\text{Al K}\alpha$, $h\nu = 1486.6$ eV) was used for the XPS. Raman spectroscopy (Jasco, NRS-3100) was performed using a 532 nm excitation source at room temperature. Attenuated total reflectance Fourier transform infrared (ATR-FTIR) measurements were carried out using PekinElmer FT-IR spectrometer Frontier equipped with horizontal ZnSe crystal. The surface morphology of the GO samples was observed by atomic force microscopy (AFM; Digital Instruments, Nanoscope V, tapping mode) and field-emission scanning electron microscopy (FE-SEM; JSM-7600F, JEOL). According to the XPS profiles, cations were deposited on the rGO electrodes as metal oxides or hydroxides (denoted $\text{MO}_x/\text{r-hGO}$ and $\text{MO}_x/\text{r-eGO}$ herein) owing to the increase in pH at the electrode surface during the electrochemical reduction. To analyze the amounts of metal oxides or hydroxides (MO_x) deposited on GO ($\text{MO}_x/\text{rGO}/\text{GC}$), inductively coupled plasma atomic emission spectroscopy (ICP-AES) was performed using a charge injection device (CID) plasma photoemission spectrophotometer (IRIS Advantage, Nippon Jarrell Ash) after dissolving the samples in acid solutions, the amounts of all the deposited MO_x species were lower than about 10% of r-hGO (in weight) in the cases of the $\text{MO}_x/\text{r-hGO}$ electrodes. Surface area of the GO samples was measured using UV-vis spectroscopy (Jasco, V-550) with methylene blue (MB) dye as a probe. The surface of the GO samples was soaked in 1 μM MB aqueous solution for 30 min, and then the concentration of the MB solution was measured by UV-vis spectra. The amount of adsorption of MB onto the GO samples was determined from the decrement of the absorbance at $\lambda = 664$ nm. The literature value of 1.30 nm^2 for surface

covered per molecule of MB was the basis for our calculations [30–32].

All electrochemical measurements were performed in three-electrode electrochemical cells. GO/GC, eGO/GC, eGO/HOPG-b, and eGO/HOPG-e were tested as electrodes for supercapacitors in 0.1 M Na₂SO₄ and for ORR in 1 M KOH saturated with O₂. Ag/AgCl and Pt plates were used as the reference and counter electrodes, respectively. A potentiostat with a function generator (Ivium Compactstat) was used to measure cyclic voltammograms. A rotating ring disk electrode (RRDE) system (Pine Instruments) was used to study the ORR mechanism at the r-eGO/GC electrode in 1 M KOH. r-eGO/GC and Pt were used as the disk and ring electrodes, respectively. Pt (20%)/C powder (ElectroChem Inc.) was used as the reference electrocatalyst for ORR. This was suspended in a propanol/water (1:1) solution, a droplet of which was placed on a GC electrode surface (0.1 mg cm⁻²) and then vacuum dried.

2.3 Results and Discussion

2.3-1 Electrolytic graphene oxide

The preparation scheme and surface SEM images of eGO are shown in Figure 2-1. Glassy carbon (GC), highly oriented pyrolytic graphite-basal plane surface (HOPG-b), and highly oriented pyrolytic graphite-edge surface (HOPG-e) electrodes (Figure 2-2) were electrolyzed at 3~150 V in pure water. Unless otherwise stated, the electrolysis was performed at 150 V for 60 min. The surfaces of the GC and HOPG-b electrodes morphologically changed to show many uniform circular pores of nanometer to micrometer sizes, valleys filled with pores, and cracks during eGO formation.

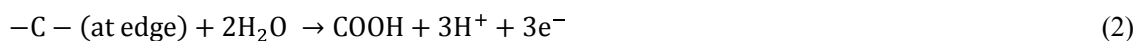
Figure 2-3 shows the XPS profiles of C1s, Raman spectra of the eGO surfaces. The C1s deconvolution analysis of eight peaks in these profiles for C=C, C-C, C defect (and/or CH), epoxide (COC), hydroxyl (COH), carbonyl (C=O), carboxyl (O=C-O), and $\pi-\pi^*$ [14, 33–36] showed the clearest results for the present samples. Both eGO/GC and eGO/HOPG-b showed spectra similar to that of

hGO (Figure 2-4), except for the amount of each oxygen functional group in the XPS profiles (Figure 2-3(a)). The atomic ratios of O/(C + O) and the amounts of all carbon bonding states are listed in Table 2-1. The main products were COC epoxide group at the basal plane together with relatively small amounts of COOH carboxyl group at the edges. The oxygen contents of both eGO/GC (about 21%) and eGO/HOPG-b (about 13%) prepared at 150 V for 60 min were always lower than that of hGO (32%) and decreased with decreasing applied voltage and electrolysis time (Table 2-1).

The oxidation of the HOPG-b surface was difficult in comparison with that of the GC surface, indicating that the basal plane is difficult to oxidize, compared with its edges, because the GC surface consists of edges as well as basal planes (see the high-intensity D band in Figure 2-3(b) and the C-C sp^3 bonding peak in Figure 2-3(a) of GC). The eGO had sufficient conductivity to enable the flow of current in the present electrochemical test because of its low oxygen content. In fact, large ORR currents were observed at eGO electrodes, as described in Section “**oxygen reduction reaction**”, even before the electrochemical reduction.

In the Raman spectra (Figure 2-3(b)), a broad D band ($\sim 1340\text{ cm}^{-1}$) appeared with eGO formation, which is clear for eGO/HOPG-b. The intensity ratio I_D/I_G of eGO/GC was 0.95, which was almost the same as that of hGO (0.97, Figure 2-4), whereas the intensity ratio of eGO/HOPG-b was small (0.22) because of the presence of the original G band ($\sim 1580\text{ cm}^{-1}$) of the HOPG-b substrate. The D and G bands are mainly due to carbon sp^3 bonds (disorder or defects) and carbon sp^2 bonds (π -conjugation), respectively [37–39], where the D' band ($\sim 1620\text{ cm}^{-1}$) as a result of disorder is contained in the present G band region. The broad D band is based on oxygen functional groups in the case of GO [37, 40]. In conclusion, the prepared eGO is pure GO or aggregated GO, has low oxygen content, and is contamination free because only pure water was used (i.e., the eGO consists of only C, O, and H). High voltage applied across the graphite/water interface promotes the

electrochemical oxidation of graphite; however, other electrochemical reactions such as O₂ evolution are strongly suppressed by pure water acting as an insulator. The electrochemical oxidation mainly occurs as follows:



Obviously, other oxygen functional groups are produced from COC and/or carbon directly by the electrochemical oxidation. Simultaneously, some defects are produced during the electrochemical reactions given above.

Figure 2-5 shows AFM images of the eGO surfaces. Many uniform circular pores and pore-filled cracks or valleys, produced during eGO formation, were clearly observed in the HOPG-b substrate, as shown in Figure 2-1, 5, and 6. Uniform circular pores with different depths were produced by CO₂ evolution during the electrolysis; deep pores were about ~40 nm in depth. Since the interlayer spacing of GO can be estimated at about 0.8 nm according to the XRD analysis of GO paper [41], the depth of the uniform circular pores corresponds to about 50 layers. The average thickness of eGO was estimated to be about 20 nm for GC and HOPG-b, according to calculations using the depth profiles of oxygen obtained by XPS with Ar etching (Figure 2-7) [42,43]. The production of uniform circular pores means that uniform electrochemical oxidation occurs at the edges of pores after the oxidation of trigger points at the basal plane, which may be atomic-level defects. For eGO/HOPG-b, its surface exhibited roughness on the 1 nm scale, owing to the presence of small GO pieces (Figure 2-5).

After the electrochemical (photoelectrochemical) reduction, small aggregates of r-eGO pieces were precipitated, covering the surface (Figure 2-8). During the electrochemical reduction, some of the produced eGO is exfoliated from the surface and then reprecipitated, because GO sheets with negative charge are released by negative bias but aggregated by π interaction of the produced

rGO at the electrode surface. The I_D/I_G ratio of r-eGO/GC increased from 0.95 to 1.09 (Figure 2-3(b)), indicating that the number of sp^3 -related bonds increases with the reduction. Figure 2-9 shows ATR-FTIR spectra obtained for eGO/GC and r-eGO/GC. The ATR-FTIR spectrum of eGO/GC shows peaks at 815 and 1240 ($\nu(\text{C-O-C})$), 1640 ($\nu(\text{COOH})$), 1720 ($\nu(\text{C=O})$), 1370 ($\nu(\text{C-OH})$), and a broad band at 3200 cm^{-1} ($\nu(\text{-OH})$) due to intercalated water molecules present on eGO/GC [44,45]. After the electrochemical reduction of eGO/GC, the peaks at 815, 1240, 1640 cm^{-1} were disappeared, suggesting the removal of epoxide and carboxyl groups. These results are in agreement with the XPS results (Figure 2-3(a) and Table 2-1), where the C defects and OH groups increased but COC groups decreased for all samples after the electrochemical reduction. The following reduction reaction mainly occurs [14].



To study the direct voltage effects on eGO formation, we performed HOPG-b electrolysis in which the counter electrode Au wire was placed on the center of the surface with a droplet of pure water, as illustrated in Figure 2-10(a). During this electrolysis, the real applied voltage strength depends on the distance from the point of the Au cathode; the voltage strength decreases from the center point (A) to the edge point (C) of the water droplet. After electrolysis for 30 min, we mapped the XPS peak intensities of O1s, C1s of COC and C=C groups at the formed eGO surface (Figure 2-10(b)). Large amounts of O and COC group were observed around the center, but that of C=C was small. Three points (points (A), (B), and (C)) were analyzed in detail by XPS (Figure 2-11), AFM (Figure 2-12(a)), and Raman spectroscopy (Figure 2-12(b)) in detail. At the center point (A), many large and deep pores were produced (Figure 2-12(a)) together with large oxygen content (Figure 2-11(b)), while at the edge of droplet the number and sizes of shallow pores were relatively small (Figure 2-12(a)) together with low oxygen content (Figure 2-11(b)). Thus, we can easily design GO films with various pore sizes and compositions on HOPG-b and GC substrates by controlling the

distance of counter electrodes, applied voltage, and electrolysis time.

2.3-2 Capacitance properties

Figure 2-13 show the cyclic voltammograms of the hGO and eGO electrodes and the typical $\text{MO}_x/\text{r-eGO}/\text{GC}$ electrodes, and specific area capacitance (mF cm^{-2}) at 0 V in 0.1 M Na_2SO_4 , respectively. All measurements of capacitance were performed in three-electrode electrochemical cells. With the three-electrode configuration, only one electrode, called the working electrode, contains the material being analyzed, and the applied voltage and charge transfer across the single electrode are markedly different than in a two-electrode cell configuration. The working electrode of a three-electrode cell has twice the range of potential applied to the electrodes of a two-electrode cell, resulting in doubling of the calculated capacitance ^[46]. Therefore, all the values of capacitance were converted and compared with the values of the three-electrode configuration. The capacitance was calculated from the linear relationship between scan rate and current (Figure 2-14), which was almost the same as in the potential range from -0.6 to 0.3 V. Large currents of double-layer charging capacitance were observed for the r-hGO and r-eGO electrodes, whereas low currents were observed for the hGO and eGO electrodes before the electrochemical reduction (Figure 2-13(a)). The remarkable increase in capacitance current with the electrochemical reduction for r-eGO is attributed not to an increase in electrical conductivity but to changes in surface carbon species and to a certain extent, to morphology (Figure 2-8).

The apparent order of the capacitance was as follows: r-hGO > r-eGO/HOPG-b > r-eGO/GC > r-eGO/HOPG-e, as shown in Figure. 2-13(a) and 15(a). Note that r-eGO/HOPG-b has the largest capacitance among all the r-eGO electrodes. This means that the high capacitance of rGO is based on the basal planes rather than on the edges of rGO. During eGO formation at the basal plane, COC groups are formed, which then change to C defects and/or OH groups upon

electrochemical reduction (Eq. (3)). These changes yield the real specific surface area or promote pseudocapacitance due to Faradic redox at the surface, leading to increased capacitance. For r-eGO/GC, the capacitance was low when the amount of COC groups of eGO/GC was small (i.e., prepared under low applied voltage and/or for a short time) before the reduction, as shown in Figure 2-13(c). Consequently, C defects or OH groups at the basal plane are important for capacitance. The specific capacitances per unit weight of r-eGO/GC and r-eGO/HOPG-b were roughly calculated to be about $6 \times 10^3 \text{ F g}^{-1}$, if the thickness of r-eGO is about 20 nm (20 layers) as stated already, whereas that of the present r-hGO as the reference was about 197 F g^{-1} under the same conditions. Although it was expected that the capacitances of r-eGO/GC and r-eGO/HOPG-b would not be high because of the low degree of oxidation, the estimated values are remarkably high. This result suggests that the specific capacitances per unit weight are affected only to the interface of GO/electrolyte. [As shown in Figure 2-16, the specific capacitance per unit weight (113 F g^{-1}) of r-hGO/GC prepared by placing a droplet of hGO suspension on the GC electrode was lower than that of the present sample prepared by electrophoresis.] To compare the specific capacitances per unit area, the surface area of the GO samples was measured by UV-vis spectroscopy with MB dye as a probe. The surface coverage of a single MB molecule is reported to be 1.30 nm^2 for molecules lying flat on the HOPG surface [32]. Thus, 7.7×10^{13} molecules/cm² adsorb on the even HOPG surface without any defect. From UV-vis spectra, the amounts of adsorption of the MB molecule for r-eGO/HOPG-b, r-eGO/GC, and r-hGO were estimated to be 1.1×10^{14} , 1.0×10^{14} , and 7.1×10^{14} molecules/cm², respectively. If it is assumed that the amount of adsorption of the MB molecule and the surface roughness are correlated, the surface roughness of r-hGO is about seven times that of r-eGO/GC and r-eGO/HOPG-b. Since r-hGO and r-eGO/GC showed almost the same oxidation condition on the surface (Table 2-1), the amount of adsorption could be used to evaluate the surface roughness. Considering the surface roughness, the specific capacitances per unit area of r-eGO/GC is about four times that of r-hGO.

Thus, r-eGO is an excellent electrode material for a supercapacitor, and its specific capacitance per unit area is higher than that of graphene as stated later.

Note that the capacitances of MO_x deposited electrodes were always greater than approximately 1.5- to 2-fold that of free r-eGO, but did not strongly depend on the metal cation type, as shown in Figure 2-13(c) and 16. It has been reported that the Faradic redox of some metal oxides directly affect on the increase in capacitance current [26, 27, 29]. However, the relatively weak dependence of the present capacitance on the metal oxide or hydroxide type suggests that the increase in capacitance current with deposition is mainly attributed to the increase in the number of C defects or OH groups on the rGO surface during MO_x deposition. According to the XPS results for $\text{MO}_x/\text{rGO}/\text{GC}$ (Figure 2-3(a) and Table 2-1), the number of C defects and OH groups largely increased with MO_x deposition. I_D/I_G also increased for the deposited samples, as shown in Figure 2-3(b) (1.15–1.17). We obtained the highest specific capacitance per unit weight of *ca.* 330 F g⁻¹ for the $\text{CoO}_x/\text{r-hGO}/\text{GC}$ electrode (Figure 2-16) (whose value is slightly lower than that of 550 F g⁻¹ estimated from the specific surface area of graphene [9, 47].) Consequently, the high capacitance of $\text{CoO}_x/\text{r-eGO}/\text{GC}$ was similar to that of $\text{CoO}_x/\text{r-hGO}/\text{GC}$, meaning that the r-eGO formed can serve as an excellent electrode in supercapacitors. The apparent specific capacitance per unit area calculated from the galvanostatic charge–discharge curve of the $\text{CoO}_x/\text{r-eGO}/\text{GC}$ electrode [C (mF cm⁻²) = i (mA cm⁻²) × dt/dV , Figure 2-15(a)] was about 22 mF cm⁻², and this electrode was stable because the specific capacitance still remains at 18 mF cm⁻² (~80%) after 1000 cycles (Figure 2-15(b)).

2.3-3 Photoelectrochemical properties

Figure 2-17 show the voltammograms of the r-eGO/GC and r-eGO/HOPG-b electrodes under chopped-light irradiation, the photocurrent as a function of the wavelength of monochromatic

light at 1.0 V, and the band structure of the electrodes, respectively. As shown in Figure 2-17(a), relatively large anodic photocurrent and small cathodic photocurrent were observed, suggesting that r-eGO is an n-type rather than p-type semiconductor. The photocurrents are based on the electron and hole produced by photons with energies higher than the band gap, not on the thermal effect, because the photoresponses of the currents are very slow for the latter case. Both the anodic and cathodic photocurrents produce C defects [48]. The potential at which the photocurrent changes from anodic (cathodic) to cathodic (anodic) photocurrent occur, corresponds to the flat band potential and is largely dependent on potential sweep direction (the changing potentials were about 0 and -0.9 V in the sweep directions from anodic to cathodic and from cathodic to anodic, respectively). This change in flat band potential is owing to the change in surface composition; the oxygen content of the surface increased under anodic bias and decreased under cathodic bias. From the onset wavelength of photocurrent (about 510~540 nm) in Figure 2-17(b), the band gap is calculated to be about 2.4 eV. The band structure of eGO (Figure 2-17(c)), where the energy difference between the π^* conduction band and the Fermi level in π -conjugated domains [49] is assumed to be about 0.8 eV, was previously reported [48]. This band structure applies to the largest π -conjugated domain the produces photocurrents, although there are various domains of various sizes, therefore, various band gaps in GO [49]. In the reduction process, the present photoelectrochemical reduction condition is more effective for preparing r-eGO and $\text{MO}_x/\text{r-eGO}$ than the dark reduction condition, since excited electron contribute to the reduction process.

2.3-4 Oxygen reduction reaction properties

Figure 2-18 show the I-V curves of the eGO and hGO electrodes, and typical $\text{MO}_x/\text{r-eGO}$ electrodes, and the electrodes in the current range from 100 to 150 μA , respectively, for ORR in 1 M KOH saturated with O_2 or N_2 . Note that all the eGO electrodes have higher catalytic activity than the

virgin substrates, and that their catalytic activity increases with the electrochemical reduction, especially for those with high amounts of COC group (prepared by oxidation at a high voltage for a long time for eGO/GC, as shown in Figure 2-18(a)). The observed current of eGO for ORR means that the eGO films have sufficient conductivity to enable current flow, in contrast to hGO. The order of catalytic activity for ORR is as follows: r-eGO/GC > r-eGO/HOPG-b > r-eGO/HOPG-e > r-hGO (Figure 2-18(c)). Note that all the r-eGO electrodes are higher than r-hGO in catalytic activity. The higher catalytic activity of r-eGO/HOPG-b than that of r-eGO/HOPG-e means that the basal plane of GO is more important to the catalytic activity. The C defects and/or OH groups produced mainly from the epoxide groups at the basal plane by the electrochemical reduction are thus confirmed to be important for the catalytic activity for ORR, similarly to the case of capacitance. The deposition of MnO_x and CoO_x increased the catalytic activity, as shown in Figure 2-18(b) and (c), but the other MO_x compounds produced no such effect. Thus, the catalytic activity for ORR depends on the type of metal cation.

The test results of RRDE are shown in Figure 2-19, where r-eGO/GC, $\text{MnO}_x/\text{r-eGO/GC}$, and $\text{CoO}_x/\text{r-eGO/GC}$ were used as the disk electrodes. There are two possible ORR mechanisms. One is the direct reduction of O_2 , in which O_2 is directly reduced to H_2O via four-electron transfer ($n = 4$); this is preferable for ORR. The other is a mechanism via two-electron transfer ($n = 2$), in which a HO_2^- (peroxide) intermediate is produced. The n values calculated from the well-known equation (Figure 2-20) using the RRDE results in Figure 2-19(a) were near 2.3 for the r-eGO/GC electrode and 3.4–3.8 for the $\text{MnO}_x/\text{r-eGO}$ and $\text{CoO}_x/\text{r-eGO}$ electrodes (Figure 2-19(b)); therefore, higher limiting currents are observed for these electrodes (Figure 2-18(b)). Relatively large and small ring currents due to HO_2^- oxidation were observed for the former (~85%) and latter two (12–28%) electrodes during ORR. Thus, direct O_2 reduction in ORR mainly occurred at the $\text{MnO}_x/\text{r-eGO/GC}$ and $\text{CoO}_x/\text{r-eGO/GC}$ electrodes; the two-electron transfer mechanism mainly occurred at the

r-eGO/GC electrode. Some interactions between MO_x and r-eGO are considered important for high catalytic activity, similar to that in the cases of the CoO_x and MnO_x hybrid rGO electrodes reported previously [22–24].

2.4 Conclusions

In summary, we developed a facile one-step method for preparing the oxidation-controlled GO electrodes in a short time (<1 h) by the anodic electrolysis of graphite under high voltage in pure water. Moreover, the present method is very important for the preparation of contaminant-free GO because pure water is only used. The eGO obtained had many pores (of nanometer to micrometer size) and was similar in composition to GO prepared by the Hummers' method. Its composition and morphology can be easily controlled by adjusting the applied voltage and electrolysis time. The eGO electrodes reduced by the photoelectrochemical reduction had high electrochemical capacitance and high electrocatalytic activity for ORR, and functioned as n-type semiconductor electrodes. The excellent properties of r-eGO were due to the C defects and/or OH groups produced from COC groups at the basal plane by photoelectrochemical reduction. Metal oxides or hydroxides, especially MnO_x and CoO_x , electrodeposited on r-eGO electrodes increased the capacitance and catalytic activity of the material. Thus, the present method is very useful for preparing oxidation-controlled pure GO, and therefore will be useful in many applications.

References

- [1] W.S. Hummers, R.E. Offeman, *J. Am. Chem. Soc.* **1958**, 80, 1339.
- [2] B.C. Brodie, *Ann. Chim. Phys.* **1859**, 59, 466.
- [3] L. Staudenmaier, *Ber. Deut. Chem. Ges.* **1898**, 31, 1481.
- [4] N. Liu, F. Luo, H. Wu, Y. Liu, C. Zhang, J. Chen, *Adv. Funct. Mater.* **2008**, 18, 1518.
- [5] G. Wang, B. Wang, J. Park, Y. Wang, B. Sun, J. Yao, *Carbon* **2009**, 47, 3242.
- [6] C.Y. Su, A.Y. Lu, Y. Xu, F.R. Chen, A.N. Khlobystov, L.J. Li, *ACS Nano* **2011**, 5, 2332.
- [7] L. Tang, T. Wang, Y. Li, H. Feng, J. Lu, *Adv. Funct. Mater.* **2009**, 19, 2782.
- [8] J. Wu, Y. Wang, D. Zhang, B. Hou, *J. Power Sources* **2011**, 196, 1141.
- [9] D.M. Stoller, S. Park, Y. Zhu, J. An, S.R. Ruoff, *Nano Lett.* **2008**, 8, 3498.
- [10] Y. Wang, Z. Shi, Y. Huang, Y. Ma, C. Wang, M. Chen, Y. Chen, *J. Phys. Chem. C* **2009**, 113, 13103.
- [11] W. Lv, D.M. Tang, Y.B. He, C.H. You, Z.Q. Shi, X.C. Chen, *ACS Nano* **2009**, 3, 3730.
- [12] Y. Zhu, S. Murali, M.D. Stoller, K.J. Ganesh, W. Cai, P.J. Ferreira, A. Pirkle, R.M. Wallace, K.A. Cychoz, M. Thommes, D. Su, E.A. Stach, R.S. Ruoff, *Science* **2011**, 332, 1537.
- [13] F.M. El-Kady, V. Strong, S. Dubin, B.R. Kaner, *Science* **2012**, 335, 1326.
- [14] M. Koinuma, C. Ogata, Y. Kamei, K. Hatakeyama, H. Teteishi, Y. Watanabe, T. Taniguchi, K. Gezuhara, S. Hayami, A. Funatsu, M. Sakata, Y. Kuwahara, S. Kurihara, Y. Matsumoto, *J. Phys. Chem. C* **2012**, 116, 19822.
- [15] C.N.R. Rao, A.K. Sood, K.S. Subrahmanyam, A. Govindaraj, *Angew. Chem. Int. Ed.* **2009**, 48, 7752.
- [16] L. Qu, Y. Liu, J.B. Beak, L. Dai, *ACS Nano* **2010**, 4, 1321.
- [17] Z.H. Sheng, L. Shao, J.J. Chen, W.J. Bao, F.B. Wang, X.H. Xia, *ACS Nano* **2011**, 5, 4350.

- [18] S. Wang, L. Zhang, Z. Xia, A. Roy, D.W. Chang, J.B. Baek, L. Dai, *Angew. Chem. Int. Ed.* **2012**, 51, 4209.
- [19] K. Gopalakrishnan, Kota Moses, A. Govindaraj, C.N.R. Rao, *Solid State Commun.* **2013**. in press.
- [20] H.R. Byon, J. Suntivich, Y. Shao-Horn, *Chem. Mater.* **2011**, 23, 3421.
- [21] X.Y. Yan, X.L. Tong, Y.F. Zhang, X.D. Han, Y.Y. Wang, G.Q. Jin, Y. Qina, X.Y. Guo, *Chem. Commun.* **2012**, 48, 1892.
- [22] Y. Liang, Y. Li, H. Wang, J. Zhou, J. Wang, T. Regier, H. Dai, *Nature Mater.* **2011**, 10, 780.
- [23] Y. Liang, H. Wang, J. Zhou, Y. Li, J. Wang, T. Regier, H. Dai, *J. Am. Chem. Soc.* **2012**, 124, 3517.
- [24] J. Wu, D. Zhang, Y. Wang, Y. Wan, B. Hou, *J. Power Sources* **2012**, 198, 122.
- [25] X. Dong, L. Wang, D. Wang, C. Li, J. Jin, *Langmuir* **2012** 28, 293.
- [26] Y. Wang, C.X. Guo, J. Liu, T. Chen, H. Yanga, C.M. Li, *Dalton Trans.* **2011**, 40, 6388.
- [27] Z. Lei, F. Shi, L. Lu, *ACS Appl. Mater. Interfaces* **2012**, 4, 1058.
- [28] S. Chen, J. Zhu, X. Wu, Q. Han, X. Wang, *ACS Nano* **2010**, 4, 2822.
- [29] X. Zhu, H. Dai, J. Hu, L. Ding, L. Jiang, *J. Power Sources* **2012**, 203, 243.
- [30] R.S. Rubino, E.S. Takeuchi, *J. Power Sources* **1999**, 81, 373.
- [31] M.J. McAllister, J. Li, D.H. Adamson, H.C. Schniepp, A.A. Abdala, J. Liu, M. Herrera-Alonso, D.L. Milius, R. Car, R.K. Prud'homme, I.A. Aksay, *Chem. Mater.* **2007**, 19, 4396.
- [32] Y. Yukselen, A. Kaya, *J. Geotech. Geoenviron. Eng.* **2006**, 132, 931.
- [33] R. Larciprete, S. Gardoniob, L. Petacciab, S. Lizzitb, R. Larciprete, S. Gardoniob, L. Petacciab, S. Lizzitb, *Carbon* **2009**, 47, 2579.
- [34] A. Ganguly, S. Sharma, P. Papakonstantinou, J. Hamilton, *J. Phys. Chem. C* **2011**, 115, 17009.
- [35] S. Ferro, M.D. Colle, A.D. Battisti, *Carbon* **2005**, 43, 1191.

- [36] M. Koinuma, H. Tateishi, K. Hatakeyama, S. Miyamoto, C. Ogata, A. Funatsu, T. Taniguchi, Y. Matsumoto, *Chem. Lett.* **2013**, 42, 924.
- [37] A.C. Ferrari, *Solid State Commun.* **2007**, 143, 47.
- [38] L.M. Malarda, M.A. Pimentaa, G. Dresselhaus, M.S. Dresselhaus, *Phys. Rep.* **2009**, 473, 51.
- [39] M.S. Dresselhaus, A. Jorio, M. Hofmann, G. Dresselhaus, R. Saito, *Nano Lett.* **2010**, 10, 751.
- [40] J. Shen, Y. Hu, M. Shi, X. Lu, C. Qin, C. Li, M. Ye, *Chem. Mater.* **2009**, 21, 3514.
- [41] X. Yan, J. Chen, J. Yang, Q. Xue, P. Miele, *ACS Appl. Mater. Interfaces* **2010**, 2, 2521.
- [42] M.P. Seah, *Thin Solid Films* **1981**, 81, 279.
- [43] G.K. Wehner, *Methods of Surface Analysis*, in: A.W. Czanderna (Ed.), Elsevier, New York, **1975** (Chapter 1).
- [44] M. Acik, G. Lee, C. Mattevi, M. Chhowalla, K. Cho, Y.J. Chabal, *Nature Mater.* **2010**, 9, 840.
- [45] M.A. Raj, S.A. John, *J. Phys. Chem.* **2013**, 117, 4326.
- [46] M.D. Stoller, R.S. Ruoff, *Energy Environ. Sci.* **2010**, 3, 1294.
- [47] J. Xia, F. Chen, J. Li, N. Tao, *Nat. Nanotechnol.* **2009**, 4, 505.
- [48] Y. Matsumoto, M. Koinuma, S. Ida, S. Hayami, T. Taniguchi, K. Hatakeyama, H. Tateishi, Y. Watanabe, S. Amano, *J. Phys. Chem. C* **2011**, 115, 19280.
- [49] G. Eda, Y.Y. Lin, C. Mattevi, H. Yamaguchi, H.A. Chen, I.S. Chen, C.W. Chen, M. Chhowalla, *Adv. Mater.* **2010**, 22, 505.

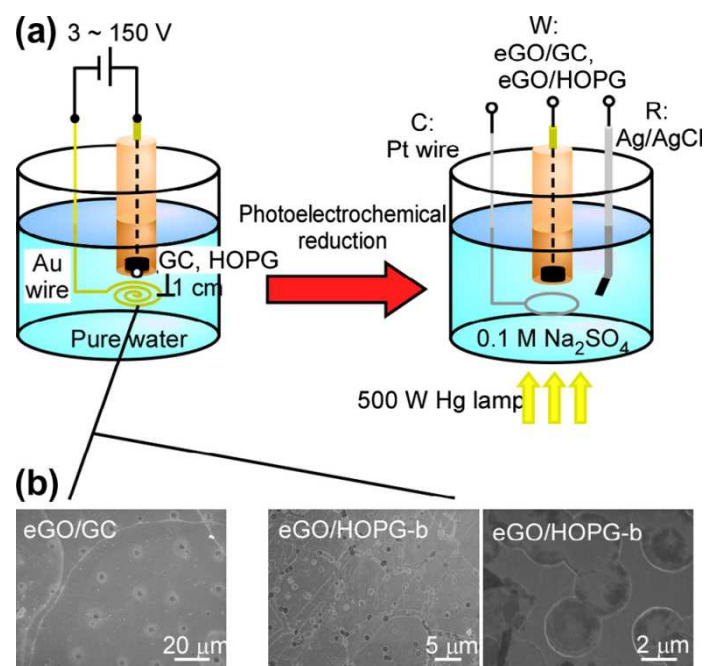


Figure 2-1. Schematic of electrolysis. **(a)** Preparation scheme of eGO in pure water and photoelectrochemical reduction. **(b)** SEM images of eGO surfaces after electrochemical oxidation of GC and HOPG-b electrodes in pure water.

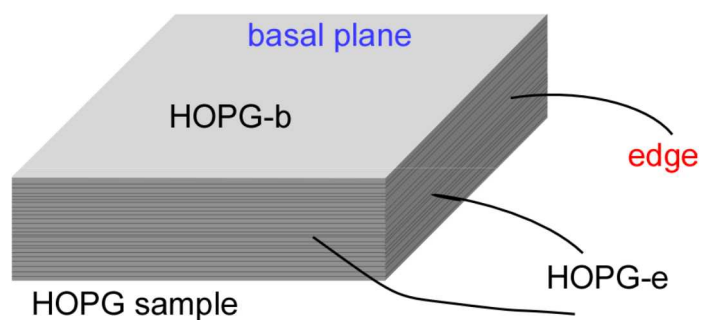


Figure 2-2. HOPG samples: HOPG-b and HOPG-e.

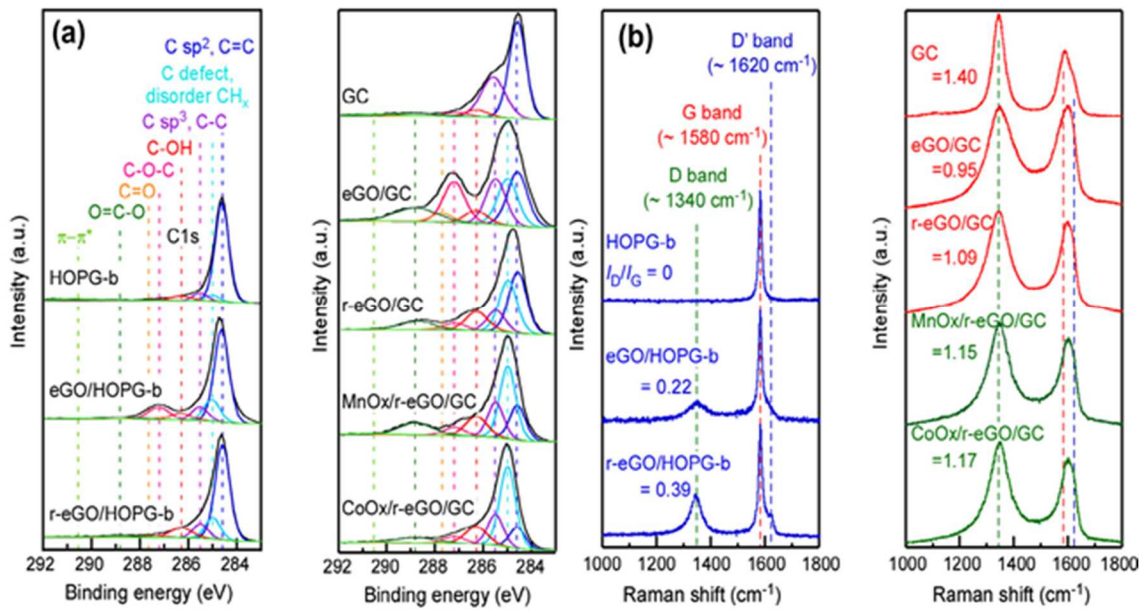


Figure 2-3. The eGO/GC, eGO/HOPG-b, and MO_x/r-eGO/GC electrodes. **(a)** C1s XPS profiles of GC, HOPG-b, eGO/GC, eGO/HOPG-b, r-eGO/GC, r-eGO/HOPG-b, CoO_x/r-eGO/GC, and MnO_x/r-eGO/GC electrodes. **(b)** Raman spectra of the same electrodes.

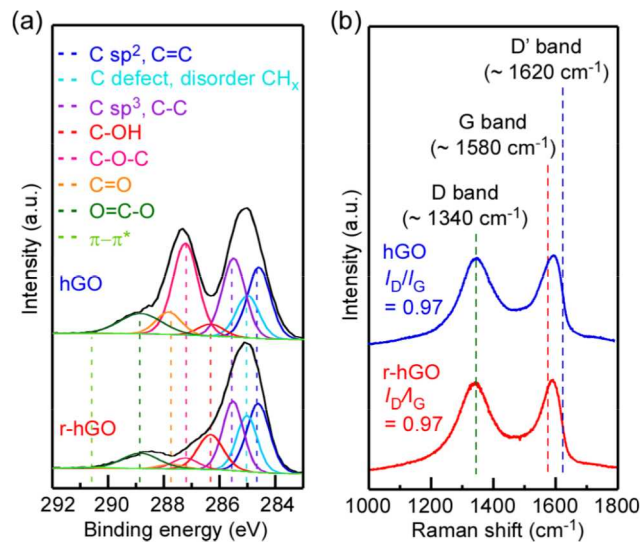


Figure 2-4. hGO and r-hGO electrodes. **(a)** C 1s XPS profiles of hGO and r-hGO electrodes. **(b)** Raman spectra of the same electrodes.

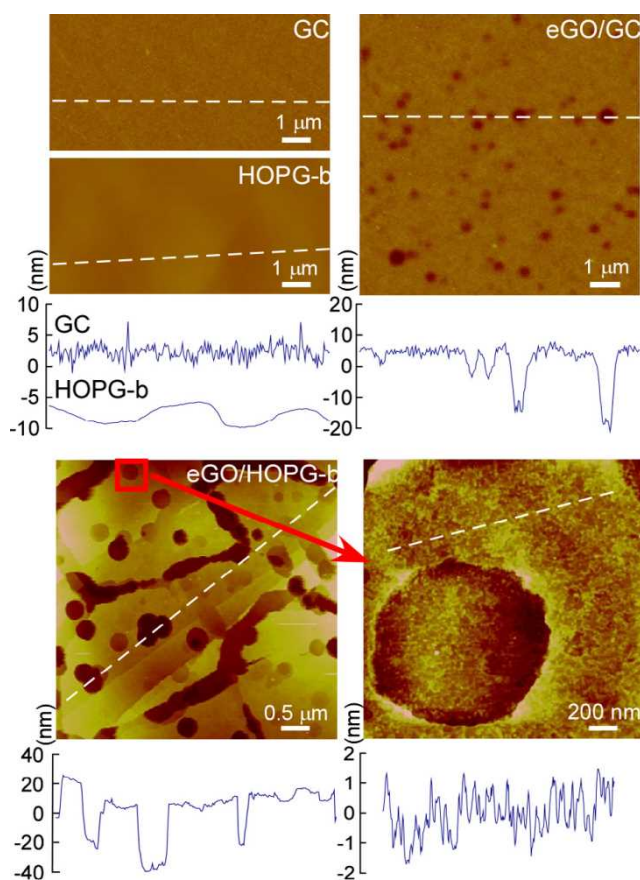


Figure 2-5. AFM images of GC, HOPG-b, eGO/GC, and eGO/HOPG-b surfaces and their depth profiles.

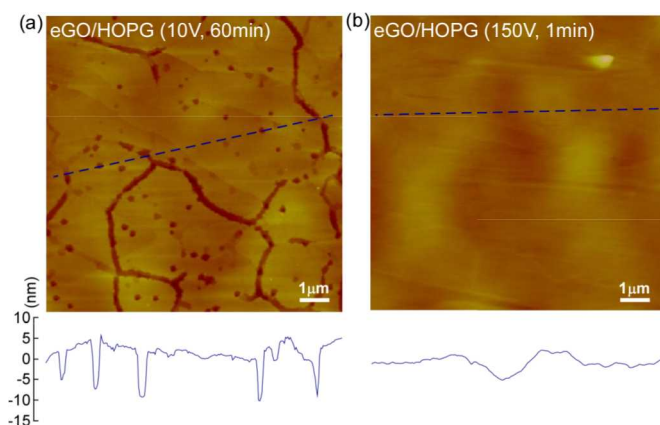


Figure 2-6. AFM images and depth profiles of eGO/HOPG-b prepared under low applied voltage and for short time. **(a)** 10 V for 60 min. **(b)** 150 V for 1 min.

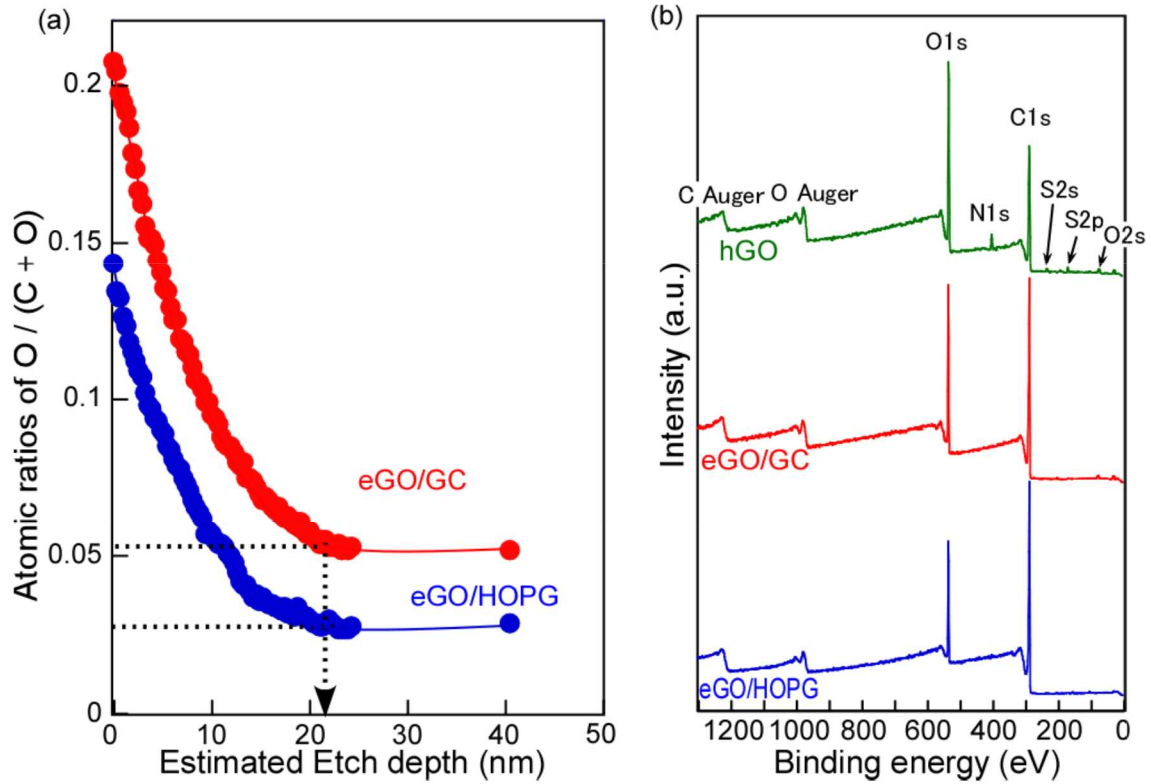


Figure 2-7. (a) Depth profile of eGO/GC and eGO/HOPG measured by XPS. **(b)** XPS spectra of hGO, eGO/GC, and eGO/HOPG

Approximate argon etch rates was calculated form sputter yield data in existing scientific literature.¹ The Sputter Etch Rate, S , in nm/s, is given by;

$$S = (I \cdot Y \cdot A_r) / (100\rho)$$

Where S = Sputter Etch Rate in nm/s

I = Ion Current Density in $\mu\text{A} \cdot \text{mm}^{-2}$ ($0.7 \mu\text{A} \cdot \text{mm}^{-2}$)

Y = Sputter yield (0.4 for carbon)¹

A_r = The sputtered material's relative atomic mass (12.4. This value is assumed that GO contained 10 % of oxygen.)

ρ = The substrate density in $\text{g} \cdot \text{cm}^{-3}$ ($0.43 \text{ g} \cdot \text{cm}^{-3}$. This value is estimated that interlayer spacing of GO was 1 nm and GO contained 10 % of oxygen.)

Thus, S is estimated as 0.081 nm/s.

- Zalar, A., Kovač, J., Praček, B., Panjan, P. & Čeh, M. Ion sputtering rates of W-, Ti- and Cr-carbides studied at different Ar^+ ion incidence angles. *Appl. Surf. Sci.* **2008**, 254, 6611–6618.

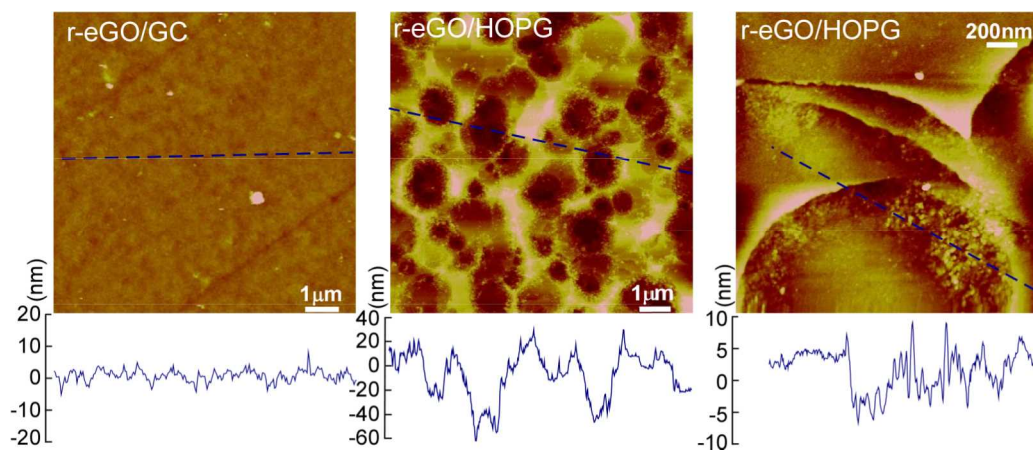


Figure 2-8. AFM images and depth profiles of r-eGO/GC and r-eGO/HOPG-b.

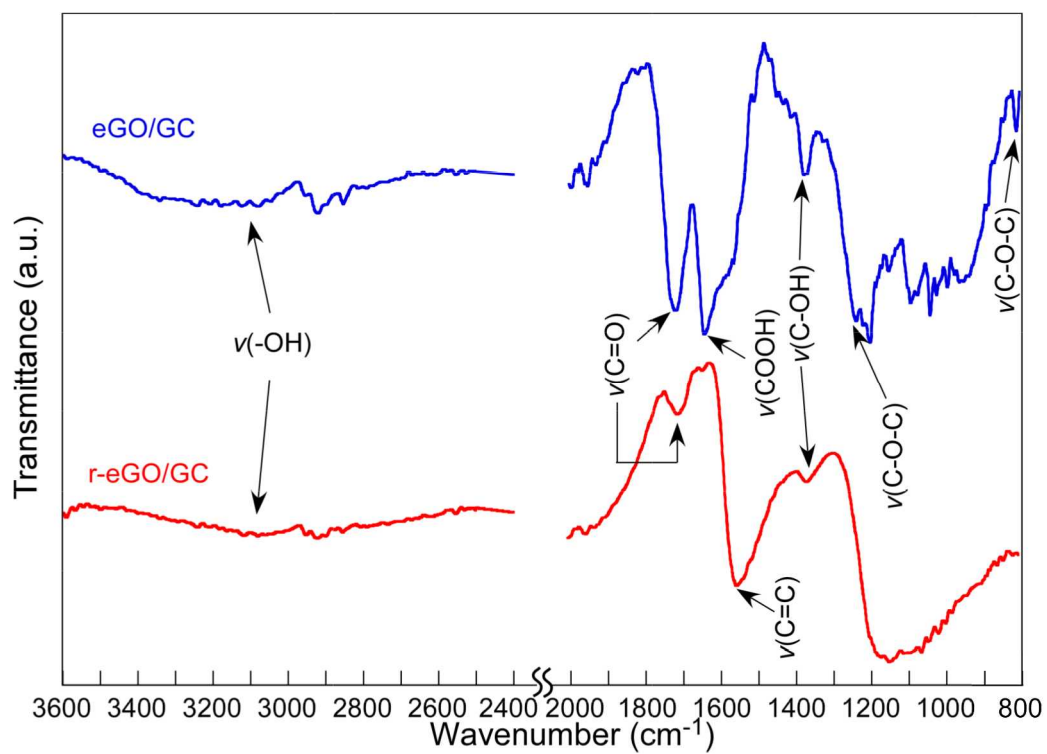


Figure 2-9. ATR-FTIR spectra of eGO/GC and r-eGO/GC

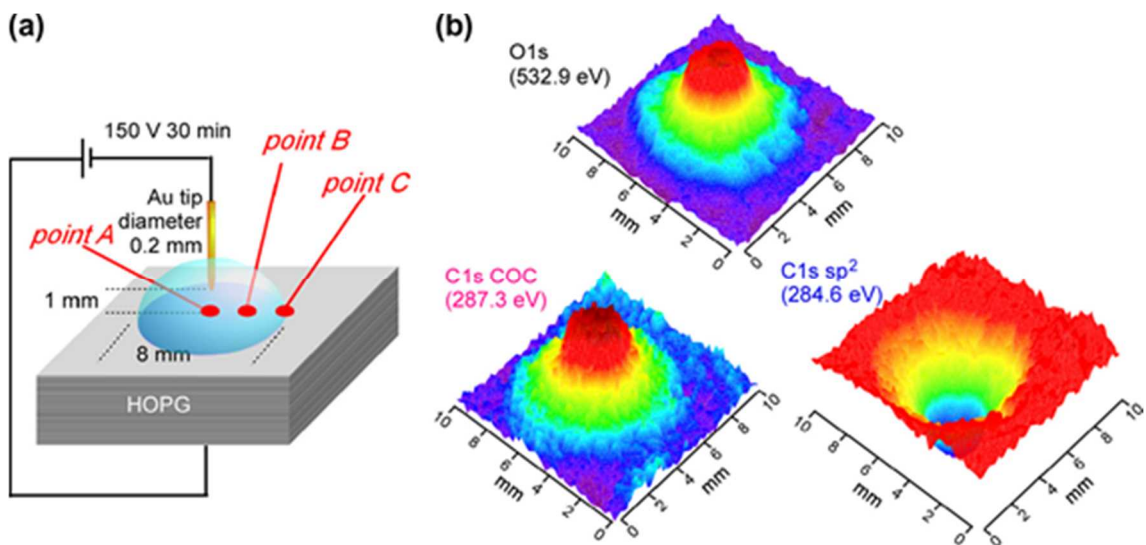


Figure 2-10. Surface analyses of eGO/HOPG-b by XPS. **(a)** Schematic of electrolysis using a water droplet placed on HOPG-b. **(b)** O1s, C1s of COC and sp² XPS intensity maps of prepared eGO surface.

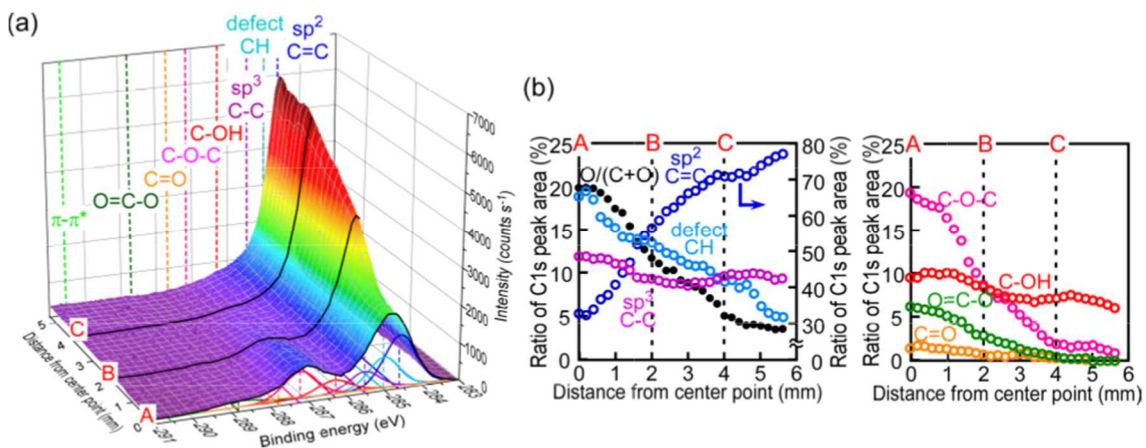


Figure 2-11. **(a)** XPS spectra of C1s for distance from center point. **(b)** XPS quantitative analyses for distance from center point. Points A, B, and C were shown in Figure 2-10(a).

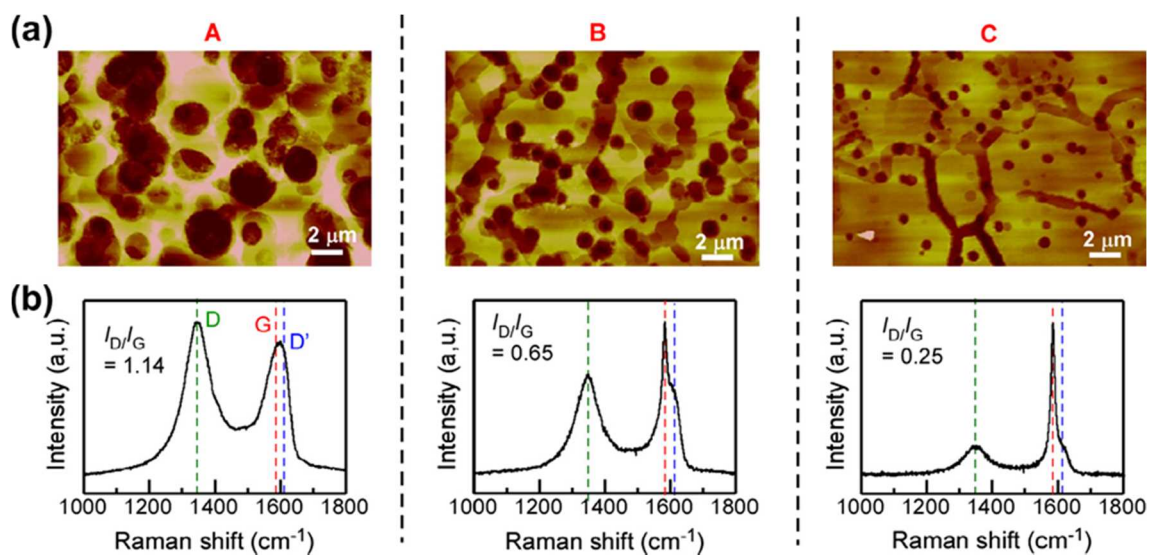


Figure 2-12. AFM images (a) and Raman spectra (b) of points A, B, and C in Figure 2-10.

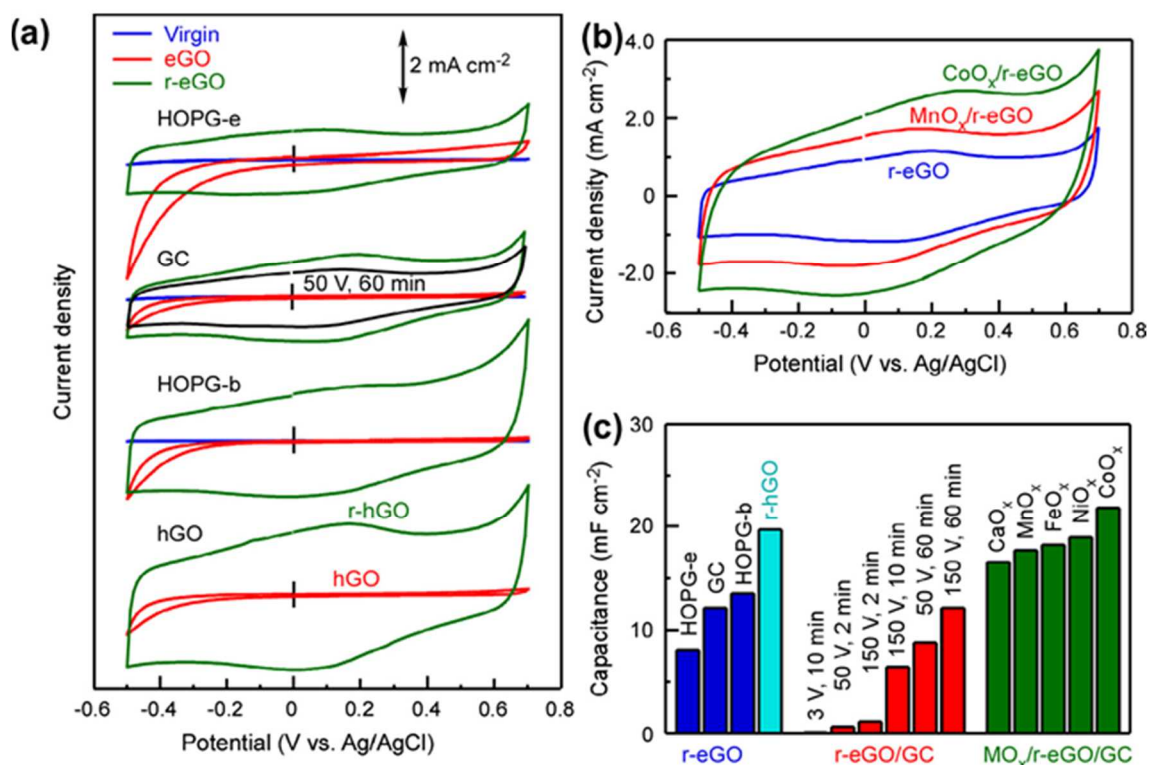


Figure 2-13. eGO as supercapacitor electrode in 0.1 M Na₂SO₄. **(a)** CVs of HOPG-e, eGO/HOPG-e, r-eGO/HOPG-e, GC, eGO/GC, r-eGO/GC, HOPG-b, eGO/HOPG-b, r-eGO/HOPG-b, hGO, and r-hGO electrodes (scan rate = 0.1 V s⁻¹). **(b)** CVs of CoO_x/r-eGO/GC, MnO_x/r-eGO/GC, and r-eGO/GC electrodes (scan rate = 0.1 V s⁻¹). **(c)** Specific capacitances per unit area of r-hGO, r-eGO, and MO_x/r-eGO/GC electrodes.

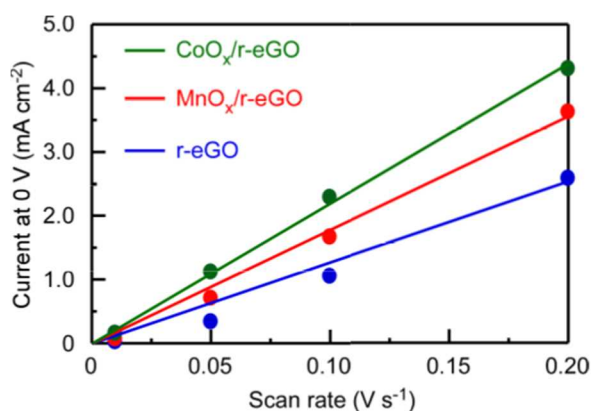


Figure 2-14. Linear relationships between scan rate and current for r-eGO electrodes.

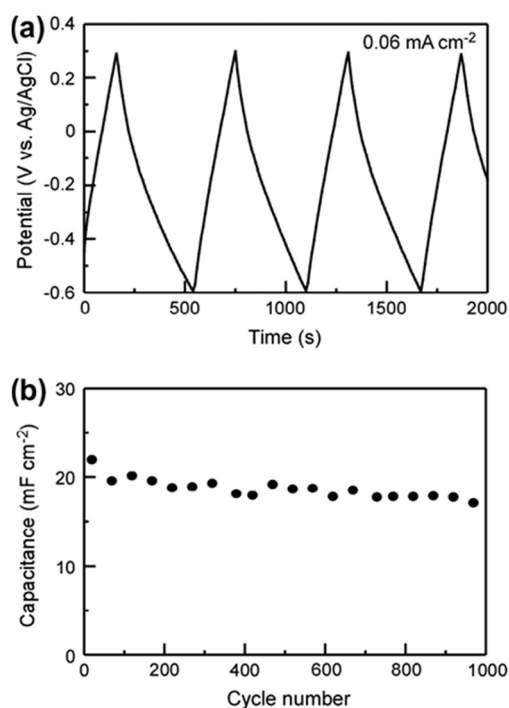


Figure 2-15. (a) Galvanostatic charge–discharge curve of $\text{CoO}_x/\text{r-eGO}/\text{GC}$ electrode at 0.06 mA cm^{-2} . (b) Specific capacitance per unit area of $\text{CoO}_x/\text{r-eGO}/\text{GC}$ electrode as a function of cycle number which was calculated from (a).

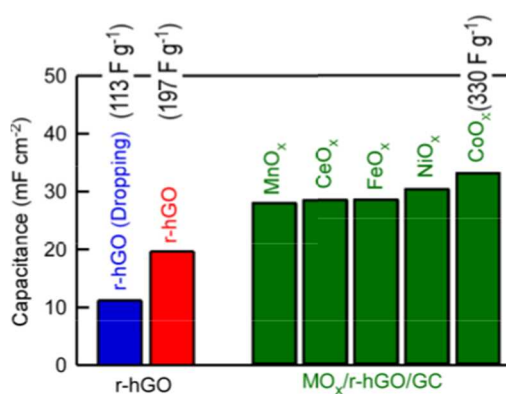


Figure 2-16. Specific weight capacitances of r-hGO and $\text{MO}_x/\text{r-hGO}$ electrodes in $0.1 \text{ M Na}_2\text{SO}_4$. r-hGO (Dropping) is the electrode prepared by dropping hGO suspension onto GC electrode and then drying (0.1 mg cm^{-2}). Other electrodes were prepared by the electrophoretic technique described in the experimental section.

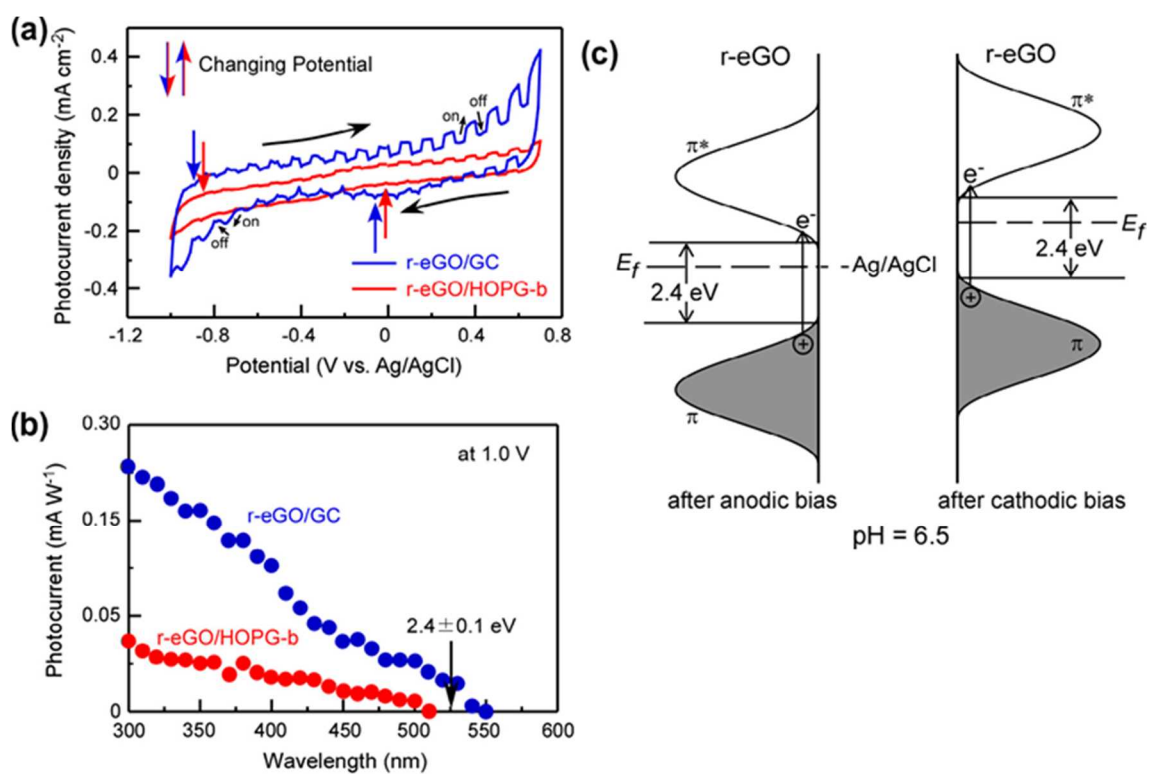


Figure 2-17. Photoelectrochemical properties of r-eGO/GC and r-eGO/HOPG-b electrodes. **(a)** CV curves under chopped-light irradiation (scan rate = 0.01 V s⁻¹). **(b)** Photocurrent as a function of wavelength of irradiated monochromatic light. **(c)** Model of band energy positions of eGO.

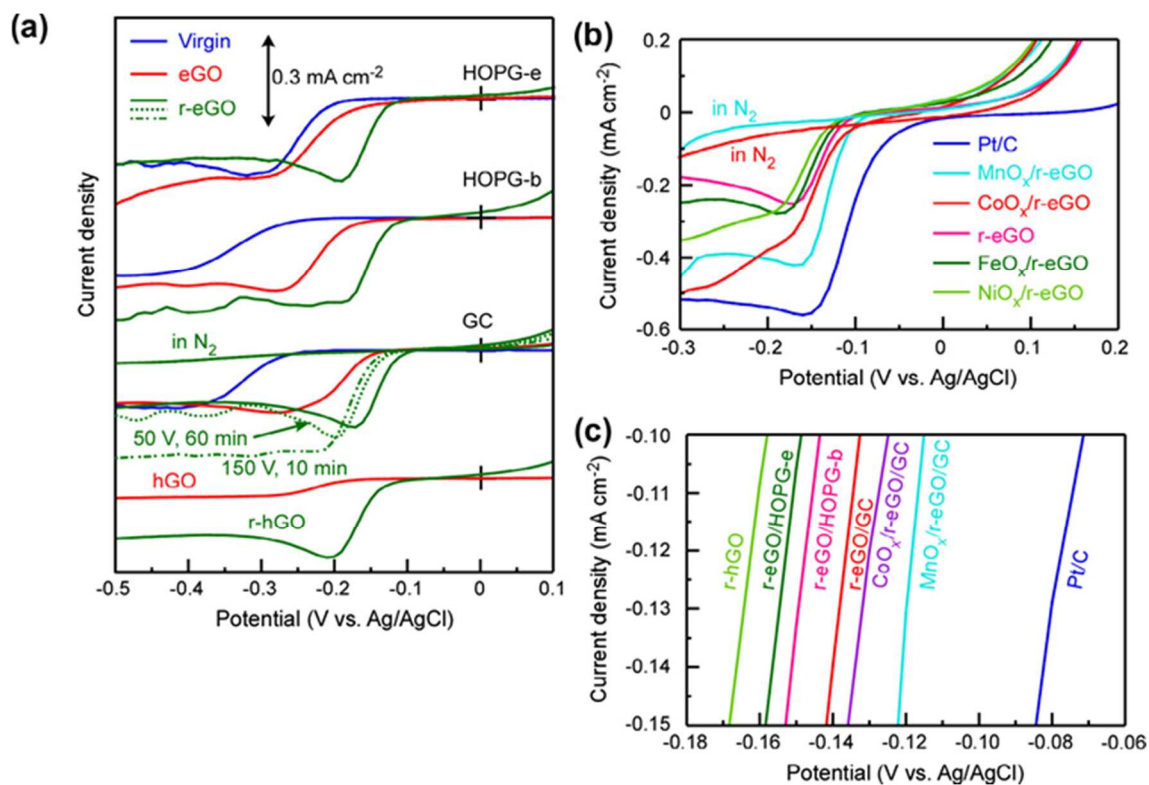


Figure 2-18. Electrocatalytic activities of eGO for ORR. **(a)** I–V curves for ORR at HOPG-e, eGO/HOPG-e, r-eGO/HOPG-e, HOPG-b, eGO/HOPG-b, r-eGO/HOPG-b, GC, eGO/GC, reGO/GC (150 V for 60 min, 150 V for 10 min, 50 V for 60 min), hGO, and r-hGO electrodes. The electrolysis for preparing eGO was performed under 150 V for 60 min, unless otherwise stated. **(b)** I–V curves for ORR at MO_x/r-eGO/GC and commercial Pt/C electrodes. **(c)** I–V curves of some eGO electrodes in the range 100–150 μA.

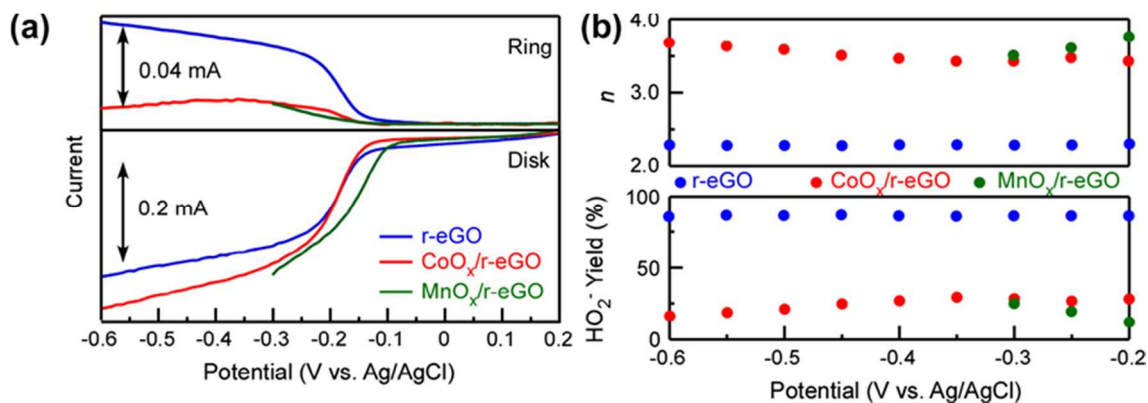


Figure 2-19. Rotating ring (Pt) – disk (r-eGO/GC, CoO_x/r-eGO/GC, and MnO_x/r-eGO/GC) electrodes for ORR at 400 rpm. **(a)** I-V curves of ring and disk electrodes where ring current was measured at disk potential of 0.6 V. **(b)** The *n* and peroxide yield as functions of electrode potential at r-eGO/GC, CoO_x/r-eGO/GC, and MnO_x/r-eGO/GC electrodes.

$$(1) n = 4I_D / (I_D + (I_R/N))$$

$$(2) \text{H}_2\text{O}_2\% = 100(4 - n)/2$$

$$(3) \text{H}_2\text{O}_2\% = 100(2I_R/N) / (I_D + I_R/N)$$

Where I_D is the faradic current at the disk, I_R is the faradic current at the ring, and $N=0.26$ is the RRDE collection efficiency.

Figure 2-20. Equations to calculate *n* and H₂O₂ (HO₂⁻)%

Table 2-1. Functional group content of GO electrodes

Sample	atm%								
	Csp ² C=C	defect CH _x	Csp ³ C-C	C-OH	C-O-C	C=O	O=C-O	π-π*	O/(C+O) ¹⁾
hGO	19.3	11.5	21.3	3.6	27.4	6.6	10.2	0.1	32.1
r-hGO	26.1	20.2	22.7	14.6	4.6	1.9	9.3	0.6	19.5
GC	29.0	0.0	47.2	14.9	3.2	0.0	3.7	2.0	6.5
eGO/GC 150 V 60 min	22.0	19.0	18.6	5.7	18.2	2.9	12.0	0.6	20.9
eGO/GC 10 V 60 min	17.7	37.6	12.5	11.3	5.7	2.1	13.1	0.0	17.2
r-eGO/GC	33.1	28.1	11.3	12.6	4.4	1.6	8.8	0.3	16.0
HOPG-b	79.8	5.8	6.2	3.6	0.7	0.1	0.0	3.9	2.2
eGO/HOPG-b 150 V 60 min	59.0	10.1	9.4	5.8	10.8	2.3	2.0	0.6	12.9
eGO/HOPG-b 10 V 60 min	74.9	7.5	7.8	5.3	2.2	0.5	0.1	1.9	3.2
eGO/HOPG-b 150 V 1 min	68.3	11.5	7.1	5.6	3.2	0.4	2.2	1.8	4.5
r-eGO/HOPG-b	62.0	13.7	9.2	9.5	1.4	1.3	2.4	0.7	7.7
MnO _x /r-eGO/GC	16.4	34.7	16.7	12.9	5.5	0.0	12.8	1.1	61.7
CoO _x /r-eGO/GC	11.8	44.8	16.9	13.1	5.2	0.5	7.2	0.6	14.8

1) O/(C+O) was obtained by elemental analysis of XPS.

CHAPTER 3

Effect of the Reduction Method and Electrochemical Oxidation/Reduction Cycle on the electrochemical capacitance of Graphene Oxide

Overview

Reduction largely affects the properties of graphene oxide (GO) and graphite oxide (GtO; multilayered GO), because the content of each functional group changes by the oxidation degree. In this chapter, we analyzed some reduced GO and GtO (rGO and rGtO) by X-ray photoelectron spectroscopy (XPS). The number of CH defects increased for the photochemical and electrochemical reduction, whereas a direct increase in the number of C=C bonds was observed for thermal and hydrazine-assisted reduction. Cyclic voltammograms showed that the electrochemical capacitance of rGtO increased with the number of CH defects. Moreover, we study about the electrochemical reduced GtO, which has the largest capacitance in these prepared rGO and rGtO, in detail by focusing on its electrochemical oxidation/reduction cycle. According to XPS analysis, C=C bonds were produced from CH defects of the rGtO by the electrochemical re-oxidation. The high electrochemical capacitance observed for the rGtO electrodes is caused by the activity of the CH defects and good conduction.

3.1 Introduction

Graphene oxide (GO) and graphite oxide (GtO; multilayered GO) has many promising chemical and physical properties in the fields of magnetism [1, 2], photoluminescence [3, 4], electrocatalysis [5-7], and as electrochemical supercapacitor electrodes [7-19]. The high specific surface area (SSA) of GO is a very important factor for supercapacitor electrodes, and the SSA value may be

as high as $2630 \text{ m}^2 \text{ g}^{-1}$ if it is assumed to be similar to that of graphene [8, 11, 12]. Its performance as a supercapacitor electrode is drastically enhanced by the reduction of GO and GtO to produce reduced graphene oxide (rGO) and reduced graphite oxide (rGtO) with high conductivity. Although the high SSA value and high conductivity of rGO and rGtO are important factors contributing to its high capacitance, the presence of suitable functional groups to rGO and rGtO are another significant factor [7, 15–19]. The later factor will affect the Faradaic electrochemical reaction (i.e. pseudocapacitive redox reaction) of the functional groups [7, 16–19].

Typically, rGO is prepared by the thermal [20–23], hydrazine-assisted [23–26], or photochemical [27–29] reduction of GO. Although these treatments produce similar increases in the electrical conductivity, the increasing rate of that depends on the treatment conditions. However, a detailed analysis of the functional groups in rGOs prepared by various reduction methods, particularly of the non-oxygenated functional groups ($\text{sp}^3 \text{ C-C}$, $\text{sp}^3 \text{ CH}$, and $\text{sp}^2 \text{ C=C}$ bonds), has never been performed. We analyzed GO and rGO by X-ray photoelectron spectroscopy (XPS) and deconvoluting the C1s binding energies of the functional groups. Analysis of the CH defects is very important because they are key functional groups in rGO supercapacitor electrodes [7].

In this chapter, we demonstrate the importance of the CH defects on the electrochemical capacitance and the dependence of the differences in the functional groups of the rGO samples, particularly the CH defects, on the reduction method. Moreover, we focused on electrochemical reduced GO, which exhibits higher capacitance as compared with other reduction methods, and researched about the mechanisms of oxidation/re-oxidation and reduction/re-reduction to more understand the origin of high capacitance. The XPS analysis indicates that C=C bonds, not COC epoxides, are produced from CH defect, which is the origin of high capacitance, of rGtO by its re-oxidation.

3.2 Experimental

3.2-1 Preparation of materials

Two types of GO samples were prepared by different methods. The GO sample was prepared by the conventional Hummers' method [30], using 98% graphite powder (Wako Chemicals) as the starting material. The GtO sample was prepared by the electrochemical oxidation of glassy carbon (GC, BAS Ltd.) in 0.1 M Na₂SO₄ (Wako Chemicals) at 2.0 V (vs. Ag/AgCl) for 30 min. The electrochemical reduction of GtO was performed at -1.1 V in 0.1 M Na₂SO₄ for 30 min. Photochemical, thermal, and hydrazine-assisted reduction were conducted on both samples. The photochemical reduction was carried out under a 500 W Hg lamp for 1 h in H₂. The thermal reduction was carried out in Ar at 300 °C for 30 min. For the hydrazine-assisted reduction, the samples were immersed in a 10 M aqueous hydrazine solution at 60 °C for 6 h.

3.2-2 Oxidation/reduction cycle

GC electrode was employed as the electrode material to produce GtO_{*n*} and r_{*n*}GtO (*n* = the oxidation/reduction cycle number) films electrochemically on its surface. Pt wire and Ag/AgCl were used as the counter and reference electrodes, respectively. At first, GtO was prepared by the oxidation of GC electrodes in a 0.1 M Na₂SO₄ solution at +1.5 to 2.0 V (vs. Ag/AgCl) for 30 min. The subsequent electrochemical reduction of GtO was conducted in the same solution at -1.1 V for 30 min. The re-oxidation and re-reduction cycles were carried out at +2.0 V (oxidation) and -1.1 V (reduction), respectively, unless otherwise stated.

3.2-3 XPS measurement

The XPS measurements were carried out using a Thermo Scientific SigmaProbe and monochromatic Al K α radiation. The instrument work function was calibrated to give a binding energy (BE) of 83.95 eV for the Au4f_{7/2} line for metallic gold. The spectrometer dispersion was

adjusted to give a BE of 368.25 eV for metallic Ag3d_{5/2} and 932.65 eV for metallic Cu2p_{3/2}. The instrument base pressure was 1×10^{-9} mbar. High-resolution spectra were collected with a pass energy of 15 eV, which corresponds to a Ag3d_{5/2} full width at half-maximum of 0.47 eV. The relative sensitivity factors (RSFs) used for quantitative analysis were adapted from the empirical RSF collection reported by Scofield [31].

The GO and rGO samples were prepared by dropping a nanosheet suspension of the sample onto a metallic Au substrate, which was cleaned with Milli-Q (>18 MΩ) water, methanol (Wako Chemicals), and a hydrogen flame because it has high conductivity and contains very little oxygen on its surface. The reference samples for deconvoluting the C1s binding energy were diamond (single-crystal (100), Sumitomo Electric, Type-Ib), highly oriented pyrolytic graphite (HOPG; NT-MDT Co, Type-ZYB), hydroquinone (Wako Chemicals), sodium terephthalate, and sodium dodecanedioate. Sodium terephthalate and sodium dodecanedioate were prepared by adding 1 M NaOH (Wako Chemicals) to terephthalic acid (Wako Chemicals) and dodecanedioic acid (Wako Chemicals) dissolved in methanol, respectively. Hydroquinone, sodium terephthalate, and sodium dodecanedioate were dissolved in methanol on the Au substrate and then dried under vacuum. No charge neutralization was needed for the thin layer on the Au substrate. All spectra were referenced to the Au 4f_{7/2} peak at 83.95 eV.

3.2-4 Characterization and electrochemical measurement

Cyclic voltammetry utilized to measure the electrochemical capacitances of all the single-electrode samples, was carried out using three-electrode electrochemical cells with a potentiostat and a function generator (Ivium Compactstat) in a 0.1 M Na₂SO₄ solution. Raman spectroscopy (Jasco, NRS-3100) were employed to analyze the surface of all samples. The 532 nm excitation source was used for Raman spectroscopy. The surface morphologies of the samples were

observed by atomic force microscopy (AFM, Digital Instruments Nanoscope V, tapping mode). The surfaces of the samples (1 cm^2) were soaked in a $1 \text{ }\mu\text{M}$ methylene blue (MB) aqueous solution for 30 min, and then the MB solution concentration was measured by UV-vis spectrometry (Jasco, V-550) to determine the amount of MB adsorption on the samples. The relative surface areas (SAs) of the samples were calculated using the literature value of 1.30 nm^2 of the surface covered per molecule of MB [32–34]. The measured or calculated SA only gives a relative value, since MB adsorption occurred for $r_n\text{GtO}$ but not for GtO_n samples because of π - π interaction for former sample. The resistances of the samples were measured using the mercury (Hg) pool system shown in Figure 3-1(a).

3.3 Results and Discussion

3.3-1 Analysis of GO and rGO by XPS

Figure 3-2 shows the XPS C1s spectra of GO and GtO; the spectra of diamond, HOPG, and the organic compounds (sodium terephthalate, sodium dodecanedioate, and hydroquinone) are also shown to confirm the suitability of the deconvolution. Diamond (Figure 3-2(c)) and HOPG (Figure 3-2(d)) exhibited sharp single peaks and gave sp^3 C-C and sp^2 C=C bonding energies [35–38], respectively. Sodium terephthalate (Figure 3-2(e)) and sodium dodecanedioate (Figure 3-2(f)) gave peaks corresponding to the carboxylate $\text{O}=\text{C}-\text{O}^-$ group and the sp^3 CH bond, respectively. The energy position of the carboxylate $\text{O}=\text{C}-\text{O}^-$ group was determined by using the energy position of the HOPG sp^2 C=C for sodium terephthalate, because only the sp^2 C=C and carboxylate $\text{O}=\text{C}-\text{O}^-$ groups are present in sodium terephthalate. Similarly, the energy position of CH [39] was determined from the sodium dodecanedioate spectrum. The energy positions of the hydroxide C-OH and the carbonyl C=O groups were obtained from hydroquinone (Figure 3-2(g)) during the oxidation of hydroquinone to quinone. The binding energy of the epoxide C-O-C peaks (287.2 eV) has been previously reported [22, 27, 40]. The deconvolution consisted of the sp^2 C=C (284.6 eV), CH (285.0 eV), sp^3 C-C (285.5

eV), C-OH (286.4 eV), C-O-C (287.2 eV), C=O (287.7 eV), and O=C-O⁻ (288.8 eV) peaks. The deconvolution using the three peaks from non-oxygenated groups for diamond (sp³ C-C), HOPG (sp² C=C), and sodium dodecanedioate (CH) is critical to the analysis of rGO and rGtO. Consequently, this C1s deconvolution of the seven elements is the most suitable for analyzing the many groups in GO and rGO that have been reported in XPS studies [20-22, 24-26, 41-44].

Figure 3-3 shows the C1s XPS spectra of rGO and rGtO prepared by various reduction methods. The main C-O-C groups in GO decreased sharply for all methods. The group contents are listed in Table 3-1. The most important difference was that the CH defects were produced by the photochemical and electrochemical reduction but not by the thermal and hydrazine-assisted reduction. The latter two methods form sp² C=C bonds by reducing C-O-C bonds, although N was observed for the hydrazine-assisted reduction. Therefore, the C-N bond was added to the energy position of 285.9 eV in the C1s deconvolution of the hydrazine-assisted reduction [24].

3.3-2 Effect of reduction methods

In the electrochemical reduction method, the CH defects significantly affect the electrochemical capacitance. The cyclic voltammograms (CVs) of rGtO prepared by reducing GtO are shown in Figure 3-4. The reduction increased the capacitance current, mainly because of the increase in conductivity. The resistance of rGtO is shown in Figure 3-1(b) and was approximately 12, 12, 3, and $2.5 \times 10^3 \Omega$ for the samples treated by thermal, hydrazine-assisted, electrochemical, and photochemical reduction, respectively. The resistance of the photoreduced sample was high because the bonds in the interior GO layers were not reduced; the photochemical reduction occurred at the surface. Therefore, we measured the capacitance of the three samples that showed good conduction. The capacitance current of the rGtOs prepared by the electrochemical method, which contained a large number of the CH defects, was the highest among the three samples. This result indicates that

the CH defects significantly affected the capacitance current. The large capacitance can be attributed to the CH defects, based on the following Faradaic redox reaction (pseudocapacitance).



Effect of the electrochemical oxidation/reduction cycle on the electrochemical capacitance of GO.

3.3-3 Effect of oxidation/reduction cycle and reaction mechanism

Figure 3-5(a) shows the CVs of the GC, GtO, and rGtO electrodes. To produce rGtO, the reduction potential employed was -1.1 V (vs. Ag/AgCl) for all samples, because the capacitance current increased with more negative potential but saturated at -1.1 V in the reduction electrolysis process. Capacitance currents were observed for the rGtO electrodes, but the current was higher for electrodes prepared under a high positive potential (+2.0 V) during the oxidation electrolysis process, while lower currents were observed for the GC and GtO electrodes, as shown in Figure 3-5(a). The re-oxidized sample is denoted as GtO_{*n*}, where *n* is re-oxidation cycle number (for example, the sample oxidized three times is denoted as GtO₃). On the other hand, the re-reduced sample is denoted as r_{*n*}GtO (for example, the sample reduced three times is denoted as r₃GtO). The dependences of the capacitances on the oxidation/reduction cycle are shown in Figure 3-5(b). Three phenomena are observed from Figure 3-5(b). First, the capacitance of r_{*n*}GtO is always about 10² times higher than that of GtO_{*n*}, for a given value of *n*. The capacitances per apparent surface area were determined to be about 50~200 mF cm⁻² for r_{*n*}GtO, while those for GtO_{*n*} were <2 mF cm⁻² (inset of Figure 3-5(b)). Second, the capacitances were always greater for r_{*n*}GtO prepared at a higher oxidation potential. For example, r_{*n*}GtO prepared at +2.0 V had the highest capacitance of all the r_{*n*}GtO electrodes. Third, the capacitances of the r_{*n*}GtO samples increased with increasing values of *n* (i.e., the oxidation/reduction cycle number).

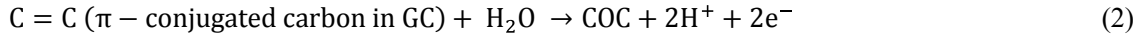
The first phenomenon may be related to the resistance of the film samples. We measured

the $r_n\text{GtO}$ and GtO_n electrode resistances, obtained from the I/V linear relationships evaluated using the Hg pool system illustrated in Figure 3-6. Figure 3-5(c) shows the dependences of the sample resistances on the electrochemical oxidation/reduction cycle. The resistances of the GtO_n electrodes were always much higher than those of the $r_n\text{GtO}$ electrodes prepared under the +2 V oxidation preparation condition, but not in the case of the +1.5 V oxidation preparation condition.

It is considered that the resistance will depend on the oxygen content rather than the kind of carbon bonds (CH defects and new produced C=C bonds) for the present GtO_n and $r_n\text{GtO}$ samples. Probably, the intercalated oxygen species (oxygen functional groups and water) may suppress the electron movement. Thus, a high resistance for the GtO_n electrode will tend to suppress the charge-discharge current flow during the capacitance measurements, in the case of the +2 V oxidation process. However, even though the $r_n\text{GtO}$ electrodes prepared at +1.5 V have nearly the same low values of resistance as those prepared at +2 V, as shown in Figure 3-5(c), the capacitances of the latter were much higher than those of the former (see Figure 3-12(a)), as will be discussed later in detail. Thus, it can be reasonably assumed that the high capacitance of the $r_n\text{GtO}$ electrodes prepared at +2 V is attributed to the activity of the functional groups and to good conduction.

Figure 3-7(a) shows the XPS spectra of the GtO_n and $r_n\text{GtO}$ electrodes. Analysis of these spectra [7, 22, 39, 45] indicates that C-O-C was the main product after the first oxidation (for GtO) and that CH defect was the primary product after the reduction of GtO ($r\text{GtO}$). It should be noted that the degree of oxidation of the re-oxidized samples of the GtO_n electrodes did not increase significantly, rather the extent of the production of C=C bond increased, while the CH defect increased again by the re-reduction of the $r_n\text{GtO}$ electrodes. This observation indicates that the CH defect is a very significant factor for high capacitance. Dependences of the contents of CH defects on the oxidation/reduction cycle are shown in Figure 3-7(b). The tendencies observed for the content of the CH defect corresponds well to the magnitude of the capacitance shown in Figure 3-5(b).

Initially, the following oxidation reaction will proceed to produce the C-O-C during high positive potential electrolysis:



The following main reaction to produce CH defects in rGtO will proceed from the COC groups of GtO during the initial reduction:



During the re-oxidation to produce GtO₂, the C=C bonds will be produced as follows,



And then, the reverse reaction of Eq. (4) will occur for the production of r₂GtO. The C=C produced in reaction (4) will be different from that produced in GC (π -conjugated carbon) in bonding state, because no C-O-C are produced during the high positive potential electrolysis of rGtO and r₂GtO, and the new produced C=C never causes an increase in the conductivity (Figure 3-5(c)). We assumed that the formation of C=C bonds caused the high resistance. Because C=C (sp²) carbon existed as non-conjugated bonds, such as C=C=C, the electron transfer within GtO_n was restricted. The Raman spectra of G and D bands and their intensity ratio (I_D/I_G) are shown in Figure 3-8, respectively. The electrochemical reduction causes an increase of I_D , suggesting the increase of defects [46, 47], in harmony with the observed increase in CH defect.

The second phenomenon suggests that the positive potential sufficiently high to produce C-O-C for the initial oxidation reaction (Eq. (2)) is necessary because the C-O-C are the reactant to produce the CH defect in the subsequent reduction process (Eq. (3), i.e., the trigger reaction to produce the CH defect). As shown in Figure 3-9, the contents of the C-O-C and the CH defects are small for the GtO and rGtO produced at +1.5 and +1.7 V, compared with that produced at +2.0 V. As a matter of course, Eq. (4) and its reverse reaction to produce the CH defect is small with respect to the product content, as shown in Table 3-2.

The third phenomenon can be explained by postulating an increase of the SA with the oxidation/reduction cycle. Figure 3-10 shows AFM images of GtO_n and r_nGtO sample surfaces. Some pores of about submicron radii are produced during the first oxidation, and their depths and roughness somewhat increased by the oxidation/reduction cycle. In the present study, the root mean squared (RMS) roughness of the surface is defined as $R_{RMS} \text{ (nm)} = [\sum(Z_i - Z_{ave})^2/N]^{1/2}$, where z_i is the current value of z , z_{ave} is the mean value of z in the scan area, and N is the number of points. The RMS roughnesses obtained using a $1 \times 1 \mu\text{m}$ scan window without pores (Figure 3-10(a)), of a relatively flat domain, were 0.99, 1.11, and 1.33 nm for GtO , GtO_2 , and GtO_3 , respectively. Moreover, the RMS roughnesses of $rGtO$, r_2GtO , and r_3GtO , which were calculated in a similar way, were 1.04, 1.14, and 1.10 nm, respectively. In the relatively flat domain, the surface roughness did not depend on the number of reductions, although the electrode surface became coarser gradually as the number of oxidations increased. In contrast, R_{RMS} in domains including the holes (Figure 3-10(b), scan size $30 \times 30 \mu\text{m}$) increased with the number of electrochemical oxidation/reduction cycles. Therefore, the number of holes on the surface was the main factor in the increase in the SA, because R_{RMS} estimated from the AFM images of relatively flat domains did not increase in the same way as the value of SA during the electrochemical reduction/oxidation cycle. We also measured the amount of MB adsorbed onto the sample surfaces. Dependence of the SA calculated from the amounts of the adsorption on the cycle is shown in Figure 3-11. The relative SA of the $rGtO$ electrode increased by about 3.8 times after four cycles (i.e., for r_4GtO), while the increase of the capacitance was about 3.5 times higher (Figure 3-5(b)). The increase of the SA is based on that of GtO produced already by the reaction (4) cycles, because no production of C-O-C was observed for GtO_2 and GtO_3 as shown in Figure 3-7(a).

However, the following results indicate that the CH defect, rather than the SA, is a much more important factor for high capacitance. Figure 3-12(a) shows the change of the capacitance with

that of the oxidation potential (+1.5 and +2.0 V) in the oxidation/reduction cycle where the reduction was conducted at -1.1 V. The capacitance was very low in the interval of the oxidation of +1.5 V compared with that of +2.0 V oxidation. Of special note, the capacitance was found to decrease for $r_n\text{GtO}$ in the oxidation interval conducted at +1.5 V, after the +2.0 V oxidation process, in spite of an observed increase of the SA. This fact indicates that the increase of the SA is not the most significant factor for obtaining high capacitance. Moreover, the conductance was high for the $r_n\text{GtO}$ electrode prepared at +1.5 V during the oxidation process (Figure 3-5(c)). Figure 3-13 shows the XPS spectra and contents of the CH defect of the $r_n\text{GtO}$ samples prepared by the +1.5 V oxidation process after the +2.0 V oxidation process. The content of the CH defect is found to decrease after the +1.5 V oxidation process. Figure 3-12(b) shows the relationship between the capacitance and the content of the CH defect for $r_n\text{GtO}$. The capacitance roughly increases with an increase in the contents of the CH defect in spite of the presence of the described SA effect. Thus, it must be concluded that the CH defect is the primary factor for obtaining high capacitance.

The Faradaic reaction of the CH defect bringing about high pseudocapacitance will proceed in Eq. (1). The CH defect will be very active chemically, if it is in a zigzag edge [48]. In this case, the electrochemical electron accumulation and release at the CH defects may be possible. The average thickness of $r_n\text{GtO}$ and GtO_n was estimated to be about 20 nm, according to calculations conducted using the sputter depth profiles of oxygen obtained by XPS with argon etching [49, 50]. The effect of oxide layer thickness on the number of electrochemical oxidation/reduction cycles was negligible. These XPS depth profiles suggested that the thickness of the oxide layer in $r_n\text{GtO}$ was governed by the first electrochemical oxidation. The specific weight capacitances of $r_n\text{GtO}$ were estimated to be about $6 \times 10^4 \text{ F g}^{-1}$, if the thickness of $r_2\text{GtO}$ is about 20 layers. Even if the thickness of $r_2\text{GtO}$ is assumed to be the same as the pore depth of about 200 nm (Figure 3-10(b)), the estimated specific weight capacitance is $6 \times 10^3 \text{ F g}^{-1}$. Anyhow, the specific gravity capacitance of

r_nGtO is huge. In these cases, it was estimated that ~100% of all the CH defects react at electrolyte interface in the interlayer and at the surface.

3.4 Conclusions

We used XPS to analyze rGO and rGtO prepared by various reduction methods and measured their electrochemical capacitances. The deconvolution of the C1s binding energies for seven elements was well suited to analyzing the various functional groups of GO and rGtO, particularly the non-oxygenated functional groups of the sp³ C-C bond, CH defects, and the sp² C=C bond. An increase in the number of CH defects was observed in rGO and rGtO prepared by photochemical and electrochemical reduction but not for those prepared by thermal and hydrazine-assisted reduction. The CH defects significantly affected the electrochemical capacitance because the capacitance was the largest for the rGtO prepared by the electrochemical reduction, which contained a large number of CH defects. We also found that the mechanism about oxidation/reduction cycle. C=C bonds were produced from CH defects by the electrochemical re-oxidation of the rGtO, while C-O-C epoxides were produced from GC by the first electrochemical oxidation. The conduction of the re-oxidation sample, containing the newly produced C=C bonds, was poor, while that of the reduced sample, containing CH defects, was high. The increase in the capacitance of the rGtO, with respect to the electrochemical oxidation/reduction cycle, is due to the increase of the surface area of rGtO produced by the C=C/CH reaction cycle.

References

- [1] Y. Wang, Y. Huang, Y. Song, X. Zhang, Y. Ma, J. Liang, Y. Chen, *Nano Lett.* **2009**, 9, 220.
- [2] Y. Matsumoto, M. Koinuma, S. Ida, S. Hayami, T. Taniguchi, K. Hatakeyama, H. Tateishi, Y. Watanabe, S. Amano, *J. Phys. Chem. C* **2011**, 115, 19280.
- [3] K. P. Loh, Q. Bao, G. Eda, M. Chhowalla, *Nat. Chem.* **2010**, 2, 1015.
- [4] J. Shen, Y. Zhu, C. Chen, X. Yang, C. Li, *Chem. Commun.* **2011**, 47, 2580.
- [5] L. Qu, Y. Liu, J. B. Baek, L. Dai, *ACS Nano* **2010**, 4, 1321.
- [6] Y. Liang, Y. Li, H. Wang, J. Zhou, J. Wang, T. Regier, H. Dai, *Nat. Mater.* **2011**, 10, 780.
- [7] Y. Matsumoto, H. Tateishi, M. Koinuma, Y. Kamei, C. Ogata, K. Gezuhara, K. Hatakeyama, S. Hayami, T. Taniguchi, A. Funatsu, *J. Electroanal. Chem.* **2013**, 704, 233.
- [8] M. D. Stoller, S. Park, Y. Zhu, J. An, R. S. Ruoff, *Nano Lett.* **2008**, 8, 3498.
- [9] Y. Wang, Z. Shi, Y. Huang, Y. Ma, C. Wang, M. Chen, Y. Chen, *J. Phys. Chem. C* **2009**, 113, 13103.
- [10] Y. Huang, J. Liang, Y. Chen, *Small* **2012**, 8, 1805.
- [11] Y. W. Zhu, S. Murali, M. D. Stoller, K. J. Ganesh, W. W. Cai, P. J. Ferreira, A. Pirkle, R. M. Wallace, K. A. Cyhosh, M. Thommers, D. Su, E. A. Stach, R. S. Ruoff, *Science* **2011**, 332, 1537.
- [12] M. F. El-Kady, V. Strong, S. Dubin, R. B. Kaner, *Science* **2012**, 335, 1326.
- [13] J. J. Yoo, K. Balakrishnan, J. Huang, V. Meunier, B. G. Sumpter, A. Srivastava, M. Conway, A. L. M. Reddy, J. Yu, R. Vajtai, P. M. Ajayan, *Nano Lett.* **2011**, 11, 1423.
- [14] L. L. Zhang, X. Zhao, M. D. Stoller, Y. Zhu, H. Ji, S. Murali, Y. Wu, S. Perales, B. Clevenger, R. S. Ruoff, *Nano Lett.* **2012**, 12, 1806.
- [15] J. Yan, J. Liu, Z. Fan, T. Wei, L. Zhang, *Carbon* **2012**, 50, 2179.
- [16] D. A. C. Brownson, C. E. Banks, *Chem. Commun.* **2012**, 48, 1425.

- [17] J. Yang, S. Gunasekaran, *Carbon* **2013**, 51, 36.
- [18] C. M. Chen, Q. Zhang, M. G. Yang, C. H. Huang, Y. G. Yang, M. Z. Wang, *Carbon* **2012**, 50, 3572.
- [19] B. Zhao, P. Liu, Y. Jiang, D. Pan, H. Tao, J. Song, T. Fang, W. Xu, *J. Power Sources* **2012**, 198, 423.
- [20] O. Akhavan, *Carbon* **2010**, 48, 509.
- [21] D. Yang, A. Velamakanni, G. Bozoklu, S. Park, M. Stoller, R. D. Piner, S. Stankovich, I. Jung, D. A. Field, C. A. Ventrice, Jr., R. S. Ruoff, *Carbon* **2009**, 47, 145.
- [22] A. Ganguly, S. Sharma, P. Papakonstantinou, J. Hamilton, *J. Phys. Chem. C* **2011**, 115, 17009.
- [23] X. Gao, J. Jang, S. Nagase, *J. Phys. Chem. C* **2010**, 114, 832.
- [24] S. Stankovich, D. A. Dikin, R. D. Piner, K. A. Kohlhaas, A. Kleinhammes, Y. Jia, Y. Wu, S. B. T. Nguyen, R. S. Ruoff, *Carbon* **2007**, 45, 1558.
- [25] S. Park, J. An, J. R. Potts, A. Velamakanni, S. Murali, R. S. Ruoff, *Carbon* **2011**, 49, 3019.
- [26] S. Park, Y. Hu, J. O. Hwang, E.-S. Lee, L. B. Casabianca, W. Cai, J. R. Potts, H.-W. Ha, S. Chen, J. Oh, S. O. Kim, Y.-H. Kim, Y. Ishii, R. S. Ruoff, *Nat. Commun.* **2012**, 3, 638.
- [27] Y. Matsumoto, M. Koinuma, S. Y. Kim, Y. Watanabe, T. Taniguchi, K. Hatakeyama, H. Tateishi, S. Ida, *ACS Appl. Mater. Interfaces* **2010**, 2, 3461.
- [28] M. Koinuma, C. Ogata, Y. Kamei, K. Hatakeyama, H. Tateishi, Y. Watanabe, T. Taniguchi, K. Gezuhara, S. Hayami, A. Funatsu, M. Sakata, Y. Kuwahara, S. Kurihara, Y. Matsumoto, *J. Phys. Chem. C* **2012**, 116, 19822.
- [29] Y. H. Ding, P. Zhang, Q. Zhuo, H. M. Ren, Z. M. Yang, Y. Jiang, *Nanotechnology* **2011**, 22, 215601.
- [30] W. S. Hummers, Jr., R. E. Offeman, *J. Am. Chem. Soc.* **1958**, 80, 1339.
- [31] J. H. Scofield, *J. Electron Spectrosc. Relat. Phenom.* **1976**, 8, 129.

- [32] R. S. Rubino, E. S. Takeuchi, *J. Power Sources* **1999**, 81, 373.
- [33] M. J. McAllister, J. Li, D. H. Adamson, H. C. Schniepp, A. A. Abdala, J. Liu, M. H. Alonso, D. L. Milius, R. Car, R. K. Prud'homme, I. A. Aksay, *Chem. Mater.* **2007**, 19, 4396.
- [34] Y. Yukselen, A. Kaya, *J. Geotech. Geoenviron Eng.* **2006**, 132, 931.
- [35] J. Díaz, G. Paolicelli, S. Ferrer, F. Comin, *Phys. Rev. B* **1996**, 54, 8064.
- [36] R. Haerle, E. Riedo, A. Pasquarello, A. Baldereschi, *Phys. Rev. B* **2001**, 65, 045101.
- [37] H. Estrade-Szwarckopf, *Carbon* **2004**, 42, 1713.
- [38] D.-Q. Yang, E. Sacher, *Surf. Sci.* **2002**, 516, 43.
- [39] R. Larciprete, S. Gardonio, L. Petaccia, S. Lizzit, *Carbon* **2009**, 47, 2579.
- [40] K. Krishnamoorthy, M. Veerapandian, K. Yun, S.-J. Kim, *Carbon* **2013**, 53, 38.
- [41] T. Szabó, O. Berkesi, P. Forgó, K. Josepovits, Y. Sanakis, D. Petridis, I. Dékány, *Chem. Mater.* **2006**, 18, 2740.
- [42] Y. Shao, J. Wang, M. Engelhard, C. Wang, Y. Lin, *J. Mater. Chem.* **2010**, 20, 743.
- [43] T. Kuila, P. Khanra, A. K. Mishra, N. H. Kim, J. H. Lee, *Polym. Test.* **2012**, 31, 282.
- [44] H. Tang, G. J. Ehlert, Y. Lin, H. A. Sodano, *Nano Lett.* **2012**, 12, 84. 115, 17009.
- [45] S. Ferro, M. D. Colle, A. D. Battisti, *Carbon* **2005**, 43, 1191.
- [46] A. C. Ferrari, J. Robertson, *Phys. Rev. B* **2000**, 61, 14095.
- [47] K. N. Kudin, B. Ozbas, H. C. Schniepp, R. K. Prud'homme, I. A. Aksay, R. Car, *Nano Lett.* **2008**, 8, 36.
- [48] T. Wassmann, A. P. Seitsonen, A. M. Saitta, M. Lazzeri, F. Mauri, *Phys. Rev. Lett.* **2008**, 101, 096402.
- [49] M. P. Seah, *Thin Solid Films* **1981**, 81, 279.
- [50] G. K. Wehner, In: A. W. Czanderna, editor. *Methods of surface analysis*. Amsterdam: Elsevier; **1975** [Chapter 1].

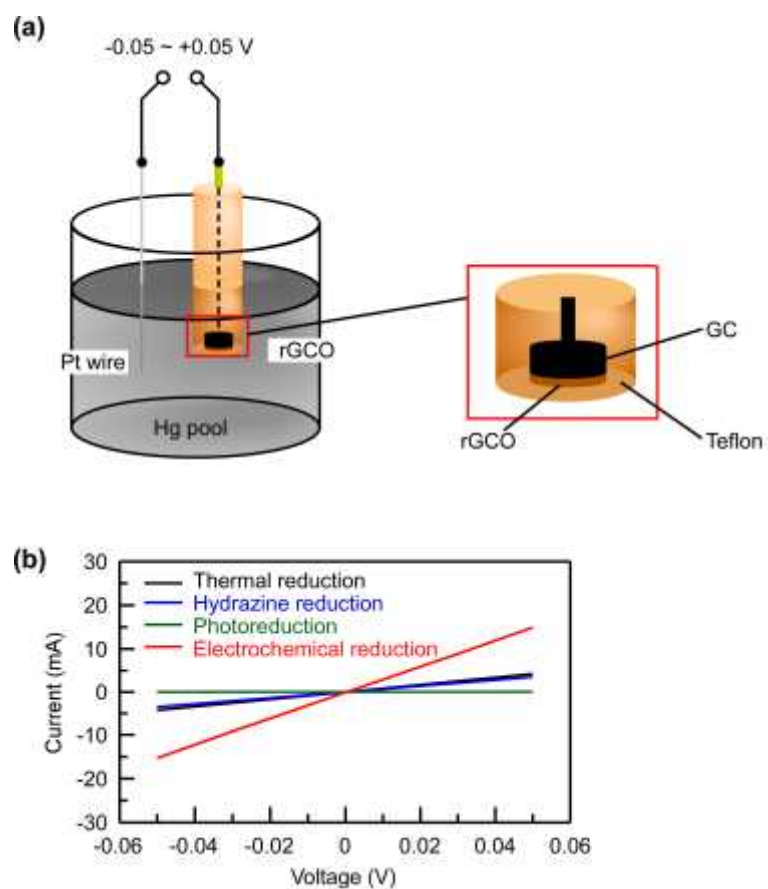


Figure 3-1. (a) Schematic illustration of the resistance measurement system for the GtO electrodes.

(b) I-V curves of the GtO electrodes prepared by thermal, hydrazine, photo-, and electrochemical reduction.

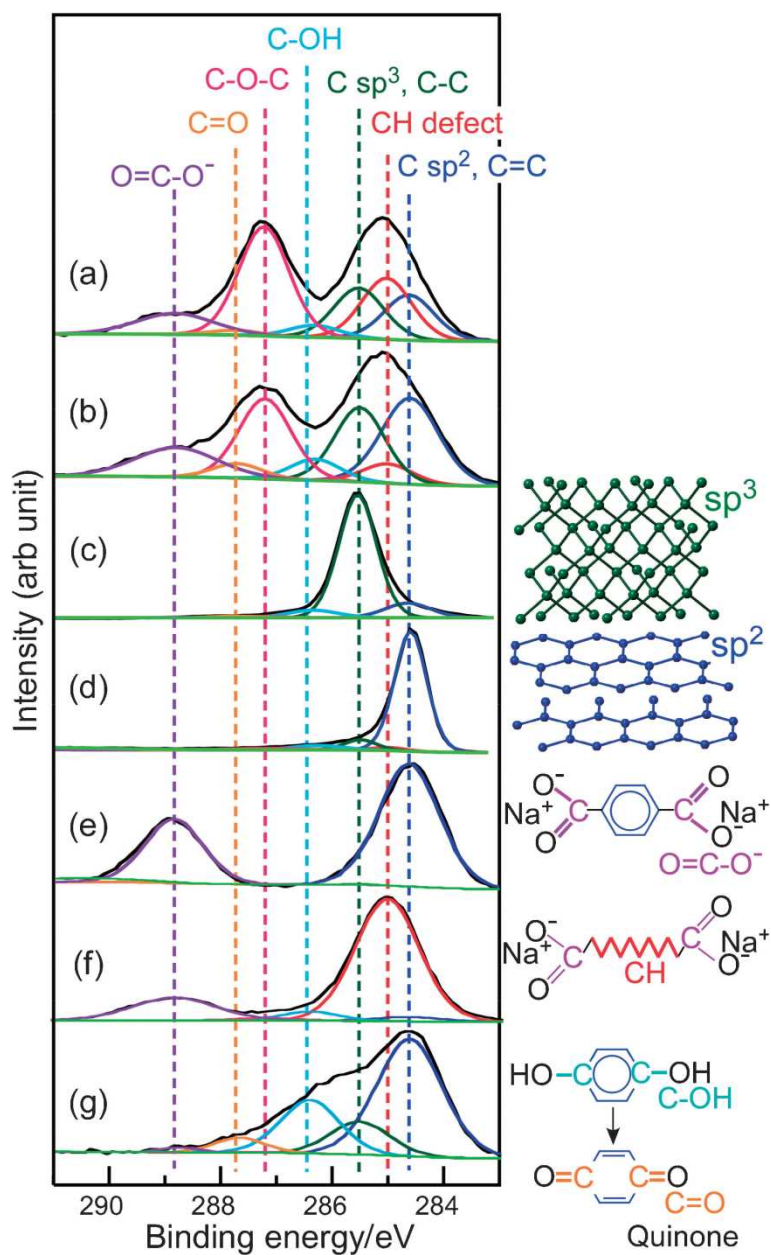


Figure 3-2. C1s XPS spectra of (a) GO, (b) GtO, (c) diamond(100), (d) HOPG, (e) sodium terephthalate, (f) sodium dodecanedioate, and (g) hydroquinone. The structures of the reference compounds are shown on the right.

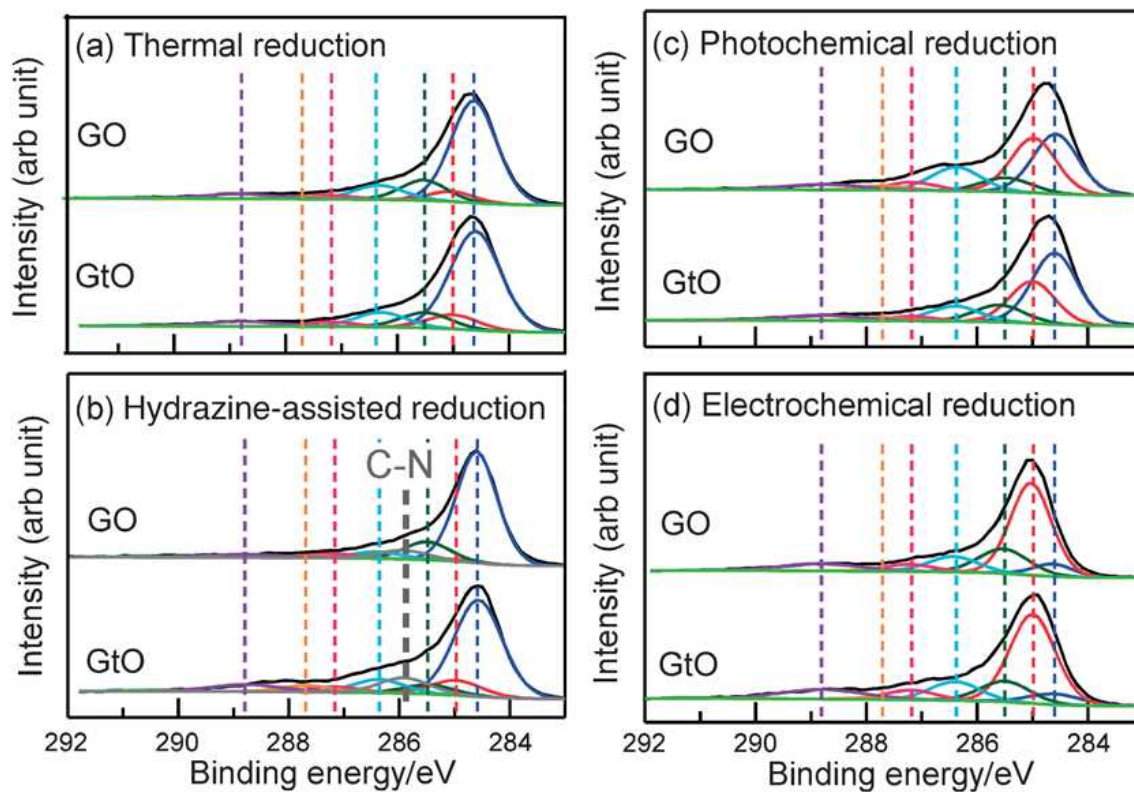


Figure 3-3. C1s XPS spectra of rGO and rGtO prepared by various reduction methods. **(a)** Thermal reduction at 300°C in Ar, **(b)** hydrazine-assisted reduction, **(c)** photochemical reduction in H₂ for 1 h, and **(d)** electrochemical reduction at -1.1V for 30min.

Table 3-1. Functional group content of GOs, GtOs, and reference samples

	atm %											O/(C+O)
	C=C	CH	C-C	C-OH	C-O-C	C=O	O=C-O	C-N				
GO	14.6	18.9	16.6	3.9	34.0	1.8	10.1	-				32.1
	27.5	4.7	21.7	6.1	22.3	4.5	13.3	-				28.9
GtO												
Diamond(100)	11.3	0	80.1	6.1	0.6	1.6	0.2	-				5.8
HOPG	82.6	1.8	9.9	3.5	0.8	1.4	0	-				0.3
Untreated	Sodium terephthalate	65.5	0	0.3	0	0	0	34.2	-			32.7
	Sodium dodecanedioate	2.7	73.2	0	4.9	1.4	0	17.8	-			37.4
Hydroquinone	62.4	0	5.9	24.7	0.2	6.1	0.6	-				28.8
Thermal reduction	GO	63.0	4.7	14.3	9.4	1.6	2.1	4.9	-			11.5
	GtO	63.5	7.0	11.9	9.1	2.2	1.3	4.9	-			11.5
Hydrazine reduction	GO	66.4	1.4	11.9	5.0	3.3	1.7	3.9	6.5			9.4
	GtO	55.0	8.8	5.6	8.0	3.3	3.9	6.1	9.2			15.3
Photochemical reduction	GO	33.2	40.5	8.7	14.5	5.1	2.6	5.5	-			15.1
	GtO	42.7	25.1	11.2	10.1	3.0	2.3	5.7	-			14.6
Electrochemical reduction	GO	6.9	51.5	16.8	10.7	4.9	1.1	8.1	-			18.8
	GtO	7.2	50.9	12.8	11.7	5.9	1.8	9.7	-			20.8

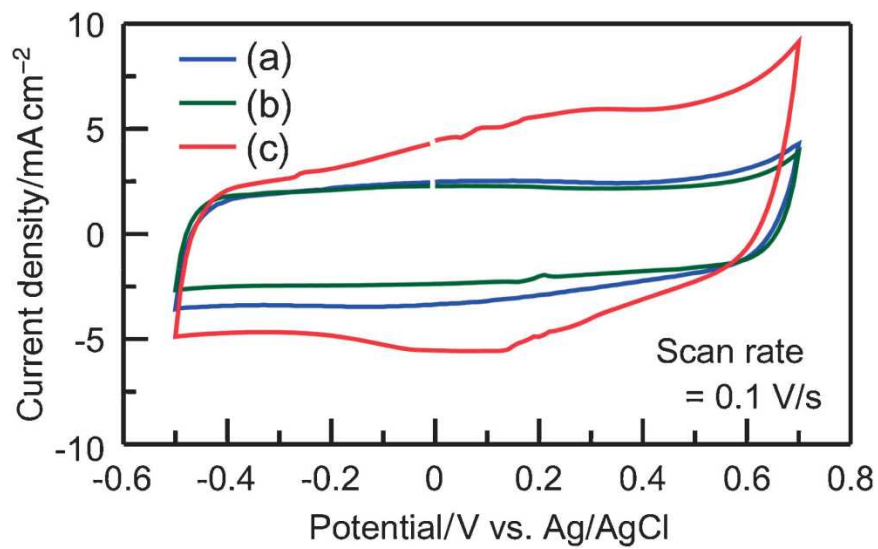


Figure 3-4. Cyclic voltammograms (CVs) of rGtO prepared by reducing GtO. **(a)** Thermal reduction, **(b)** hydrazine-assisted reduction, and **(c)** electrochemical reduction

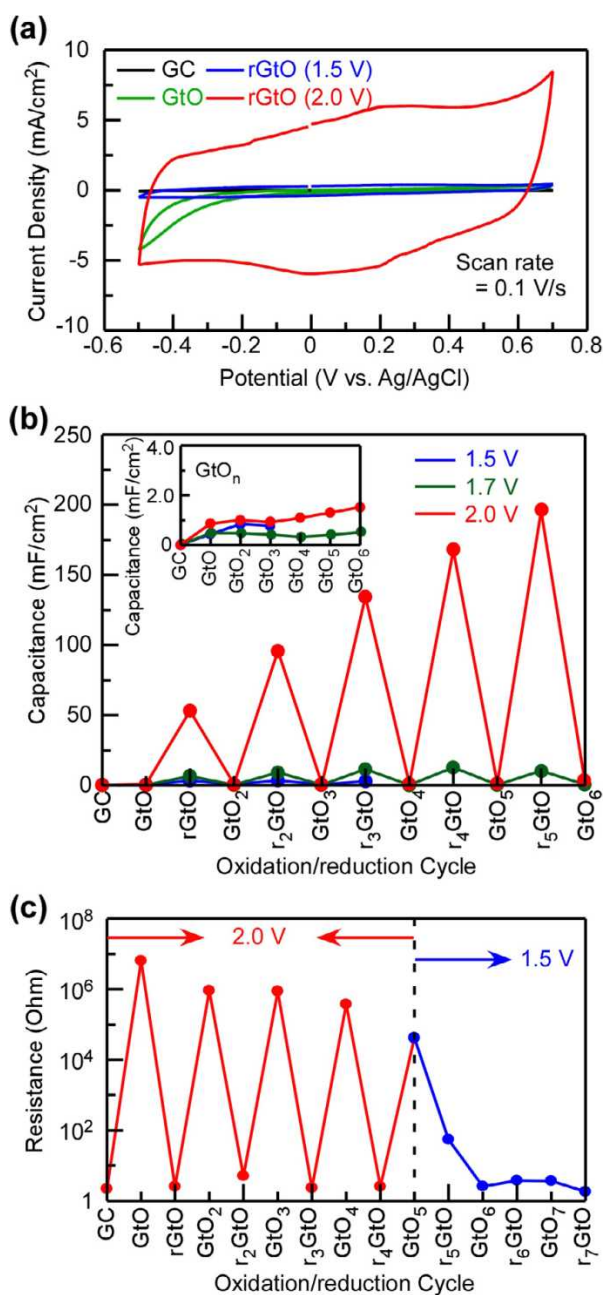


Figure 3-5. (a) CVs of GC, GtO, and rGtO. Oxidation was conducted at +1.5 or +2.0 V, and reduction was conducted at -1.1 V. **(b)** Dependences of electrochemical capacitances of GC, GtO_n, and r_nGtO on the oxidation/reduction cycle. Oxidation was conducted at +1.5, +1.7, or +2.0 V, and reduction was conducted at -1.1 V. The inset shows the electrochemical capacitances of GtO_n. **(c)** Dependences of resistances of GC, GtO_n and r_nGtO on oxidation/reduction cycle, where oxidation were made at 2.0 V and 1.5 V.

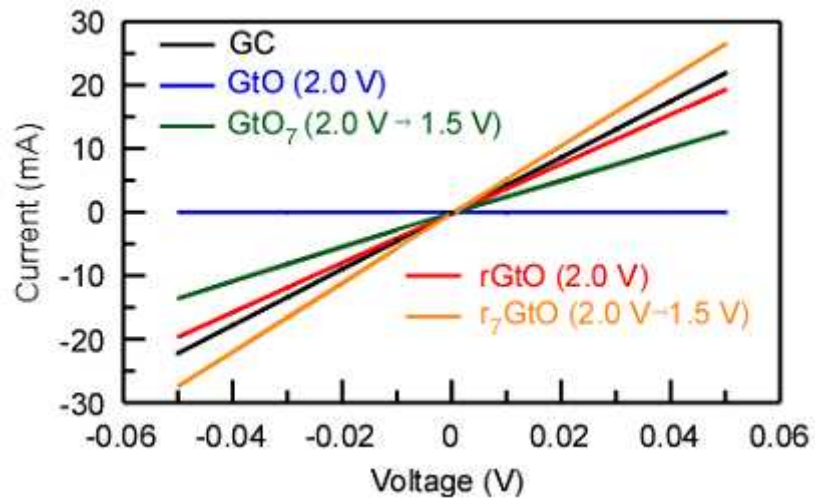


Figure 3-6. I-V curves of the GC, GtO_n, and r_nGtO films (The values in the parenthesis are the potentials during the oxidation process).

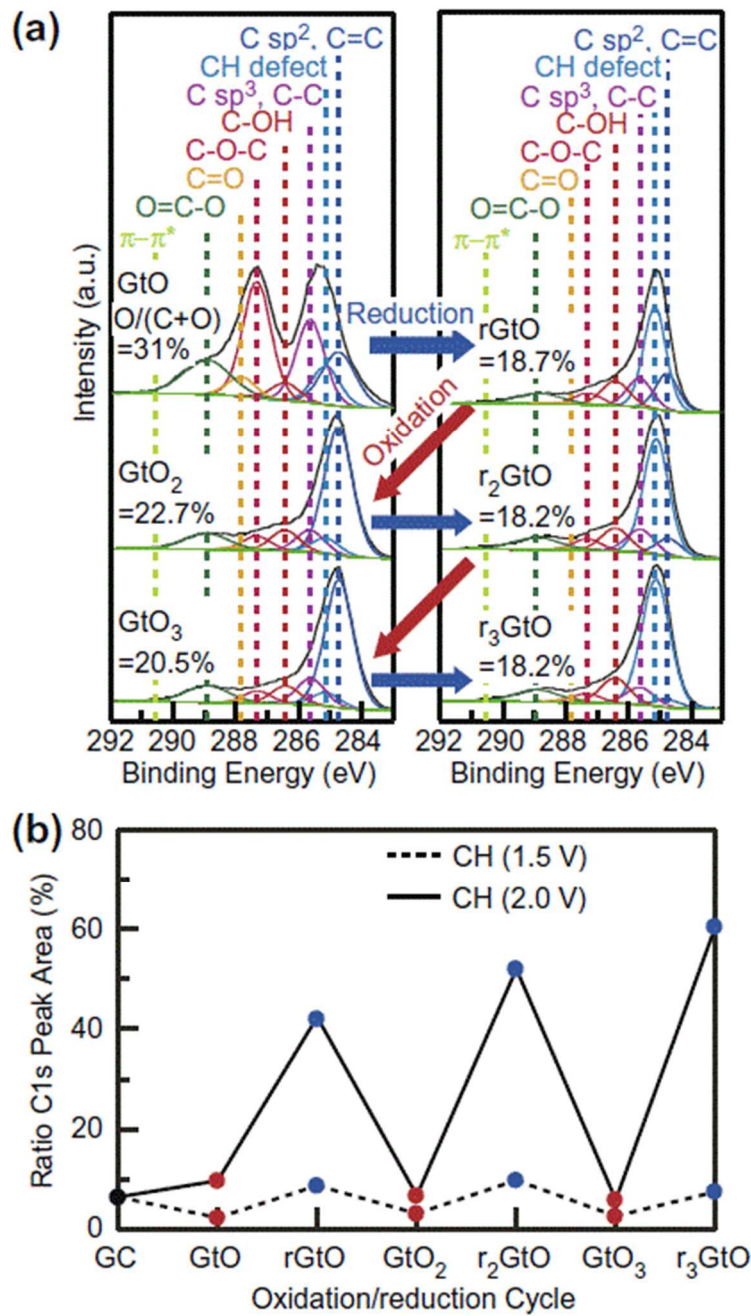


Figure 3-7. (a) C1s XPS profiles of the GtOn and rGtO electrode samples where oxidation and reduction were conducted at +2.0 V and -1.1 V, respectively. **(b)** Dependences of the content of the CH defect on the oxidation/reduction cycle (The values in the parenthesis are the potentials during the oxidation process).

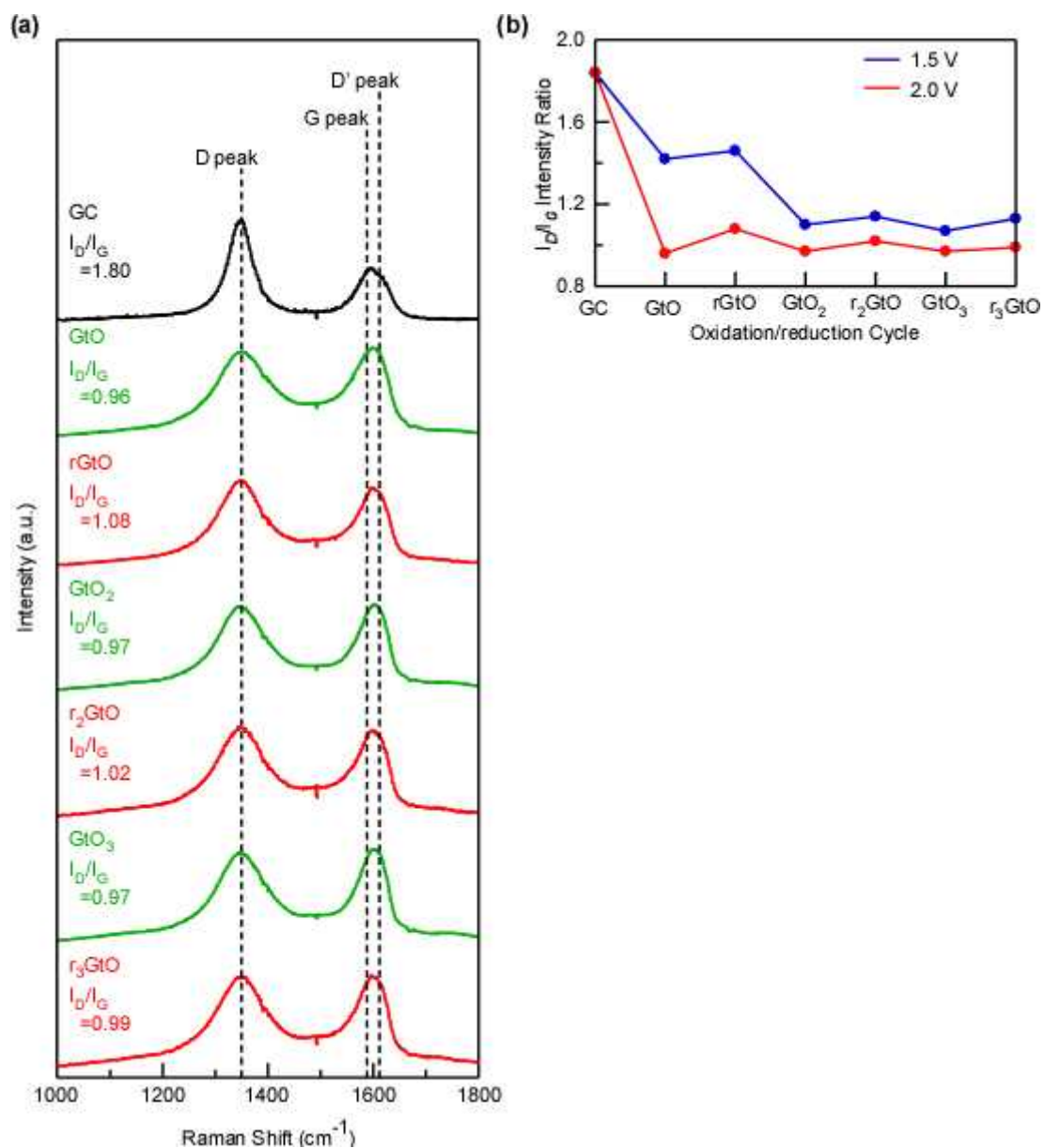


Figure 3-8. (a) Raman spectra of GC, GtO_n and r_nGtO, where oxidation and reduction were conducted at +2.0 V and -1.1 V, respectively. (b) Dependences of the I_D/I_G intensity ratio on the oxidation/reduction cycle (The values in the parenthesis are the potentials during the oxidation process).

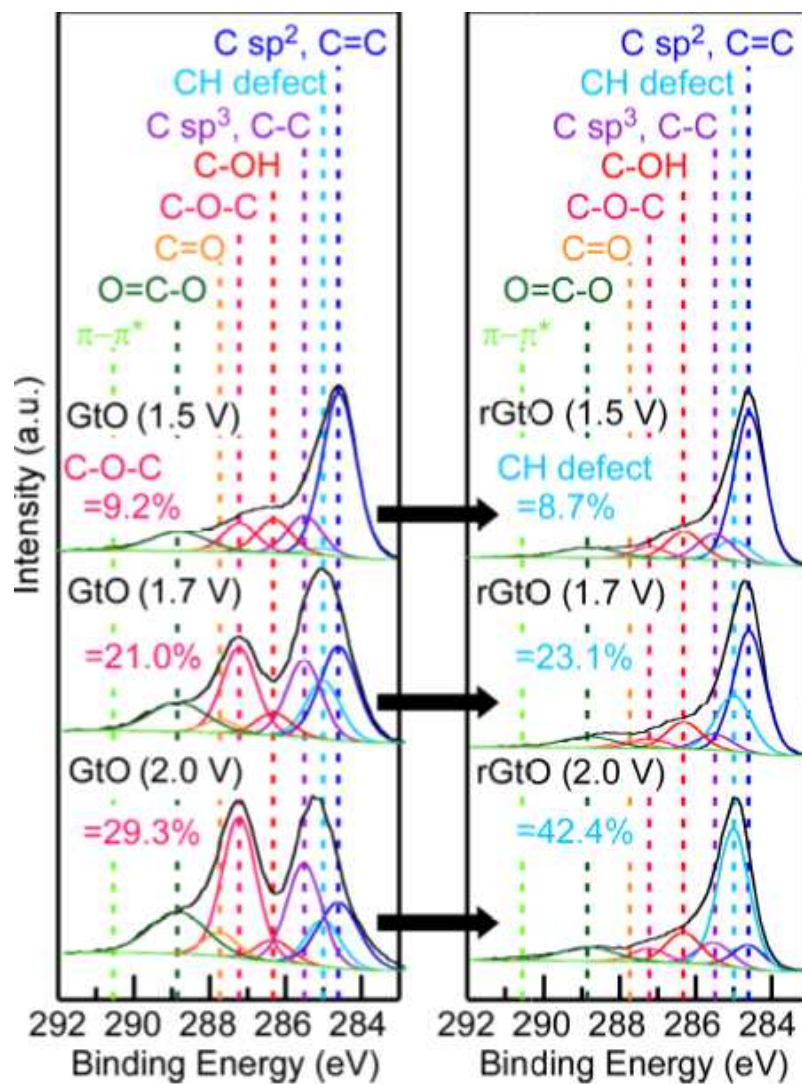


Figure 3-9. (a) C1s XPS profiles of the GtO (oxidized at +1.5 V, +1.7 V, or +2.0 V) and the rGtO (reduced at -1.1 V).

Table 3-2. Functional group contents (atm%) of GC, GtO_n, and r_nGtO.

Sample	atm%								
	Csp ²	CH	Csp ³	C-OH	C-O-C	C=O	O=C-O	π - π^*	O/ (C+O)
	C=C	defect	C-C						
GC	61.6	6.4	14.8	7.1	4.4	0.0	3.7	2.0	7.2
GtO (1.5 V oxidation)	52.7	2.3	12.4	10.8	9.2	1.6	10.3	0.6	20.6
rGtO (1.5 V oxidation)	56.4	8.7	10.8	11.4	4.7	0.6	7.0	0.4	15.1
GtO ₂ (1.5 V oxidation)	57.9	3.1	11.0	9.6	4.9	1.4	11.4	0.8	21.4
r ₂ GtO (1.5 V oxidation)	55.7	9.8	8.5	11.2	3.4	2.4	8.6	0.3	19.0
GtO ₃ (1.5 V oxidation)	55.4	2.6	11.1	9.9	7.0	2.2	11.0	0.8	21.6
r ₃ GtO (1.5 V oxidation)	57.7	7.5	9.1	11.0	3.3	2.5	8.5	0.3	19.0
GtO ₄ (1.5 V oxidation)	58.9	3.1	10.4	8.8	4.9	1.8	11.2	0.9	21.1
r ₄ GtO (1.5 V oxidation)	56.0	6.4	9.9	10.8	3.6	2.8	10.1	0.4	18.9
GtO (1.7 V oxidation)	25.1	14.3	19.0	5.5	21.0	3.2	11.6	0.3	26.1
rGtO (1.7 V oxidation)	45.4	23.1	6.4	11.0	4.0	2.8	7.0	0.4	17.9
GtO ₂ (1.7 V oxidation)	50.1	8.5	10.8	9.8	7.2	1.7	11.5	0.5	22.0
r ₂ GtO (1.7 V oxidation)	41.5	27.9	4.0	12.4	4.1	2.7	7.2	0.2	19.0
GtO ₃ (1.7 V oxidation)	55.6	7.0	10.7	11.2	4.0	2.0	8.8	0.8	19.2
r ₃ GtO (1.7 V oxidation)	39.6	24.9	4.8	15.4	5.3	2.7	7.2	0.2	18.9
GtO (2.0 V oxidation)	16.2	9.7	21.0	4.5	29.3	4.9	14.4	0.1	31.0
rGtO (2.0 V oxidation)	15.5	42.4	13.3	12.4	5.8	1.2	8.9	0.3	18.7
GtO ₂ (2.0 V oxidation)	55.9	6.7	9.5	9.1	6.2	1.5	10.9	0.3	22.7
r ₂ GtO (2.0 V oxidation)	8.1	52.0	11.7	11.4	5.7	1.3	9.7	0.2	18.2
GtO ₃ (2.0 V oxidation)	56.2	5.9	11.6	7.9	5.4	1.1	11.3	0.7	20.5
r ₃ GtO (2.0 V oxidation)	3.7	60.4	8.2	12.0	4.3	1.9	9.1	0.4	18.2

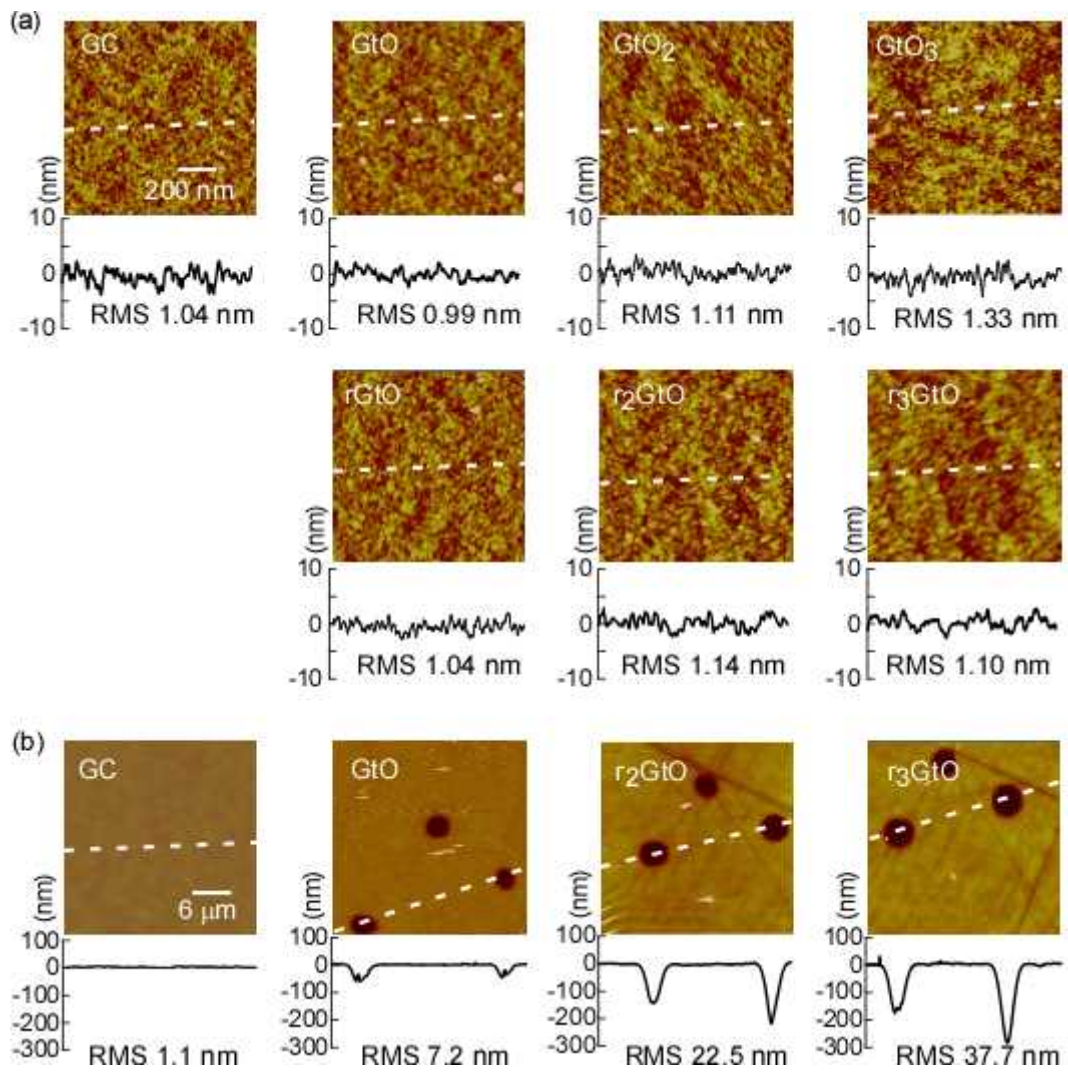


Figure 3-10. AFM images of the GC, GtO_n, and r_nGtO surfaces and their depth profiles. Scan size

(a) 1 × 1 μm² and **(b)** 30 × 30 μm².

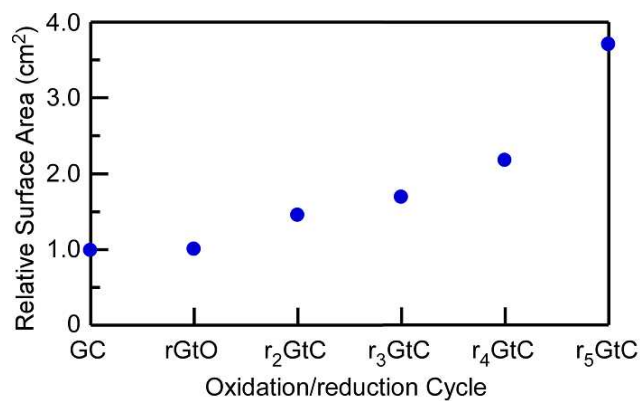


Figure 3-11. Dependence of relative SA of the r_n GtO on the oxidation/reduction cycle.

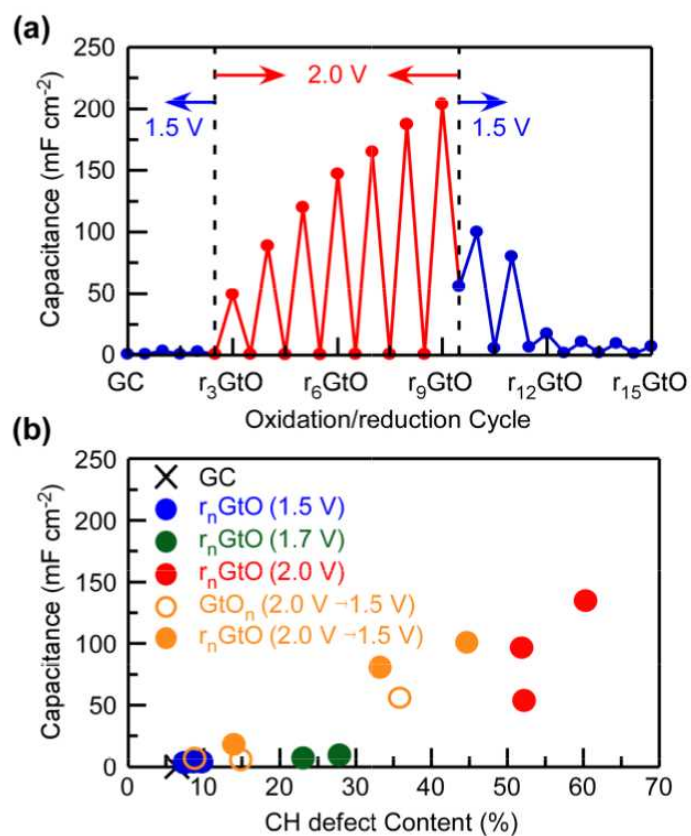


Figure 3-12. (a) Electrochemical capacitances of GC, GtO_n, and r_nGtO with respect to different oxidation potentials (+1.5 V and +2.0 V). (b) Electrochemical capacitance as a function of the content of the CH defect.

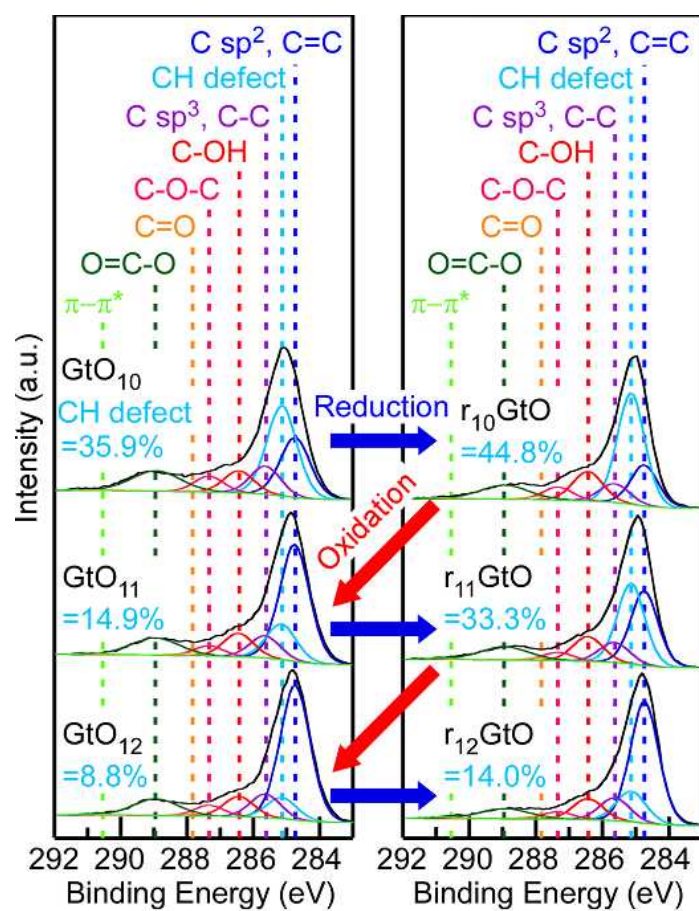


Figure 3-13. C1s XPS profiles of the GtO_n and r_nGtO prepared at +1.5 V oxidation process after +2.0 V oxidation process. *n* in the GtO_n and r_nGtO correspond to that in **Figure 3-12**.

CHAPTER 4

A Self-Assembly Route to an Iron Phthalocyanine/Reduced Graphene Oxide Hybrid Electrocatalyst Affording an Ultrafast Oxygen Reduction Reaction

Overview

Graphene oxide (GO) is an attractive freestanding support that can be decorated with ultrathin organic layers for facile and low-cost fabrication of novel devices with controllable functional properties and microstructures. In this chapter, it is reported that a hybrid material consisting of an ultrathin iron phthalocyanine (FePc) layer self-assembled on reduced graphene oxide (rGO) exhibits excellent catalytic activity that is superior to that of commercial Pt/C for an oxygen reduction reaction (ORR). During solution processing, the FePc layer is first self-organized onto GO sheets and then reduced electrochemically to form an FePc/rGO hybrid electrocatalyst. Kinetics studies reveal that the hybrid architecture affords an ultrafast ORR rate caused by a strongly dominant four-electron process, and the durability of the catalyst shows significant improvement by forming the hybrid structure. Spectroscopic studies suggest that these advantages are afforded by synergistic effects between FePc and rGO, which are enriched by the hybrid structure and the appropriate reduction step.

4.1 Introduction

Engineering organic ultrathin layers at a nanoscale level enables the enhancement of functional properties owing to electrical, magnetic, optical coupling with the substrate surface, which is a key technology for developing next-generation optica ^[1], catalysis ^[2], photovoltaic conversion ^[3], electronic ^[4], or spintronics devices ^[5]. Surface-supported metallophthalocyanines

(MPcs) have attracted a great deal of attention for a wide variety of applications owing to their versatile functional properties, which depend on the central metal ion [2, 5-7]. In particular, an iron phthalocyanine (FePc)-based catalyst exhibits high activity for oxygen reduction reactions (ORRs) at an alkaline condition [8-10], and as a cathodic oxygen reduction catalyst in alkaline fuel cells, it is preferred to commercial Pt-based catalysts, which have drawbacks such as high cost and low availability in addition to their insufficient catalytic activity and durability [11].

The formation of an FePc ultrathin layer on a single-crystalline substrate has been investigated intensively in order to understand intermolecular interactions as well as molecular-substrate interactions [2, 6, 7, 12]. For instance, Mao *et al.* [6] discovered that the formation of FePc Kagome lattices on Ru (0001) surfaces, which might be excellent model systems for studying spin frustration. Recently, Sedona *et al.* [2] successfully identified the local O₂ chemisorption site in a composite consisting of an FePc monolayer on a Ag(110) surface. Such ultrathin FePc layers essentially provide ideal species for evaluating and driving catalytic reactions owing to facile electron transfer from the conductive support to the catalyst. However, the tiny surface area of the flat and bulky substrates conventionally employed provides limited opportunities toward practical applications in areas such as energy storage/conversion and as catalysts for the sustainable production of fuels and chemicals.

Knowledge obtained from these fundamental studies can be efficiently linked to the development of devices applicable to these areas if exfoliated nanosheets with a thickness of approximately 1 nm and a lateral size ranging from submicrometer to several tens of micrometers are rationally employed as free-standing supports [13, 14]. In principle, molecular layers can be formed on nanosheets in a dispersion by liquid-phase self-assembly routes. Subsequently, a simple colloidal process allows the integration of these modified nanosheets, leading to microstructures with a controlled surface area to generate high output power using a small amount of catalyst. GO has

distinct features among the various types of exfoliated nanosheets ^[15, 16], which includes metal hydroxides, oxides, and dichalcogenides. First, GO is hydrophilic owing to an abundance of oxygen functional groups, while removal of these groups by a reduction process makes it hydrophobic. Reduction also changes insulating GO into conductive rGO owing to the increased fraction of graphene-like sp² domains ^[16, 17]. In addition to the inexpensiveness and high availability, such broad chemical and physical tunability holds significant promise for the development of novel two-dimensional hybrids based on GO nanosheets with functional molecular layers ^[18, 19].

In this framework, GO and rGO have been hybridized with various phthalocyanine and porphyrin molecules so far ^[20–23]; however, it has been still challenging to fabricate rGO-based hybrid materials with well-tailored functional properties. This is because hybrid structures as well as the reduction process must be appropriately controlled to maximize synergy effects between rGO and decorated molecules. For example, FePc plates deposited on rGO showed poorer ORR properties than Pt/C ^[24]. Hence, the detailed study on controlling both self-assembly and reduction-steps is highly required to archive the fabrication of rGO–FePc hybrid catalysis with excellent ORR properties, which also would clarify critical and general roles of these steps to assist in the further development of organic layer-rGO hybrids usable in many technological fields.

In this chapter, we report a simple, low-temperature, and effective self-assembly route to an FePc–rGO hybrid electrocatalyst. We demonstrate that FePc nanodomains with a single layer or a few layers of thickness self-organized onto rGO afford ORR activity under alkaline conditions superior to that of commercial Pt/carbon black (Pt/C) catalysts as well as rGO or nitrogen-doped rGO (N-rGO) hybridized with metal nanoparticles ^[25, 26] transition oxide nanoparticles ^[27–29], or FePc nanoplates ^[24]. Because of these outstanding features, the FePc/rGO self-assembled composite is applicable as an electrocatalyst for the cathode in alkaline fuel cells, which have recently experienced renewed interest as a solution to electrolyte carbonation ^[30].

4.2 Experimental

4.2-1 Preparation of the FePc/GO hybrid by self-assembly

GO was prepared by Hummers' method using 98% graphite powder ($\approx 2\%$ oxygen; Wako Ltd.) as the initial material. A GO dispersion (0.5 g L^{-1}) was obtained after centrifugation to remove multilayer GO. A solution of FePc (0.5 g L^{-1}) was prepared by adding FePc powder ($\approx 90\%$; Aldrich) to ethanol (special grade reagent, 99.5%; Wako Ltd.) and subjecting the resulting mixture to ultrasonic treatment for 30 min. The FePc ethanol solution (20 mL) was mixed with the GO dispersion (1, 2, 4, 10, or 20 mL) overnight to yield blue precipitates of the FePc/GO hybrid along with a colorless supernatant solution.

4.2-2 Preparation of the FePc/rGO hybrid

For FePc/rGO hybrid electrode fabrication, the aforementioned FePc/GO hybrid dispersion was deposited on glassy carbon (GC) electrode (BAS Ltd), and then was dried. Accordingly, $75 \mu\text{g}$ of sample was loaded on the glassy carbon working electrode (3.0 mm in diameter). The drying process was performed under vacuum at RT. Then, the FePc/GO/GC electrode, as a working electrode, was reduced for 5 min at -1.1 V (vs. Ag/AgCl) in $0.1 \text{ M Na}_2\text{SO}_4$ with Pt wire as a counter electrode in an electrochemical reduction process. A potentiostat with a function generator (Ivium Compactstat) was used for the electrochemical reduction process. Hydrothermal, chemical, and photo-reduction methods were also employed to prepare FePc/rGO hybrid catalysts. In the hydrothermal reduction process, 20 mL of the FePc/GO hybrid dispersion was placed in a polytetrafluoroethylene (PTFE) vessel (inner volume 40 cm^3). The vessel was sealed, placed in a stainless steel autoclave, and maintained at $150 \text{ }^\circ\text{C}$ for 3 h under autogenous pressure. In the chemical reduction process, 4 mL of hydrazine monohydrate (special grade reagent, 98%; Wako Ltd.) or 0.5 g of sodium borohydride powder (extra pure reagent, 95%; Wako Ltd.) was added to 20 mL of an FePc/GO hybrid dispersion, and the resulting mixtures were heated at $60 \text{ }^\circ\text{C}$ for 6 h, and 5

min, respectively. In these cases, 75 μg of sample was deposited on GC electrodes. In the photoreduction process, 75 μg of an FePc/GO hybrid was deposited on an GC electrode, and the sample was irradiated (Hg light, 500 W) for 2 h. After these reduction processes, the color of the products changed to be black, indicating the reduction of GO. Finally, these catalysts on a GC electrode were dried at 70 $^{\circ}\text{C}$ for 30 min in air.

4.2-3 Preparation of rGO and FePc electrode

The aforementioned GO dispersion or FePc solution was deposited on a GC electrode and then electrochemically reduced at -1.1 V (vs. Ag/AgCl) for 5 min. In both cases, 75 μg of sample was loaded on the GC working electrodes.

4.2-4 Preparation of FePc/rGO bilayer

First, 25 μg of GO was deposited on a GC electrode, and then 50 μg of FePc was deposited on the GO layer. 75 μg of the prepared sample was loaded on the GC working electrode, and finally the FePc/GO bilayer was electrochemically reduced at -1.1 V (vs. Ag/AgCl) for 5 min.

4.2-5 Preparation of the standard Pt/C electrode

The Pt/C catalyst (30 mg, 20wt% Pt on Vulcan XC-72; ElectroChem, Inc.) was suspended in a solution of 10wt% Nafion (0.12 mL) in ethanol (10 mL), and a droplet of the resulting suspension involving 75 μg of catalyst was placed on a GC electrode surface and then vacuum-dried. Note that we carefully fabricated the reference electrode such that the ORR activity of the Pt/C catalyst employed here was closely comparable with that reported elsewhere measured under the same conditions [27].

4.2-6 Characterization

X-ray photoelectron spectroscopy (XPS; Thermo Fisher Scientific, SigmaProbe) was used to analyze the surface of all the GO samples. A monochromatized X-ray source (Al K α , $h\nu = 1486.68$ eV) was used for XPS. Raman spectroscopy (Jasco, NRS-3100) was performed using a 532 nm excitation source at room temperature. The morphology of the GO and FePc/GO samples was observed by atomic force microscopy (AFM; Digital Instruments, Nanoscope V, tapping mode). Scanning electron microscopy was performed on an FEI XL30 Sirion scanning electron microscope. Transmission electron microscopy was performed on an FEI Tecnai G2 F20 transmission electron microscope.

4.2-7 Electrochemical analysis

Cyclic voltammetry (CV) measurements were carried out using three-electrode electrochemical cells. Samples were tested as electrodes for the ORR in 0.1 M or 1 M KOH saturated with O₂. Pt wire and Ag/AgCl electrodes were used as the counter and reference electrodes, respectively. The disk electrode was scanned cathodically at a rate of 5 mV s⁻¹ and the ring potential was constant at 1.5 V vs. RHE. The percentage HO₂⁻ and the electron transfer number (n) were determined, according to the previously reported methods [37].

Rotating disk electrode (RDE) and rotating ring-disk electrode (RRDE) measurements in 0.1 M or 1 M KOH saturated with O₂ were conducted with a RDE/RRDE system (Pine Instruments) with a function generator. The working electrodes for RDE and RRDE measurements were prepared by loading 180 μ g of samples or reference Pt/C on a GC electrode, 5.0 mm and 5.05 mm in diameter, respectively

4.3 Results and Discussion

4.3-1 Self-assembly and electrochemical reduction of FePc on GO

GO nanosheets are negatively charged in aqueous dispersions because of their oxygen functional groups [15]. Thus, positively charged molecules can be assembled onto the surfaces of GO nanosheets. However, although FePc is a neutral molecule, it can still strongly interact with oxygen and oxygen functional groups to form complexes through electrostatic interactions. Such interactions in addition to π - π stacking interactions provide a driving force for self-assembly of FePc onto GO. We employed a simple approach in which an aqueous dispersion of GO and an ethanol solution of FePc were mixed at room temperature and ambient pressure overnight to yield blue-colored precipitates of the FePc/GO hybrid (Figure 4-1(a)). High-angle annular dark-field scanning transmission electron microscopy (HAADF-STEM) images revealed that FePc nanodomains (bright parts) were highly loaded over the GO surface in the hybrid sample (Figure 4-1(a)); heavy atoms appear bright in the HAADF-STEM image. Note that FePc domain should be deposited on the both sides, considering that GO exhibit oxygen function group on the front and back of the sheet structure. The size of these domains is in the range of 2–10 nm (Figure 4-2,). The height profile obtained by atomic force microscopy (AFM) (Figure 4-1(b)) indicates that the thickness of most domains is in the range of 0.4–1.5 nm. The thickness indicates that self-assembled FePc nanodomains were mainly composed of single molecular layers or a few layers, considering the observed thickness of the FePc monolayer on a mica substrate (0.35 nm). The thickness of the GO sheets is approximately 1.5 nm, which demonstrates that the FePc nanodomains were self-organized on single-layer GO nanosheets. Nanoscale energy dispersive X-ray spectroscopy (EDX) elemental analysis with a bright-field TEM (Figure 4-1(c), (d)) revealed that FePc nanodomains generally showed more intense oxygen peaks than bare GO components in which oxygen functional groups rapidly decomposed during focused electron beam irradiation. Stable detection of both Fe and oxygen indicates that oxygen functional groups anchored FePc molecules on sp^3 regions.

The FePc/GO hybrid was reduced electrochemically to yield the FePc/rGO electrocatalyst in the final step. We employed the electrochemical method, as it is fast, clean, and nondestructive [25, 26], which should be suitable to prepare organic-rGO composites. Monitoring the cathodic current produced by the reduction of GO indicated that the reduction was complete in 5 min (Figure 4-3). C1s X-ray photoelectron spectroscopy (XPS) data (Figure 4-4(a)) demonstrated a decrease in peak intensity of oxygen function groups and an increase in C-C and C=C peak intensity after electrochemical reduction [31]. Peak-area analysis revealed that C/O atomic ratio increased from 2.6 to 7.0 by the reduction. We confirmed that the reduction step insignificantly changed the morphology of the hybrid structure (Figure 4-4(b), (c)). These results suggest that the GO nanosheets with ultrathin FePc layers were successfully reduced.

4.3-2 ORR properties of FePc/rGO hybrid

We employed cyclic voltammetry (CV measurements) in order to investigate the ORR catalytic activity of samples. CV measurements were performed in an O₂-saturated 1 M KOH aqueous solution. Commercial 20wt% platinum on Vulcan carbon black (Pt/C from ElectroChem) was used as a reference. The CV polarization curve (Figure 4-5(a)) demonstrated that the FePc/rGO hybrid offered a higher peak reduction potential than commercial Pt/C in which the reduction peak was observed at -0.08 V and -0.14 V (vs. Ag/AgCl) for FePc/rGO hybrid and Pt/C, respectively. Furthermore, rGO and FePc samples as well as a bilayer sample prepared by simply depositing FePc on an electrode-bound layer of GO showed much negative reduction potential than the hybrid. This demonstrated that rGO nanosheets with ultrathin FePc nanodomains have an ideal hybrid structure for enhancing synergistic effects between rGO and FePc to bolster ORR activity. The highest reduction peak voltage was obtained using hybrids with an initial FePc/GO weight ratio of 5/1 (Figure 3 b). The small ratio may have led to the low coverage of FePc on rGO. As a result, the

hybrids exhibit an insufficient number of active sites for the ORR. On the other hand, higher ratios led to the growth of significantly thicker FePc plates on rGO producing lower catalytic activity (Figure 4-5(c)). We hypothesize that efficiency of electron transfer from rGO to FePc decrease with an increase of FePc layer thickness on rGO. Thus, the formation of ultrathin layers with a high coverage enabled to produce the excellent ORR properties for the hybrid.

We assessed the ORR activity of the FePc/rGO hybrid in detail using RDE and RRDE. Figure 4-6(a), (b) shows the RDE linear sweeping voltammograms in O₂-saturated 1 M and 0.1 M KOH solutions at the rotation rate of 1600 rpm, respectively. The data show that the FePc/rGO hybrid exhibit a higher reduction current in overall Tafel region, while the limiting currents were comparable between the two samples. Under these conditions, the hybrid demonstrates better ORR activity than boron/nitrogen-codoped rGO [32] as well as N-rGO decorated with transition metal species [24, 26–28] (Figure 4-7). In addition to the high ORR activity, the self-assembly route offers further advantages toward large-scale production, considering that relevant works required toxic chemicals as well as high pressure or high temperature processes for doping nitrogen into GO.

Rotating ring–disk electrode (RRDE) measurements were performed to understand the origin of the ultrafast ORR using the hybrid. The percentage of peroxide species with respect to the total oxygen reduction products and the electron reduction number (n) were calculated from RRDE curves recorded at 1600 rpm in 0.1 M KOH for the hybrid, bilayer, and Pt/C samples (Figure 4-8(a) and Figure 4-9). The yield of peroxide species was less than 3% over the measured potential range for the hybrid catalyst and was generally lower than $\approx 15\%$ and $\approx 10\%$ for the bilayer catalyst and Pt/C, respectively. The average electron transfer number exceeded ≈ 3.95 over the range from 0.2–0.9 V for the hybrid, a value higher than those of the other samples. Furthermore, the hybrid displays a very small Tafel slope in the plot of the kinetic current (33 mV/decade) (Figure 4-8(b)). The value is less than half that of Pt/C (88 mV/decade). Thus, a strongly dominant four-electron reduction

pathway resulted in extremely facile electron transfer from rGO to active FePc sites located near the rGO surface.

We further investigated the impact of the formation of the hybrid architecture on catalyst durability. Figure 4-10 displays normalized ORR current over 25000 s of continuous operation for the hybrid, bilayer, and Pt/C samples. The results show that the FePc/rGO hybrid gave a decay curve with a $\approx 10\%$ decrease during the operation, which is comparable to that for Pt/C prepared in this study. In contrast, the ORR current using the bilayer sample decayed drastically ($\sim 80\%$). According to the literature, a catalyst composed of thick FePc nanoplates on N-rGO presented intermediate durability between the hybrid and bilayer samples ($\approx 30\%$ decrease over 6000 s)^[24] under the quite similar operation condition, thus indicating that the thinner FePc layer generally results in higher durability. As desorption of the catalyst from the GC electrode was not observed for all samples during the operation, it is concluded that decay is induced by the intermediate products^[8]. Considering this, the strongly preferable four-electron process for the hybrid could prohibit the production of H₂O₂ (produced by a two-electron process), thus maintaining active sites for the ORR.

4.3-3 Raman and XPS studies of self-assembled FePc on GO and rGO obtained by electrochemical reduction and other reduction methods

XPS and Raman spectroscopy were investigated for a better understanding of the interplay between FePc and GO. Figure 4-11(a) shows the Fe 2p_{3/2} spectra of the FePc/GO hybrid before and after electrochemical reduction. The FePc/GO hybrid exhibits a main XPS peak at 712 eV, while electrochemical reduction lowered the binding energy to ca. 709 eV. The peak position for the FePc/rGO hybrid matches well to that of FePc thin films deposited by a vacuum process, indicating that the FePc on rGO is in the divalent state. The higher binding energy for FePc/GO suggests that the initially divalent Fe ions were oxidized to a trivalent state during self-assembly as a result of Fe 3d and O 2p hybridization via oxygen present in solution and/or on GO. Subsequently, the

electrochemical reduction process reduced Fe^{3+} to Fe^{2+} , accompanied by the reduction of GO. The Raman spectra of the hybrid before and after the reduction (Figure 4-11(b)) display sharp peaks corresponding to the Raman active modes of phthalocyanine with a broad background peak for the D band ($\approx 1350 \text{ cm}^{-1}$) and G band ($\approx 1600 \text{ cm}^{-1}$) of rGO without any peaks from iron-based impurity phases. The B_{1g} band at 1536 cm^{-1} , attributable to the displacement of C–N–C bridge bonds, is highly sensitive to the mass, size, and valency of the central metal cation. In the present case, the peak for the FePc/GO hybrid was shifted toward a higher wavenumber (20 cm^{-1}) by the reduction, which supported the theory that the divalent Fe cations in the FePc/rGO hybrid were located in the cavity of a phthalocyanine macrocycle, functioning as active sites for the ORR. It is notable that the positions of the Fe $2p_{3/2}$ XPS spectra and B_{1g} Raman bands of the bilayer sample were changed very slightly after the electrochemical reduction, indicating that the reduction step insignificantly altered the dominant trivalent state. These results imply that FePc molecules attached onto GO nanosheets were preferably reduced to acquire a rather stable divalent state enabling strong electrochemical coupling between FePc nanodomains and rGO in the hybrid, which led to the ultrafast electron transfer as well as the improved durability during the ORR.

Lastly, we investigated reduction methods for the production of FePc/rGO hybrids. In general, different reduction processes result in rGO samples with different properties, which, in turn, affect the final performance of materials or devices composed of rGO [33]. Furthermore, in the hybrid system, the reduction process might influence the molecular structure and/or chemical states of the FePc ultrathin layers. To explore this aspect, we employed hydrothermal [34], chemical [35], and photoreduction methods with hydrazine or NaBH_4 [15, 31, 36] to obtain the hybrid sample. CV measurements of these samples revealed that other methods showed lower ORR activity than one obtained by the electrochemical reduction method (Figure 4-12(a)). Under these latter reduction conditions, Fe^{2+} active sites in phthalocyanine nanodomains did not form presumably because of

complex effects, such as insufficient reduction, formation of iron impurities, poisoning by adsorbed species, or decomposition of molecular and thin-layer structures. XPS elemental analysis (Figure 4-12(b)) indicates that the initial Fe/C atomic ratio in FePc/GO hybrid was not largely changed under any reduction conditions, while the initial O/C atomic ratio decreased significantly by the hydrothermal and chemical reduction methods. The O/C ratio almost unchanged after photoreduction, and thus low-electrical conductivity of rGO due to the high O/C ratio should result in the lowest ORR activity of the sample obtained by the reduction method among the samples. These data also revealed that insufficient reduction of GO should be excluded to describe the lower ORR properties for the sample obtained by hydrothermal and chemical reduction methods than one obtained by the electrochemical reduction method. We observed that Fe 2p_{3/2} XPS spectra and B_{1g} Raman band were unchanged and slightly changed after the hydrothermal reduction and chemical reduction with NaBH₄, respectively (Figure 4-12(c), (d)). Thus, active Fe²⁺ sites like those in the hybrid obtained by the electrochemical reduction method could not be efficiently formed under these reduction conditions. In contrast, Fe 2p_{3/2} band-positions of the sample obtained by the chemical reduction with hydrazine remarkably shifted toward lower binding energy, indicating the production of metallic Fe rather than Fe²⁺ ions, and thus partial decomposition of FePc structure should decrease ORR activity in this case. Indeed, N1s XPS spectra (Figure 4-13) show that the electrochemical method did not alter the N1s peak shape of FePc/GO hybrid; however, the other methods changed N1s spectra in the band shape. Thus, these latter methods partially decompose the framework of FePc, resulting in the insufficiently enhanced ORR properties. These results clearly demonstrated that the formation of ultrathin FePc layer with Fe²⁺ active sites on highly reduced rGO with significant electrical conductivity should be crucial for excellent ORR activity of hybrid catalysis. On the basis of these studies, we have suggested that the reduction step is generally important for obtaining highly functional rGO-based hybrid materials containing multivalent metallic ions

throughout the self-assembly-reduction approach.

4.4 Conclusions

In summary, a self-assembly pathway to FePc/rGO hybrids with excellent ORR activity is presented. Microscopic and spectroscopic investigations suggest that the Fe ion in an N_4 macrocycle was anchored by oxygen functional groups to form FePc nanodomains in the initial self-assembly step. Subsequent electrochemical reduction produced ultrathin FePc layers on conductive rGO. The hybrid catalysts afford a strongly dominating four-electron process for the ORR, owing to efficient electrochemical coupling between FePc and rGO. As a result, an ultrafast ORR as well as improved catalyst durability was achieved. The self-assembly strategy could be broadly extended to the fabrication of hybrid materials comprising GO nanosheets and ultrathin organic layers exhibiting various functional properties.

References

- [1] W. R. Browne, B. L. Feringa, *Annu. Rev. Phys. Chem.* **2009**, 60, 407.
- [2] F. Sedona, M. Di Marino, D. Forrer, A. Vittadini, M. Casarin, A. Cossaro, L. Floreano, A. Verdini, M. Sambi, *Nat. Mater.* **2012**, 11, 970.
- [3] D. G. De Oteyza, J. M. García-Lastra, M. Corso, B. P. Doyle, L. Floreano, A. Morgante, Y. Wakayama, A. Rubio, J. E. Ortega, *Adv. Funct. Mater.* **2009**, 19, 3567.
- [4] W. Auwärter, K. Seufert, F. Bischoff, D. Ecija, S. Vijayaraghavan, S. Joshi, F. Klappenberger, N. Samudrala, J. V. Barth, *Nat. Nanotechnol.* **2012**, 7, 41.
- [5] P. Gambardella, S. Stepanow, A. Dmitriev, J. Honolka, F. M. F. De Groot, M. Lingenfelder, S. S. Gupta, D. D. Sarma, P. Bencok, S. Stanescu, S. Clair, S. Pons, N. Lin, A. P. Seitsonen, H. Brune, J. V. Barth, K. Kern, *Nat. Mater.* **2009**, 8, 189.
- [6] J. Mao, H. Zhang, Y. Jiang, Y. Pan, M. Gao, W. Xiao, H. J. Gao, *J. Am. Chem. Soc.* **2009**, 131, 14136.
- [7] K. Yang, W. D. Xiao, Y. H. Jiang, H. G. Zhang, L. W. Liu, J. H. Mao, H. T. Zhou, S. X. Du, H. J. Gao, *J. Phys. Chem. C* **2012**, 116, 14052.
- [8] R. Chen, H. Li, D. Chu, G. Wang, *J. Phys. Chem. C* **2009**, 113, 20689.
- [9] E. Yoo, H. Zhou, *J. Power Sources* **2012**, DOI: 10.1016/j.jpowsour.2012.11.132.
- [10] E. HaoYu, S. Cheng, K. Scott, B. Logan, *J. Power Sources* **2007**, 171, 275.
- [11] A. Morozan, B. Jusselme, S. Palacin, *Energy Environ. Sci.* **2011**, 4, 1238.
- [12] S. C. Bobaru, E. Salomon, J. M. Layet, T. Angot, *J. Phys. Chem. C* **2011**, 115, 5875.

- [13] J. N. Coleman, M. Lotya, A. O'Neill, S. D. Bergin, P. J. King, U. Khan, K. Young, A. Gaucher, S. De, R. J. Smith, I. V. Shvets, S. K. Arora, G. Stanton, H. Y. Kim, K. Lee, G. T. Kim, G. S. Duesberg, T. Hallam, J. J. Boland, J. J. Wang, J. F. Donegan, J. C. Grunlan, G. Moriarty, A. Shmeliov, R. J. Nicholls, J. M. Perkins, E. M. Grieveson, K. Theuwissen, D. W. McComb, P. D. Nellist, V. Nicolosi, *Science* **2011**, 331, 568.
- [14] R. Ma, T. Sasaki, *Adv. Mater.* **2010**, 22, 5082.
- [15] D. R. Dreyer, S. Park, C. W. Bielawski, R. S. Ruoff, *Chem. Soc. Rev.* **2010**, 39, 228.
- [16] S. Stankovich, D. A. Dikin, R. D. Piner, K. A. Kohlhaas, A. Kleinhammes, Y. Jia, Y. Wu, S. T. Nguyen, R. S. Ruoff, *Carbon* **2007**, 45, 1558.
- [17] S. Park, R. S. Ruoff, *Nat. Nanotechnol.* **2009**, 4, 217.
- [18] M. Jahan, Q. Bao, K. P. Loh, *J. Am. Chem. Soc.* **2012**, 134, 6707.
- [19] Y. Xu, L. Zhao, H. Bai, W. Hong, C. Li, G. Shi, *J. Am. Chem. Soc.* **2009**, 131, 13490.
- [20] Y. Xu, Z. Liu, X. Zhang, Y. Wang, J. Tian, Y. Huang, Y. Ma, Y. Chen, *Adv. Mater.* **2009**, 21, 1275.
- [21] A. Chunder, T. Pal, S. I. Khondaker, L. Zhai, *J. Phys. Chem. C* **2010**, 114, 15129.
- [22] G. I. Cárdenas-Jirón, P. Leon-Plata, D. Cortes-Arriagada, J. M. Seminario, *J. Phys. Chem. C* **2011**, 115, 16052.
- [23] Y. Zhang, G. Mo, X. Li, J. Ye, *J. Power Sources* **2012**, 197, 93.
- [24] C. Zhang, R. Hao, H. Yin, F. Liu, Y. Hou, *Nanoscale* **2012**, 4, 7326.
- [25] H. Yin, H. Tang, D. Wang, Y. Gao, Z. Tang, *ACS Nano* **2012**, 6, 8288.
- [26] K. Parvez, S. Yang, Y. Hernandez, A. Winter, A. Turchanin, X. Feng, K. Müllen, *ACS Nano* **2012**, 6, 9541.
- [27] Y. Liang, Y. Li, H. Wang, J. Zhou, J. Wang, T. Regier, H. Dai, *Nat. Mater.* **2011**, 10, 780.

- [28] Y. Liang, H. Wang, J. Zhou, Y. Li, J. Wang, T. Regier, H. Dai, *J. Am. Chem. Soc.* **2012**, 134, 3517.
- [29] X. Y. Yan, X. L. Tong, Y. F. Zhang, X. D. Han, Y. Y. Wang, G. Q. Jin, Y. Qin, X. Y. Guo, *Chem. Commun.* **2012**, 48, 1892.
- [30] J. S. Spendelow, A. Wieckowski, *Phys. Chem. Chem. Phys.* **2007**, 9, 2654.
- [31] Y. Matsumoto, M. Koinuma, S. Y. Kim, Y. Watanabe, T. Taniguchi, K. Hatakeyama, H. Tateishi, S. Ida, *ACS Appl. Mater. Interfaces* **2010**, 2, 3461.
- [32] Y. Zheng, Y. Jiao, L. Ge, M. Jaroniec, S. Z. Qiao, *Angew. Chem. Int. Ed.* **2013**, 52, 3110.
- [33] A. Ambrosi, A. Bonanni, Z. Sofer, J. S. Cross, M. Pumera, *Chem. Eur. J.* **2011**, 17, 10763.
- [34] Y. Zhou, Q. Bao, L. A. L. Tang, Y. Zhong, K. P. Loh, *Chem. Mater.* **2009**, 21, 2950.
- [35] H. J. Shin, K. K. Kim, A. Benayad, S. M. Yoon, H. K. Park, I. S. Jung, M. H. Jin, H. K. Jeong, J. M. Kim, J. Y. Choi, Y. H. Lee, *Adv. Funct. Mater.* **2009**, 19, 1987.
- [36] Y. Matsumoto, M. Koinuma, S. Ida, S. Hayami, T. Taniguchi, K. Hatakeyama, H. Tateishi, Y. Watanabe, S. Amano, *J. Phys. Chem. C* **2011**, 115, 19280.
- [37] U. A. Paulus, T. J. Schmidt, H. A. Gasteiger, R. J. Behm, *J. Electroanal. Chem.* **2001**, 495, 134.

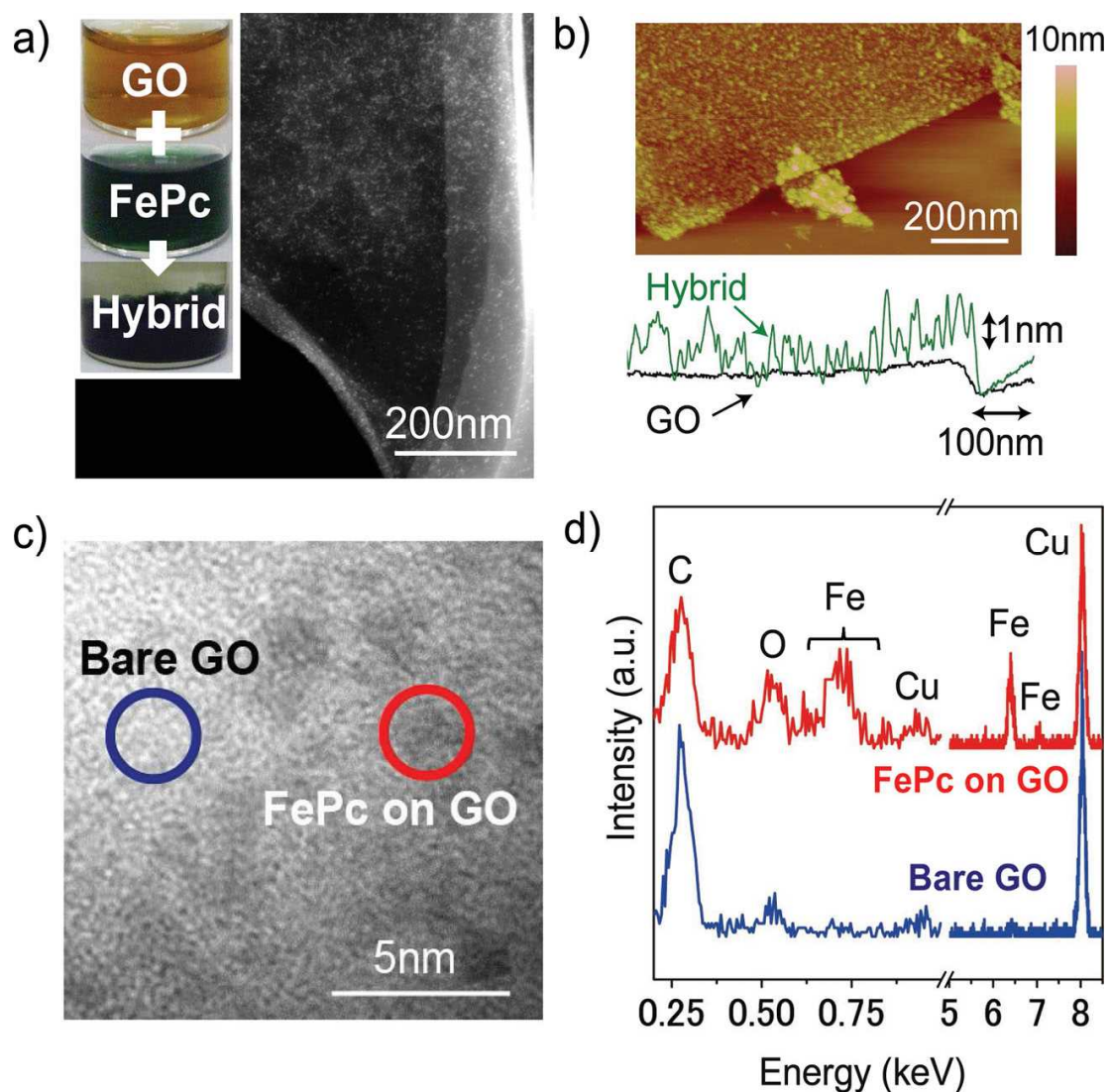


Figure 4-1. (a) HAADF-STEM image of FePc/GO hybrid; interested photographs show GO solution, FePc solution, and precipitates of FePc/GO hybrid. (b) AFM image of FePc/GO hybrid, and cross-sectional AFM image of hybrid and bare GO. (c) Bright-field TEM image of FePc/GO hybrid; the areas enclosed with blue and red circles correspond to typical bare GO and FePc-deposited parts, respectively, in which EDX elemental analysis was performed. (d) Typical EDX spectra measured from bare GO part and FePc-deposited parts. Note that copper from the sample holder was detected.

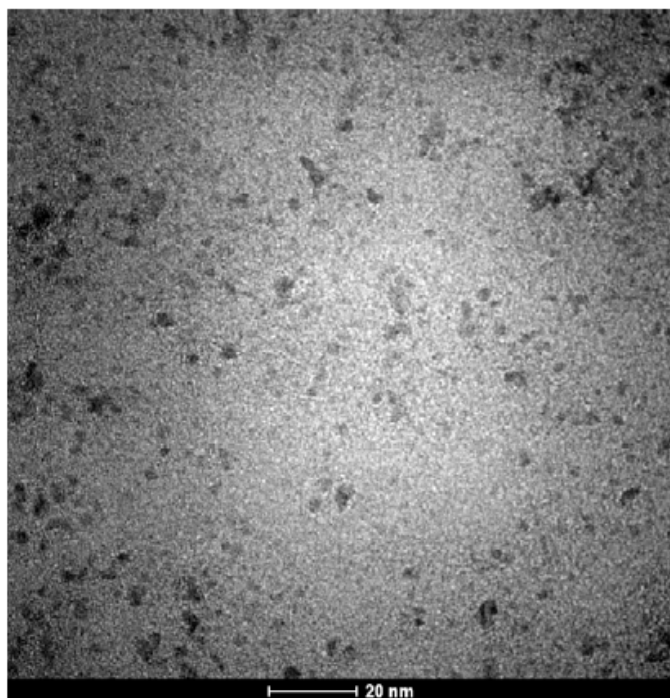


Figure 4-2. TEM image of FePc/GO hybrid.

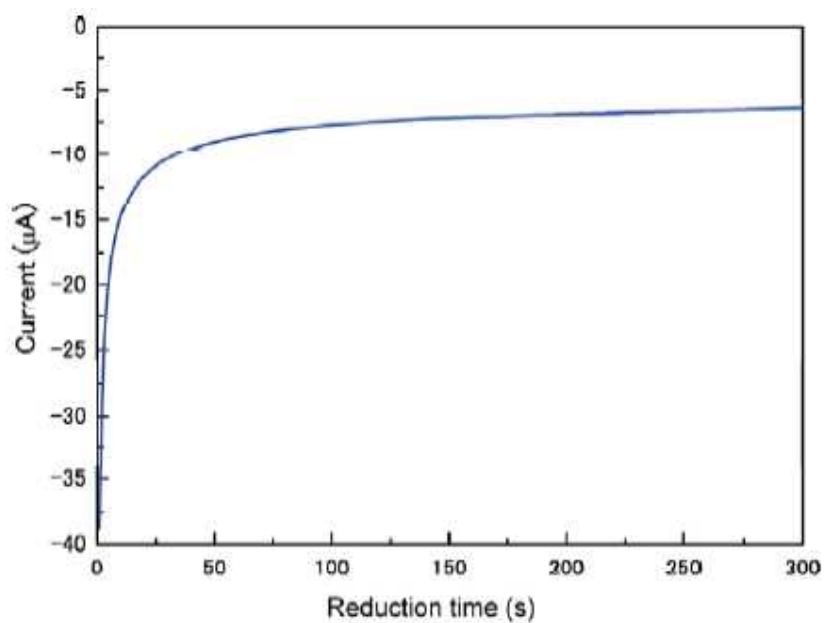


Figure 4-3. Current produced by reduction of FePc/GO hybrid in 0.1M Na₂SO₄ at -1.1 V (vs. Ag/AgCl).

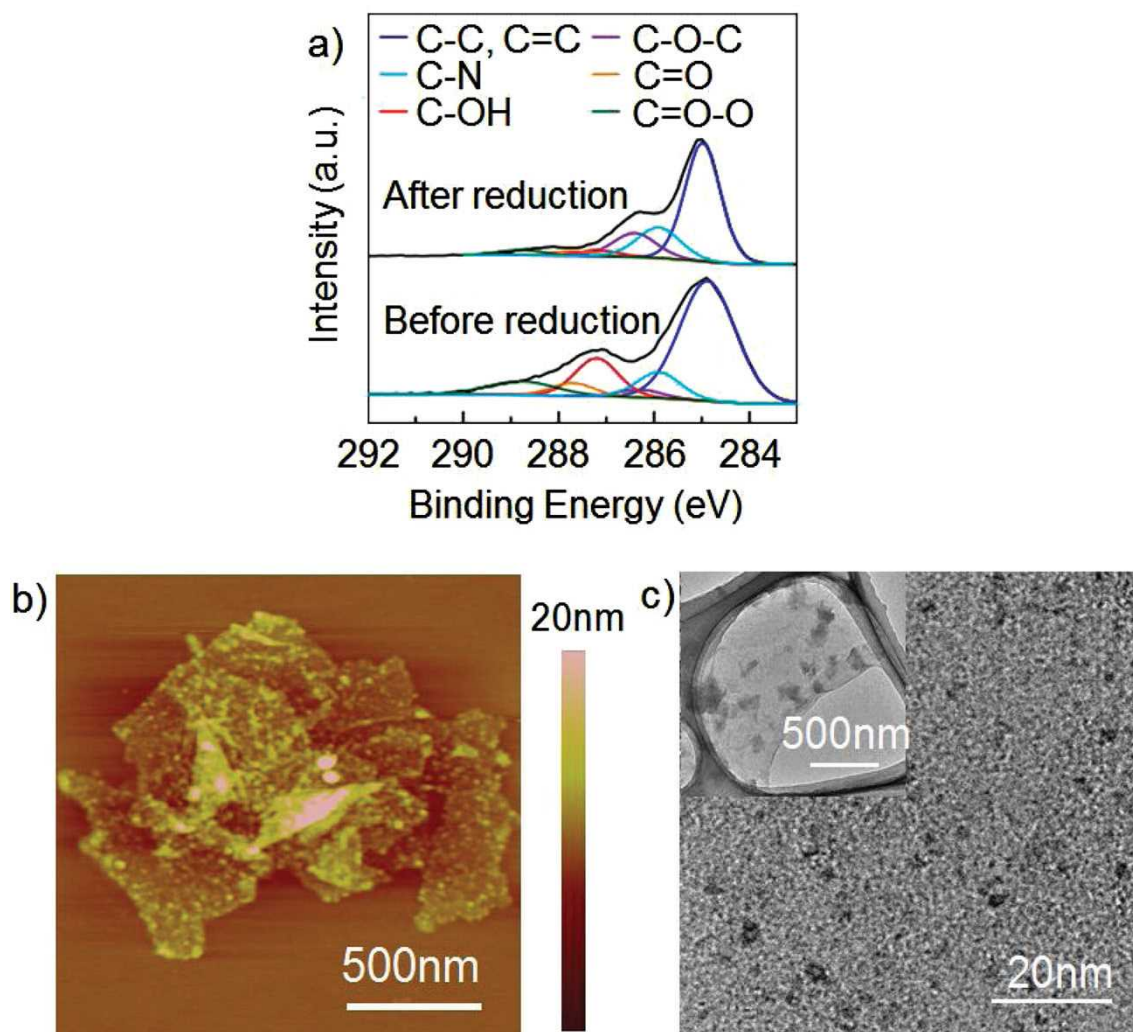


Figure 4-4. (a) C 1s XPS spectra of FePc/GO hybrid before and after electrochemical reduction. (b), (c) AFM and TEM images of FePc/rGO hybrid obtained by electrochemical reduction.

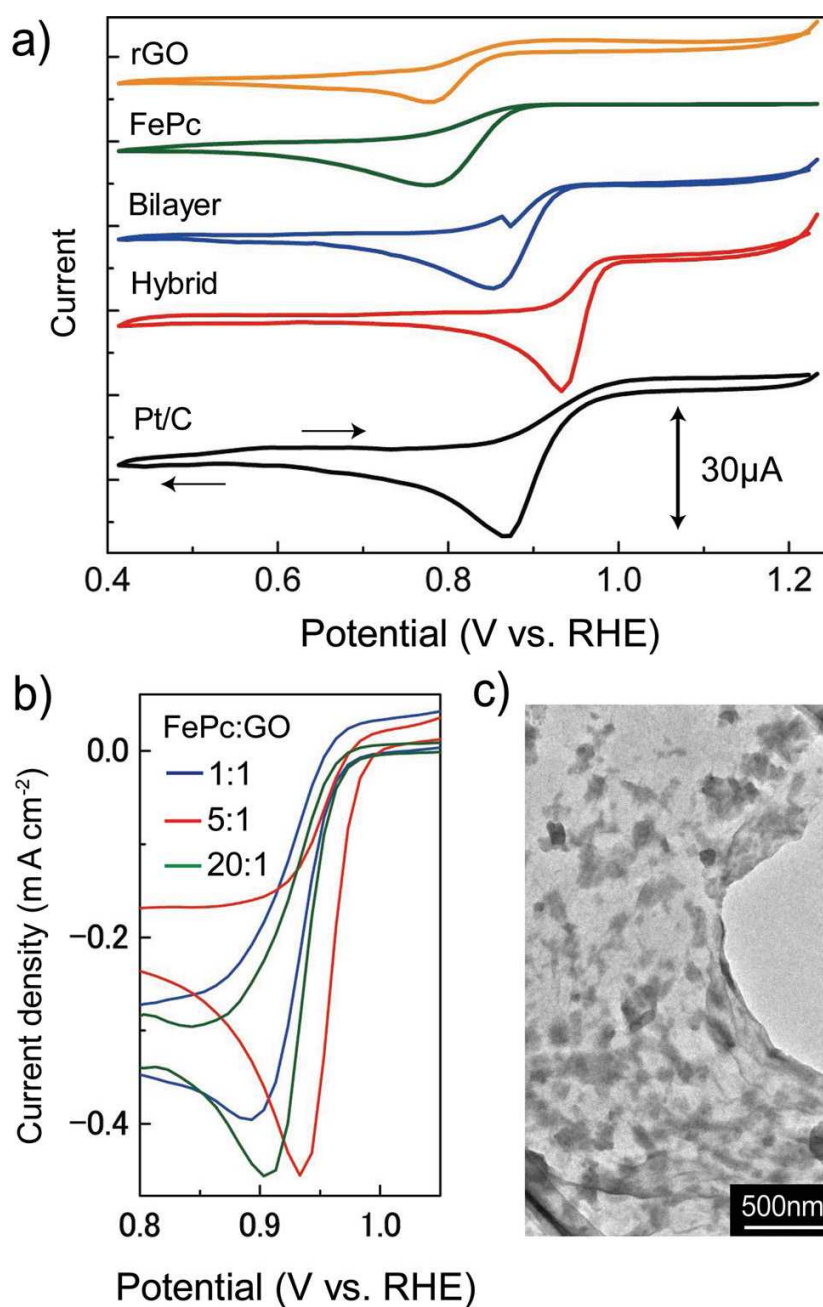


Figure 4-5. (a) CV curves of rGO, FePc, FePc/rGO bilayer, and FePc/rGO hybrid and Pt/C on glassy carbon electrodes in O₂-saturated 1 M KOH. (b) CV curves of FePc/rGO hybrid with FePc:rGO weight ratio of 1:1, 5:1, and 20:1. (c) TEM image of FePc/rGO hybrid with FePc:rGO weight ratio of 20:1.

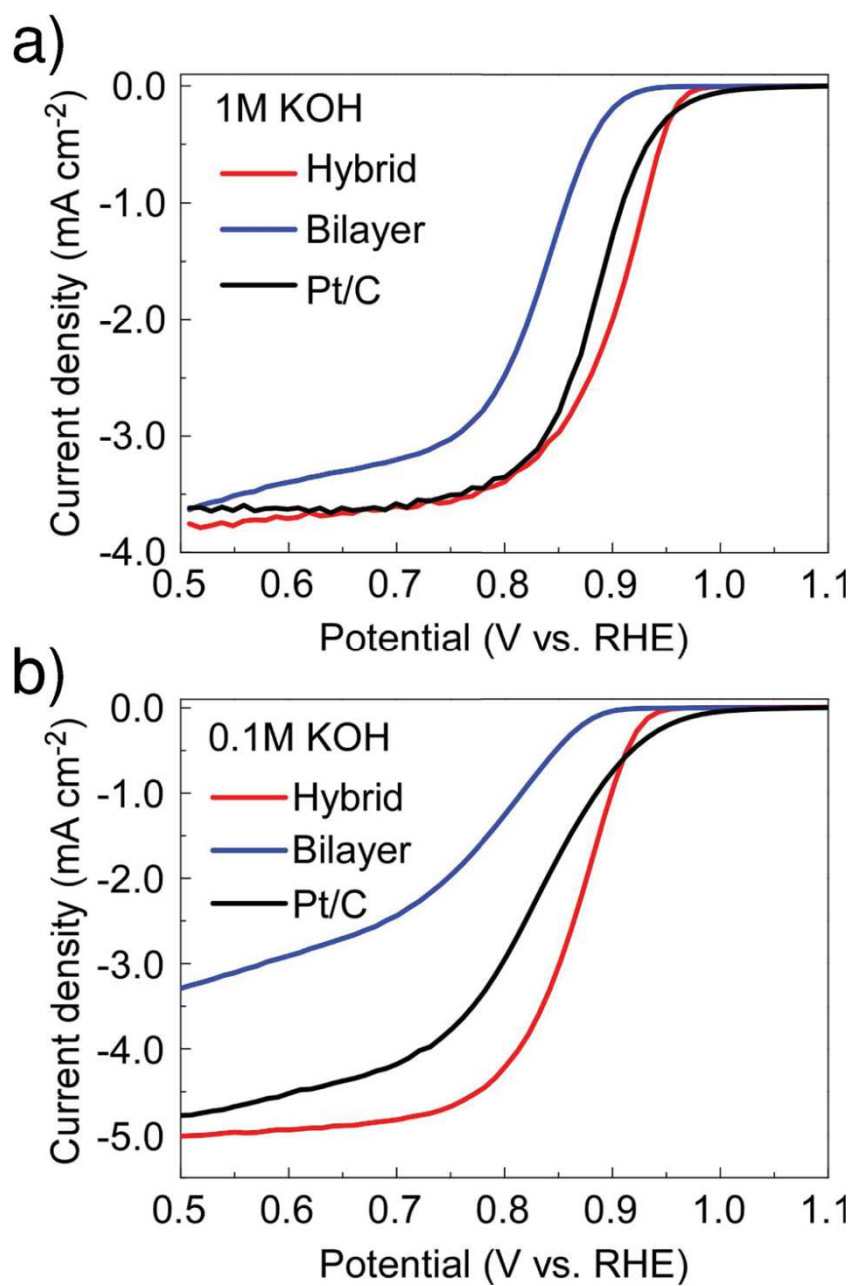


Figure 4-6. Rotating-disk voltammograms of FePc/rGO bilayer, FePc/rGO hybrid, and Pt/C in O₂-saturated (a) 1 M KOH and (b) 0.1 M KOH with a sweep rate of 5 mV s⁻¹ at 1600 rpm.

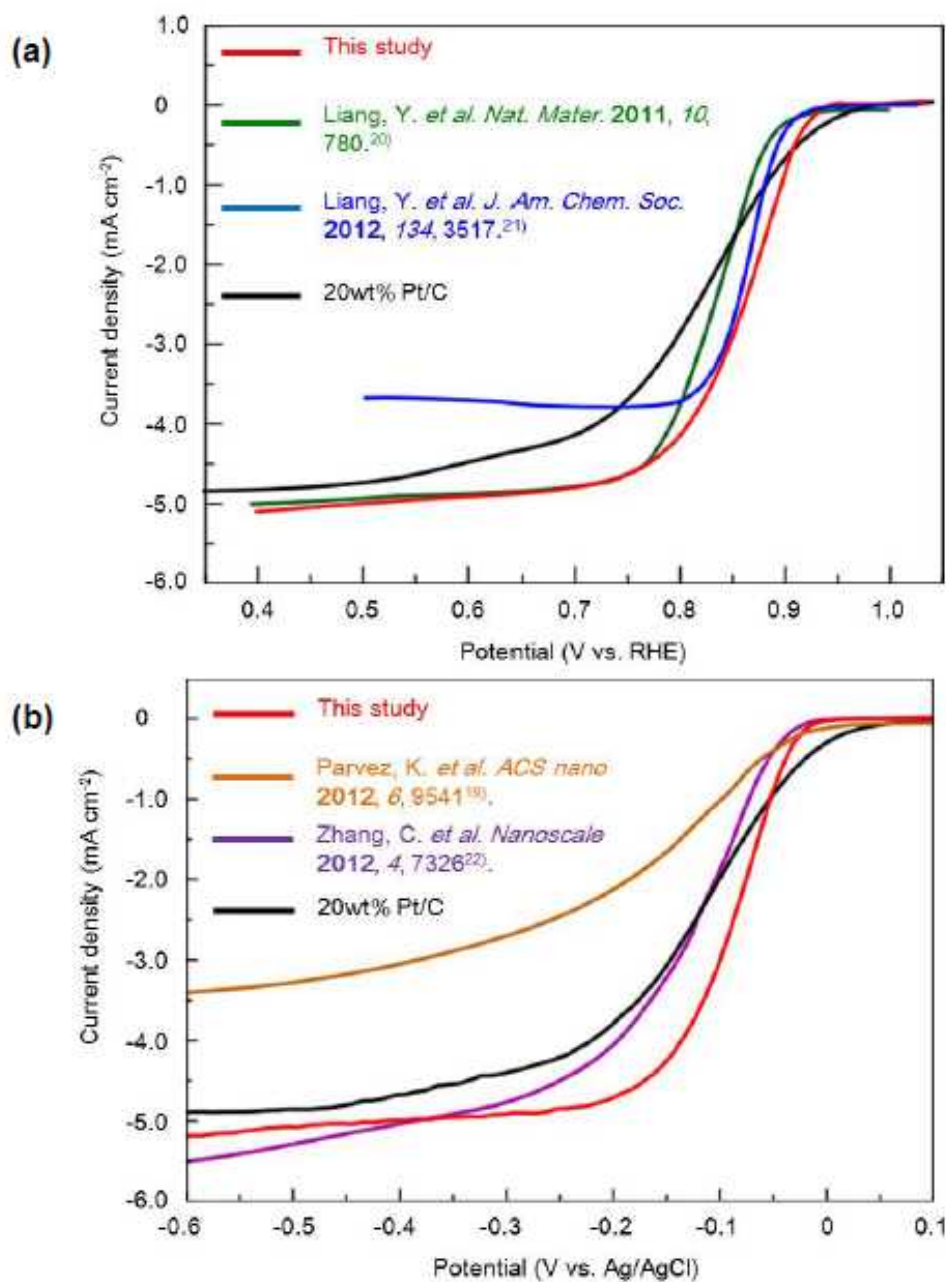


Figure 4-7. Rotating-disk voltammograms of referenced N-rGO-based catalysts along with reference Pt/C and FePc/rGO hybrid prepared in the present study in O₂-saturated 0.1 M KOH with a sweep rate of **(a)** 5 mV s⁻¹ and **(b)** 10 mV s⁻¹ at 1600 rpm.

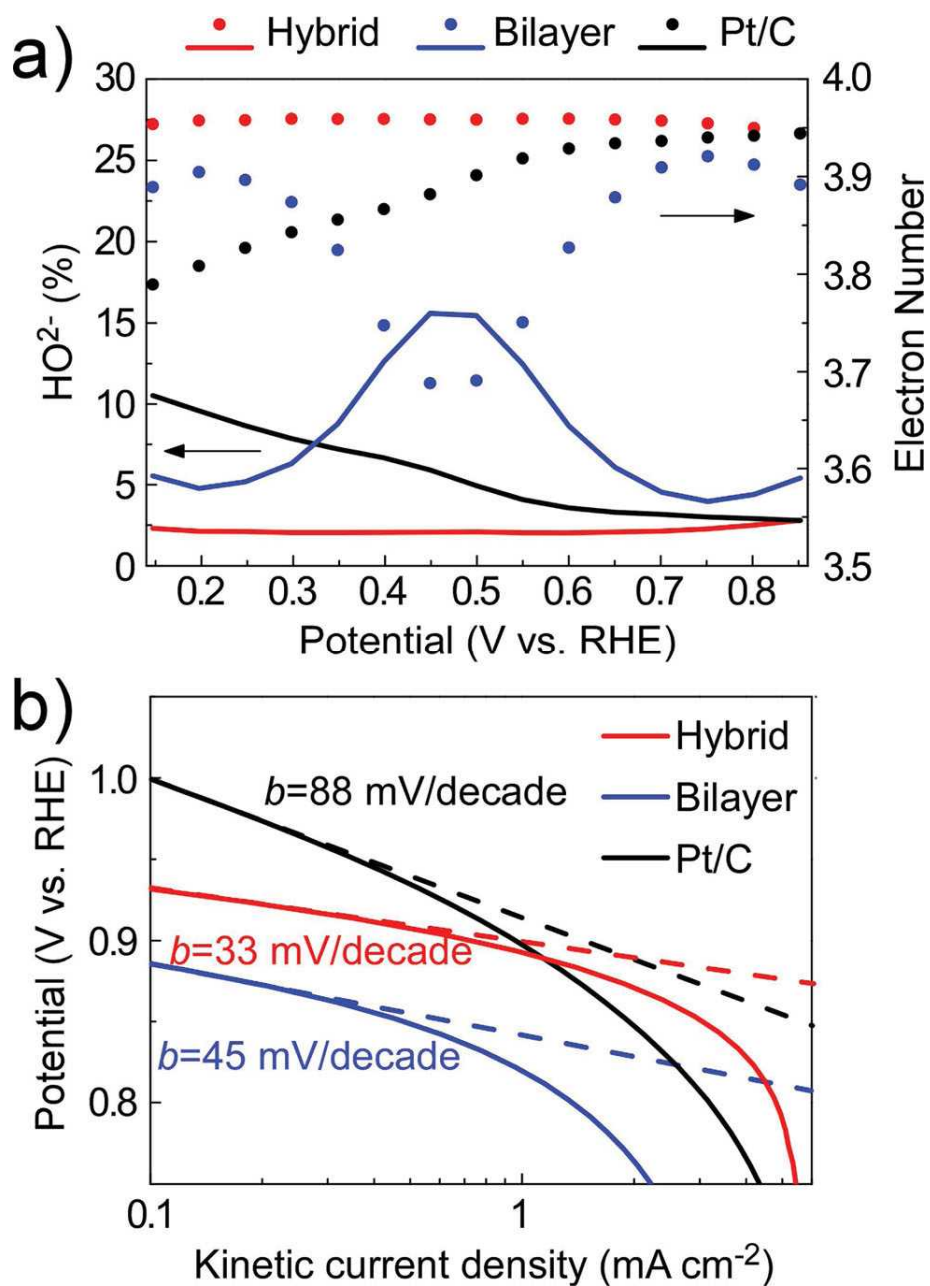


Figure 4-8. (a) Percentage of peroxide (solid line) and the electron transfer number (n) (dotted line) of FePc/rGO bilayer, FePc/rGO hybrid and Pt/C, based on the corresponding RRDE data in 0.1 KOH. (b) Tafel plots of FePc/rGO bilayer, FePc/rGO hybrid, and Pt/C prepared derived by the mass-transport correction of corresponding RRDE data.

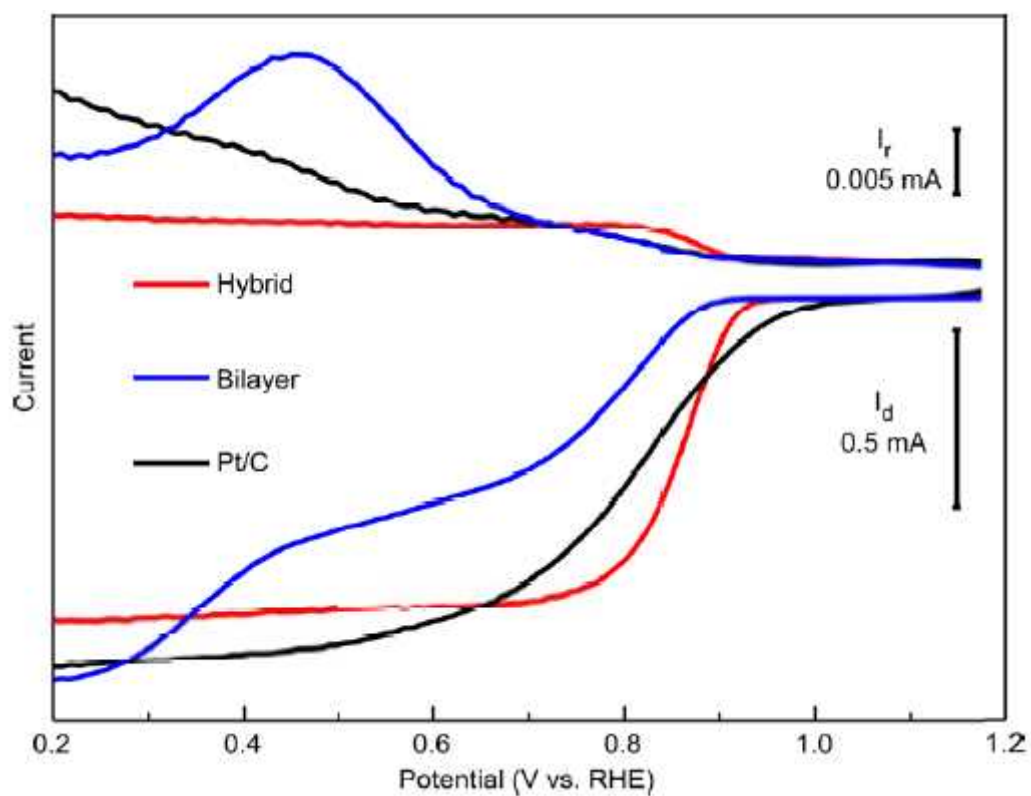


Figure 4-9. Rotating-ring disk voltammograms of FePc/rGO bilayer, FePc/rGO hybrid and Pt/C in O_2 -saturated 0.1 M KOH with a sweep rate of 5mV s^{-1} at 1600 rpm.

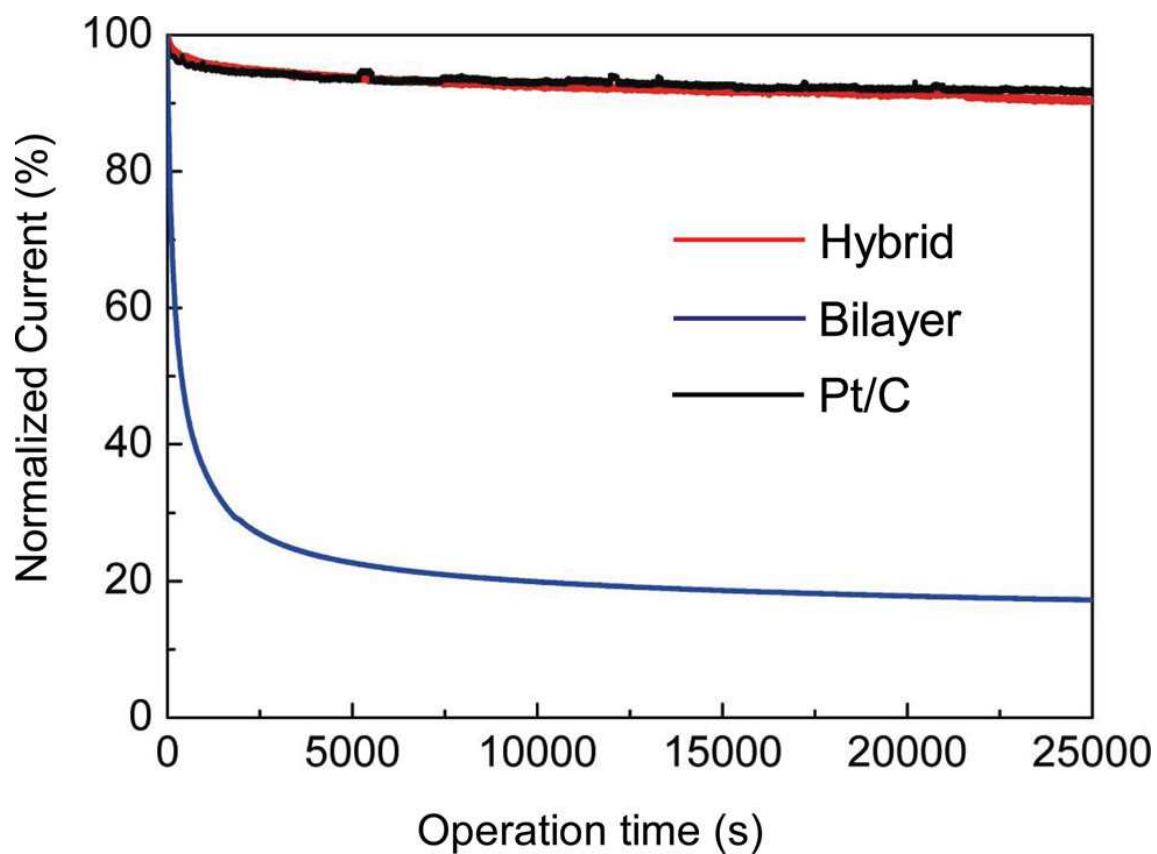


Figure 4-10. Chronoamperometric responses (percentage of current retained versus operation time) of FePc/rGO bilayer, FePc/rGO hybrid and Pt/C kept at 0.70 V versus RHE in O₂-saturated 0.1 M KOH.

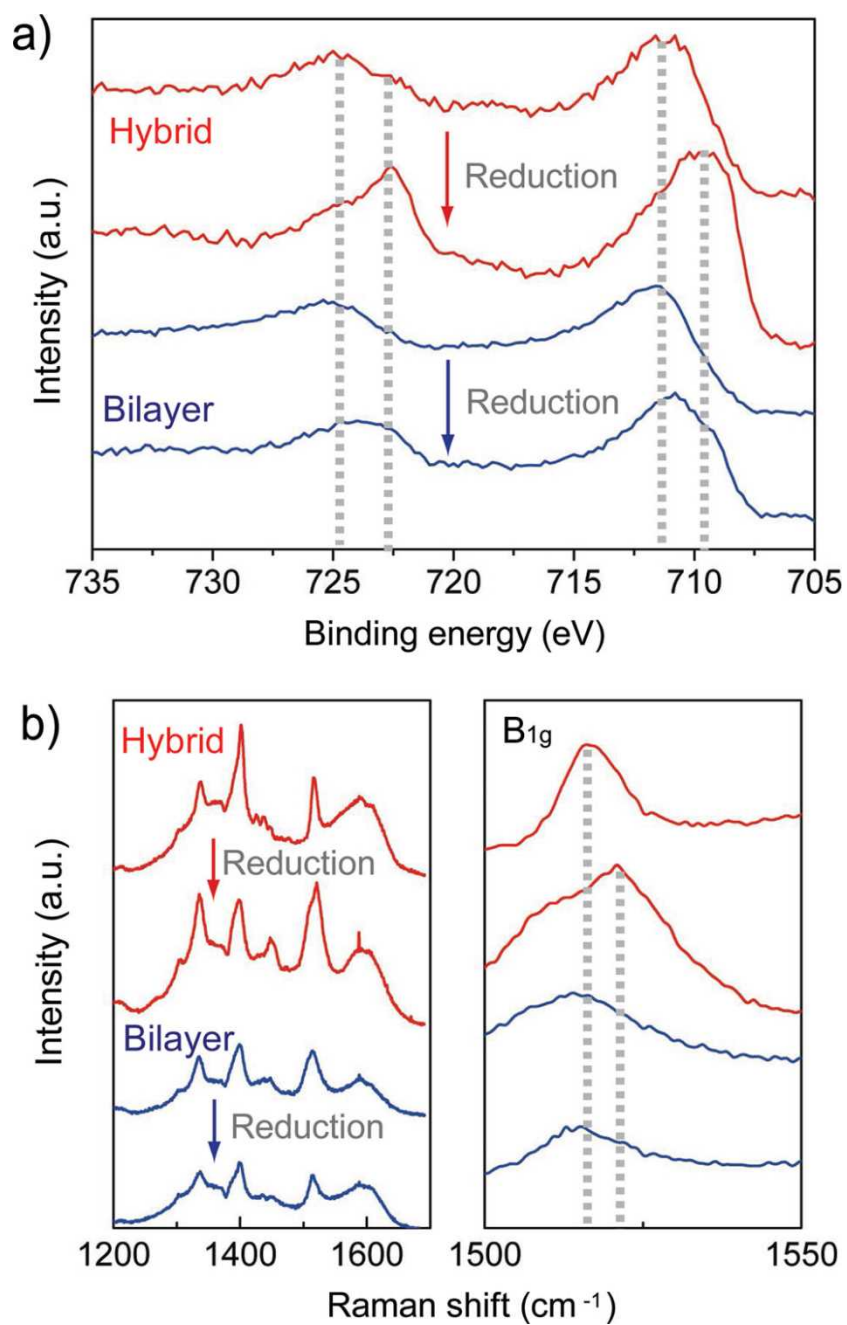


Figure 4-11. (a) Fe $2p_{3/2}$ XPS and (b) Raman spectra for FePc/GO hybrid and bilayer samples before and after electrochemical reduction.

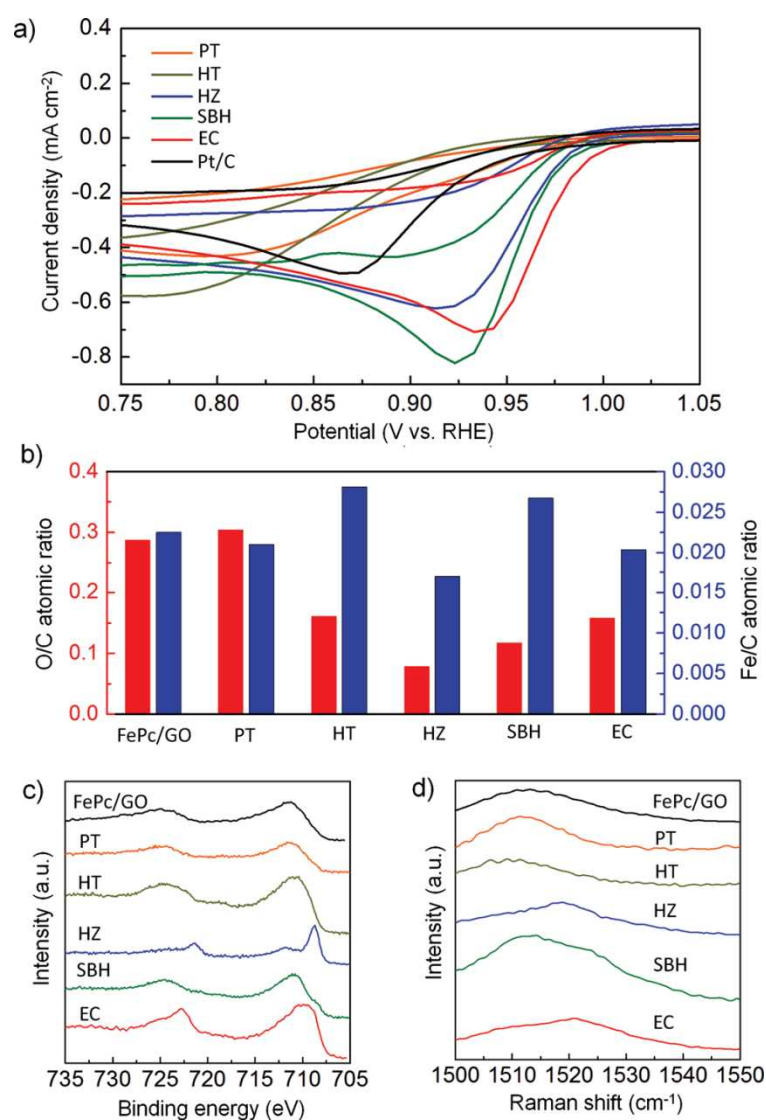


Figure 4-12. (a) CV curves of Pt/C and FePc/GO hybrid reduced by photoreduction method (PT), hydrothermal reduction method (HT), chemical reduction method with hydrazine (HZ) and NaBH₄ (SBH), and electrochemical reduction method (EC) measured in O₂-saturated 1 M KOH. (b) O/C and Fe/C atomic ratios of unreduced FePc/GO, and FePc/GO reduced by PT, HT, HZ, SBH, and EC methods calculated with relative intensity of C1s, O1s, and Fe2p XPS spectra. c) Fe2p XPS and d) Raman spectra of unreduced FePc/GO and FePc/GO hybrid reduced by PT, HT, HZ, SBH, and EC methods.

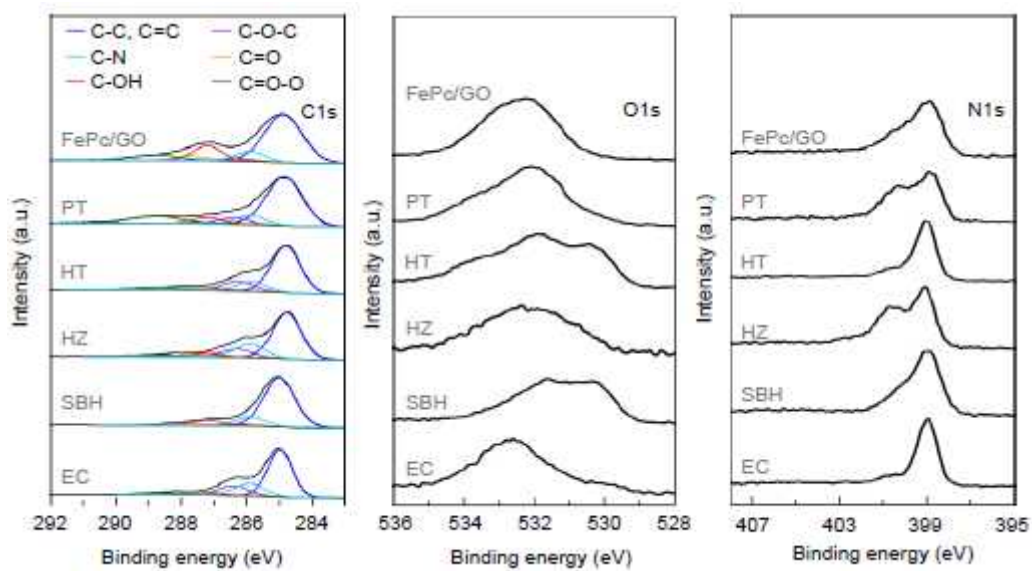


Figure 4-13. C1s, O1s and N1s XPS spectra of unreduced FePc/GO and FePc/GO hybrid reduced by PT, HT, HZ, SBH, and EC methods.

CHAPTER 5

Graphene Oxide Fuel Cell (GOFC)

Overview

Graphene oxide (GO) exhibits relatively high proton conduction even at low relative humidity (*RH*) and temperatures. Thus, multilayered GO film (GO paper) is a promising electrolyte in various cells and batteries. We report the in-plane and through-plane proton conductivities of GO paper at low *RH* and room temperature. The conductivities were $10^{-5}\sim 10^{-4}$ S cm^{-1} at *RH* of 10~20%. We examined the performance of a graphene oxide fuel cell (GOFC) with GO paper as the electrolyte at low *RH* (< 20%) and room temperature. We demonstrated that a simple membrane electrode assembly (MEA) based on Pt/GO/Pt system functioned as a H₂/O₂ fuel cell. The GOFC with Pt/C electrodes afforded better fuel cell performance than a MEA composed of Pt/C electrodes and Nafion electrolyte. GO paper composed of nano-sized GO (nanoGO) flakes enhanced the performance of the GOFC, particularly the current density. Furthermore, a composite of iron phthalocyanine (FePc) /reduced GO (rGO)/TiO₂ could act as the Pt-free oxygen electrode in GOFC, although the fuel cell performance should be improved for practical applications. Our study suggests that a low cost GOFC without a Nafion electrolyte and noble metal electrodes could be fabricated in the near future.

5.1 Introduction

GO is a promising material because of its many excellent chemical and physical properties, which arise from various oxygenated functional groups ^[1-6]. Multilayered GO nanosheets (GO paper) exhibit high proton conduction ^[7-9]. The main oxygen functional group in GO is epoxide. It

acts as the site for proton transfer after water molecules bind to it, even at low *RH* and room temperature [10]. The relatively high proton conductivity under these conditions suggests that GO paper could act as a proton electrolyte in various cells and batteries [11–16]. The proton conductivity of the GO paper is lower than that of the conventional Nafion electrolyte, which is usually used at high *RH* (~100%) [17, 18], while the overall conduction of the GO paper will be similar to that of Nafion if the GO paper is less than a tenth of the thickness of the Nafion.

It has been reported that various gases do not pass through the GO paper, even when the GO is very thin (0.1 μm) [19]. This means thin GO paper is well suited as an electrolyte for the H_2/O_2 fuel cell, because of the high proton conduction and the H_2 and O_2 gas shielding. Nafion electrolytes must be thick in order to achieve gas shielding ($> 10^2 \mu\text{m}$). Moreover, GO paper is much cheaper than Nafion. A mixture of GO paper and Nafion has been used as the electrolyte for a fuel cell, and it acted as an electrolyte even at relatively low *RH* (25%) [8]. Sulfonic acid functionalized GO (SGO) has been used as an electrolyte without Nafion, and tested in a H_2/O_2 fuel cell at 25% *RH* and 40 °C, with Pt/C electrodes [12].

Here we report the performance of a simple H_2/O_2 fuel cells with a 100% GO paper (< 1 atom% S) electrolyte (GOFC) as well as the proton conductivities at low *RH* and 23–25 °C.

5.2 Experimental

5.2-1 Synthesis of GO and nanoGO

The GO was prepared from natural graphite powder (special grade reagent, Wako Ltd.) by Hummers' method [20]. Graphite powder (2.0 g), NaNO_3 (2.0 g, special grade reagent, Wako Ltd.), and 98% H_2SO_4 (92 mL, special grade reagent, Wako Ltd.) were mixed at 0 °C in an ice-water bath. KMnO_4 (12 g, special grade reagent, Wako Ltd.) was added very slowly. The reaction mixture was removed from the ice-water bath and stirred to oxidize the graphite powder for 45 min at 95 °C. The

resulting mixture was diluted with distilled water and 30% H₂O₂ (5 mL, special grade reagent, Wako Ltd.) was added to neutralize any remaining KMnO₄. The product was washed with 5% HCl (special grade reagent, Wako Ltd.), centrifuged several times at 3000 rpm to remove excess HCl, and dried in an oven at 70 °C for 7 days. The GO was suspended in distilled water by bath sonication for 2 h, and the suspension was ultracentrifuged at 10000 rpm. The supernatant was used as the GO suspension. The atomic force microscopy (AFM; Nanoscope V, Digital Instruments) image and X-ray photoelectron spectroscopy (XPS; SigmaProbe, Thermo Scientific) spectrum of the GO are shown in Figure 5-1(a), respectively. The sizes of the GO sheets were in the range 0.1~1 μm, and the oxygen content (O/(C + O)) was about 30%.

The nanoGO was also prepared from natural graphite powder (99.9%, Alfa Aesar) by the modified Hummers' method [21]. Briefly, graphite powder (3.0 g) and 98% H₂SO₄ (400 mL) were mixed at room temperature using a mechanical stirrer. After 10 min, KMnO₄ (3.0 g) was added, and the mixture turned green. Additional KMnO₄ (3.0 g) was added when the green color faded until the mixture turned pink. The mixture was diluted and neutralized using the same procedure described for the GO. The mixture was then washed with 5% HCl and ultracentrifuged at 10000 rpm and dried in an oven at 70 °C for 7 days. The GO was suspended in distilled water by bath sonication for 2 h, and the suspension was ultracentrifuged at 10000 rpm. The supernatant contained the nanoGO suspension. The transmission electron microscope (TEM; Tecnai G2 F20, FEI Company) image and XPS spectrum of the nanoGO are shown in Figure 5-1(b), respectively. The GO particles were several nanometers in size, and the oxygen content was 33%. The carboxyl group content was high compared with that of the conventional GO sample shown in Figure 5-1(a) because nanoGO has many edges.

5.2-2 Preparation of GO paper as the electrolyte

The GO suspensions (4 mg mL^{-1} , 20~50 mL) were filtered using a membrane filter with a pore size of 0.025~0.4 μm under reduced pressure overnight in order to obtain GO paper. The thickness of the GO paper was 10~60 μm . Figure 5-2 shows the SEM (JSM-7600F, JEOL) images of the surface and the cross section of the GO paper.

5.2-3 Measurement of the proton conductivity of the GO paper

The in-plane proton conductivity of the GO papers was measured by the dc and ac four probe and the through-plane proton conductivity was measured by the ac two-probe method [8, 22]. There were sputtered Pt (150 nm) electrodes on both sides of the GO paper. For the ac methods, the impedance spectra were obtained using an impedance phase analyzer (1260, Solartron) in the frequency range of 1 MHz~1 Hz with an ac amplitude of 50 mV in a *RH* range of 2~95% at temperature of 25 °C. The *RH* was controlled by using $\text{H}_2\text{SO}_4/\text{H}_2\text{O}$ solutions of various concentrations. To calculate the activation energy of the proton conductivities, the measurements were taken at 20~50°C [22].

5.2-4 Fabrication of the GOFC

The GO paper used in the GOFC was 10~20 μm thick. The Pt electrodes were deposited on the GO paper surfaces using a sputtering machine (K575K, Emitech), and were 8.5~306 nm thick. Pt/C reference electrodes were used. The Pt/C catalyst ink was prepared by mixing Pt/C (0.25 g, 45.9wt% Pt, Tanaka Precious Metals Ltd.) with Nafion solution (2.14 g, 5wt%, Wako Ltd.) and H_2O (4 mL) under sonication for 30 min, and the mixture was stirred for 14~15 h. The catalyst ink was cast onto both sides of GO paper surfaces. The FePc/rGO/TiO₂ hybrid electrode was prepared as a noble metal-free cathode. The FePc/GO/TiO₂ catalyst ink was fabricated from a FePc ethanol dispersion. A FePc (~90%, Aldrich) ethanol dispersion (20 mL, 0.5 g L^{-1}) was mixed with a GO

suspension (4 mL, 0.5 g L⁻¹) and TiO₂ nanoparticles (P25, Aerosil Ltd.) in a FePc:GO:TiO₂ weight ratio of 1:1:0.1. The ink was cast onto the GO paper surfaces, and then reduced by irradiating it with a 500 W Hg lamp (USH-500D, Ushio) for 10 min in order to increase the electrode conduction by reducing the GO [23, 24].

5.2-5 Fuel cell performance tests

The GOFC was placed in the fuel cell test chamber (Figure 5-3) at 23~25°C. The electrode areas were 1 cm², and pure H₂ and O₂ were directly fed to each chamber at a flow rate of 10 mL min⁻¹ and 20 mL min⁻¹, respectively. The *RH* in both chambers was checked at each gas exhaust port, and was 10~20%.

5.3 Results and Discussion

5.3-1 Proton conduction of GO paper

Figure 5-4(a) and (b) shows the in-plane and through-plane proton conductivities of GO papers as a function of *RH*. For the in-plane conductivities, the same values were obtained by the ac and dc methods for the same thickness. For the ac method, the proton resistance was obtained from the Cole-Cole plots (Figure 5-4(c)). The conductivity of the through-plane was lower than that of the in-plane, although they were similar at low *RH*. There are two spaces for the through-plane proton conduction, the interlayer and edge spaces, whereas the in-plane proton conduction happens through the interlayer spaces.

The in-plane proton conductivity a little decreased with the thickness of the GO paper, in which this tendency is reproducible. This indicates that layer-layer interactions depended on the thickness of GO layers. As a result, interlayer proton diffusion rate changed by the thickness. In an ongoing work of our research group, we are studying in more detail on the unique

thickness-dependent ion-transport properties of GO layers. We also revealed that the through-plane is lower than the in-plane proton conductivity. In the through-plane conduction, the protons move from one layer to another through the edge spaces. The proton movement through the edge spaces will be more difficult than that in the inter-layer space because of the small number of epoxide groups on the edges of the GO [10], lowering the through-plane proton conductivity. It is notable that the through-plane and in-plane proton conductivities were similar at low *RH*, which suggests that the effect of water molecules on the proton movement was small for the edge spaces compared with the interlayer spaces. The activation energies of the in-plane and through-plane were also similar; 0.06~0.07 eV at low *RH*. These small values indicate that the proton conduction is based on the Grotthuss mechanism [25, 26]. The conductivity of the through-plane was more important when the GO paper was used as the electrolyte. The resistance was calculated to be around 10 Ω at 10~20% *RH*. The GO paper resistance should be lower than the calculated values, because the *RH* in the GO paper increases during the current flow, owing to the production of water in the GO paper bulk, which cannot be controlled. The GO paper resistance scarcely affected the GOFC performance when the maximum current was lower than 10 mA cm⁻¹. The proton conductivities of the present GO papers approached that of SGO at *RH* of 100% (10⁻²~10⁻¹ S cm⁻¹) [12].

5.3-2 Performance of GOFC

We also examined whether the H₂ and O₂ gases leaked through the GO paper with ca. 10 μm -thickness. The amount of H₂ and O₂ gases were evaluated by gas chromatography in the chamber filled with air and N₂, respectively, which was separated from the H₂ and O₂ chamber by the GO paper, respectively. The results showed that H₂ was not detected, and intensity of O₂ signal was in the background level. Thus, the present thin GO paper was suitable as an electrolyte because it effectively separated the gases.

Figure 5-5(a) shows the typical cell performance of the GOFC, where the sputtered Pt (150 nm) was used for both electrodes. The open circuit voltage (OCV) was 0.6~0.9 V, the highest short circuit current (SCC) was 8~10 mA cm⁻², and the highest maximum power density (MPD) was 0.3~0.4 mW cm⁻². Thus, the GO paper acted as the fuel cell electrolyte even at low *RH* and at room temperature. Note that the performance of each MEA was slightly different because of difficulties to perfectly control thickness of GO paper and *RH* in our experiments, whereas cell-performance was reproducible within above ranges. It is remarkable that linear fitting of the current-voltage data at 10 Ω for the GO paper showed better performance than the experimental results (see Figure 5-5(a)). Thus, the proton conduction of the present GO paper did not affect the current density of the MEA. Namely, the low MPD of the GOFC, mainly caused by the low current density, was attributed to the electrode configuration at the electrode/GO interface rather than the proton conduction of the GO paper.

Next, we controlled the thickness of the Pt electrodes in order to optimize the electrode/GO interfacial properties. Figure 5-5(b)~(d) show the dependences of the OCV, SCC, and MPD on the sputtered Pt film thickness. The OCV was highest for the thinnest Pt film (8.5 nm), because the Pt on the GO paper surface acted directly as a highly active electrocatalyst. However, the conductivity of the Pt thin film was not sufficient to allow a high current to flow. On the other hand, a thick Pt film interfered with the formation of the important electrode/gas/GO electrolyte three-phase interface, leading to the very low OCV and SCC. Consequently, the optimum thickness giving maximum SCC and MPD values was about 150 nm for the Pt electrodes.

Commercially available Pt/C was employed as electrodes in order to further improve the fuel cell performance of GOFC. The Pt/C electrode exhibit porous structure, which meant that electrode/gas/electrolyte interface area is large, leading to a high performance fuel cell [14, 27]. Figure 5-6 shows the performance of the GOFC with Pt/C electrodes. The performance was superior to that

of the Pt/GO/Pt GOFC (Figure 5-5(a)). It is remarkable that the GOFC with Pt/C electrodes shows better fuel cell performance than a MEA composed of Pt/C electrodes and Nafion electrolyte layer with ca. 150 μm thickness. This demonstrates great potential of GO paper as a low-cost electrolyte for practical fuel cells. Nevertheless, the current was limited by the GO proton resistance in high cell voltage range in this system as well as in the Pt/GO/Pt system aforementioned (see Figure 5-6 and Figure 5-5(a), respectively). We revealed that using nanoGO flakes to fabricate GO paper would be an effective way to further improve the cell performance (Figure 5-7); the current density from a Pt/nanoGO/Pt cell were approximately 2 times larger than that from Pt/GO/Pt paper (Figure 5-5(a)). The current density was directly related to the reactive surface area in the electrode/GO interface. Consequently, the high current density was gained presumably due to the high surface area of nanoGO.

Lastly, we employed a Pt-free oxygen reduction catalyst in GOFC. Figure 5-8 shows the performance of the GOFC with FePc/rGO/TiO₂ electrode (O₂ electrode) and sputtered Pt electrode (H₂ electrode). The OCV was 0.7~0.8 V, indicating that the FePc/rGO acted as an excellent electrode for oxygen reduction reaction [24]. Consequently, we successfully fabricated a GOFC with a noble metal-free oxygen electrode. However, the current was small. Thus, FePc/rGO/TiO₂ electrodes with a high surface area must be a key to achieve a high current density in the Pt-free GOFC.

5.4 Conclusions

The in-plane and through-plane proton conductivities of GO paper were measured at low *RH* at room temperature. The conductivities were $10^{-5}\sim 10^{-4}$ S cm^{-1} at *RH* of 10~20% at 25°C. The performance of the GOFCs with GO paper as the electrolyte was measured at a low *RH* of 10~20% at 23~25°C. We confirmed that a sputtered Pt film (150 nm)/GO (10~20 μm)/Pt simple system

worked as a H₂/O₂ fuel cell. The GOFC with Pt/C electrodes afforded better fuel cell performance than a MEA composed of Pt/C electrodes and Nafion electrolyte. The electrolyte composed of nanoGO increased the active surface area at the Pt/GO interfaces by making the interface more porous, leading to a high power density for the GOFC at low *RH* at room temperature. The GOFC using the FePc/rGO/TiO₂ oxygen electrode afforded a large OCV, while the current density must be increased for applications. These results suggest that it will be possible to fabricate low-cost, high-performance GOFC without a Nafion electrolyte and noble metal electrodes in the near future.

References

- [1] G. Eda, M. Chhowalla, *Adv. Mater.* **2010**, 22, 2392.
- [2] F. Kim, L. J. Cote, J. X. Huang, *Adv. Mater.* **2010**, 22, 1954.
- [3] M. D. Stoller, S. J. Park, Y. W. Zhu, J. H. An, R. S. Ruoff, *Nano Lett.* **2008**, 8, 3498.
- [4] J. Z. Shang, L. Ma, J. W. Li, W. Ai, T. Yu, G. G. Gurzadyan, *Scientific Reports* **2012**, 2, Article number: 792.
- [5] Y. Y. Liang, Y. G. Li, H. L. Wang, H. Dai, *J. Am. Chem. Soc.* **2013**, 135, 2013.
- [6] L. T. Qu, Y. Liu, J. B. Baek, L. Dai, *ACS Nano* **2010**, 4, 1321.
- [7] W. Gao, N. Singh, L. Song, Z. Liu, A. L. M. Reddy, L. J. Ci, R. Vajtai, Q. Zhang, B. Q. Wei, P. M. Ajayan, *Nat. Nanotech.* **2011**, 6, 496.
- [8] H. Zarrin, D. Higgins, Y. Jun, Z. W. Chen, M. Fowler, *J. Phys. Chem. C* **2011**, 115, 20774.
- [9] M. R. Karim, M. Nakai, T. Matsui, K. Hatakeyama, T. Taniguchi, M. Koinuma, Y. Matsumoto, T. Akutagawa, T. Nakamura, S. Noro, T. Yamada, H. Kitagawa, S. Hayami, *J. Am. Chem. Soc.* **2013**, 135, 8097.
- [10] M. Koinuma, C. Ogata, Y. Kamei, K. Hatakeyama, H. Tateishi, Y. Watanabe, T. Taniguchi, K. Gezuhara, S. Hayami, A. Funatsu, M. Sakata, Y. Kuwahara, S. Kurihara, Y. Matsumoto, *J. Phys. Chem. C* **2012**, 116, 19822.
- [11] K. Feng, B. B. Tang, P. Y. Wu, *ACS Appl. Mater. & Interfaces* **2013**, 5, 1481.
- [12] R. Kumar, K. Scott, *Chem. Commun.* **2012**, 48, 5584.
- [13] R. Kumar, C. X. Xu, K. Scott, *RSC Adv.* **2012**, 2, 8777.
- [14] B. Mecheri, V. Felice, Z. Zhang, A. D'Epifanio, S. Licoccia, A. C. Tavares, *J. Phys. Chem. C* **2012**, 116, 20820.
- [15] Y. C. Cao, C. X. Xu, X. Wu, X. Wang, L. Xing, K. Scott, *J. Power Sources* **2011**, 196, 8377.
- [16] C. W. Lin, Y. S. Lu, *J. Power Sources* **2013**, 237, 187.

- [17] G. H. Li, C. H. Lee, Y. M. Lee, C. G. Cho, *Solid State Ionics* **2006**, 177, 1083.
- [18] B. Dong, L. Gwee, D. Salas-de la Cruz, K. I. Winey, Y. A. Elabd, *Nano Lett.* **2010**, 10, 3785.
- [19] R. R. Nair, H. A. Wu, P. N. Jayaram, I. V. Grigorieva, A. K. Geim, *Science* **2012**, 335, 442.
- [20] W. S. Hummers Jr., R. E. Offeman, *J. Am. Chem. Soc.* **1958**, 80, 1339.
- [21] A. Dimiev, D. V. Kosynkin, L. B. Alemany, P. Chaguine, J. M. Tour, *J. Am. Chem. Soc.* **2012**, 134, 2815.
- [22] T. Yamada, M. Sadakiyo, H. Kitagawa, *J. Am. Chem. Soc.* **2009**, 131, 3144.
- [23] Y. Matsumoto, M. Koinuma, S. Ida, S. Hayami, T. Taniguchi, K. Hatakeyama, H. Tateishi, Y. Watanabe, S. Amano, *J. Phys. Chem. C* **2011**, 115, 19280.
- [24] T. Taniguchi, H. Tateishi, S. Miyamoto, K. Hatakeyama, C. Ogata, K. Koga, A. Funatsu, S. Hayami, Y. Makinose, N. Matsushita, M. Koinuma, Y. Matsumoto, *Part. & Part. Syst. Charact.* **2013**, 30, 1063.
- [25] N. Agmon, *Chem. Phys. Lett.* **1995**, 244, 456.
- [26] K. Checkiewicz, G. Zukowska, W. Wieczorek, *Chem. Mater.* **2001**, 13, 379.
- [27] T. Nakajima, T. Tamaki, H. Ohashi, T. Yamaguchi, *J. Electrochem. Soc.* **2013**, 160, F129.

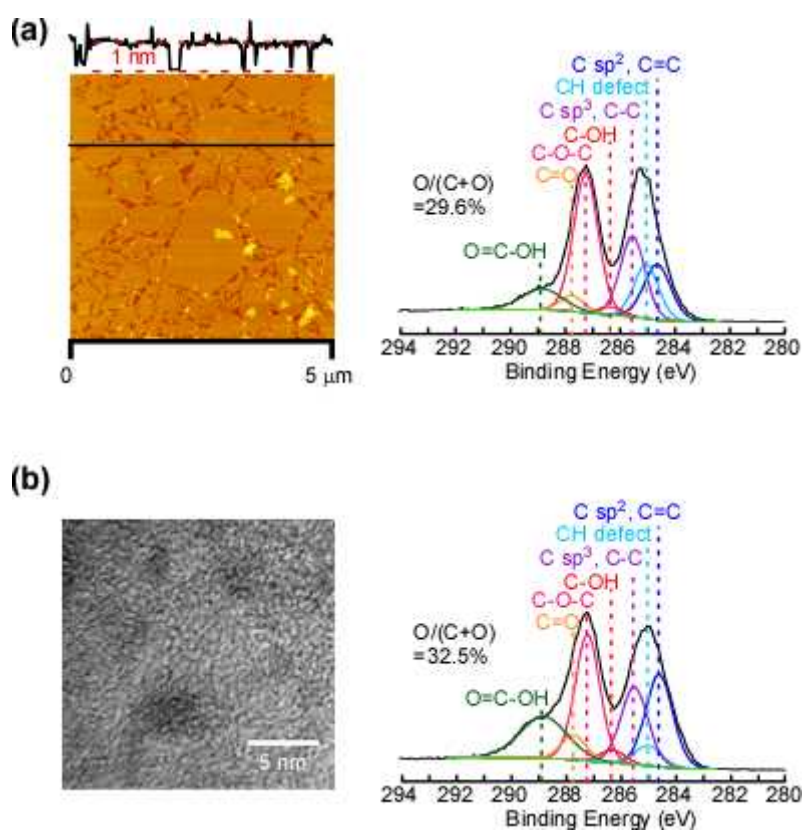


Figure 5-1. (a) (left) AFM image and (right) XPS spectrum of the GO. (b) (left) TEM image and (right) XPS spectrum of nano-sized GO.

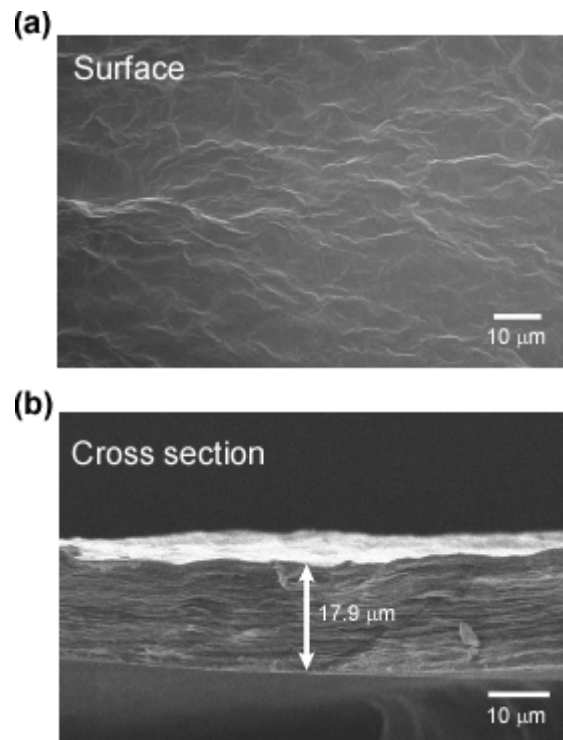


Figure 5-2. SEM images of (a) surface and (b) cross section of GO paper.

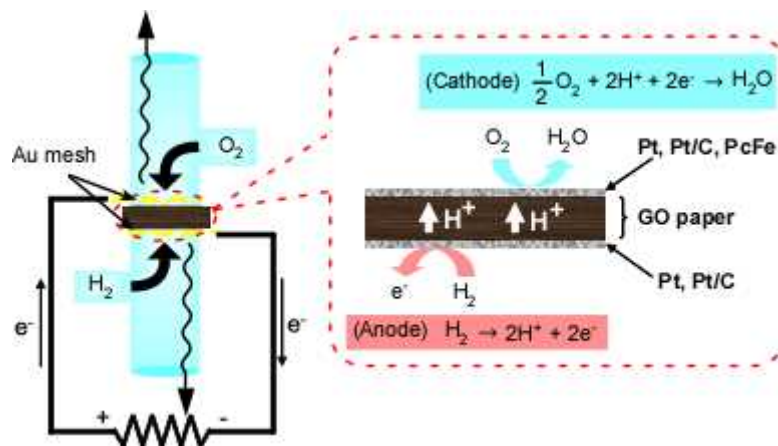


Figure 5-3. Model of the GOFC and test chamber.

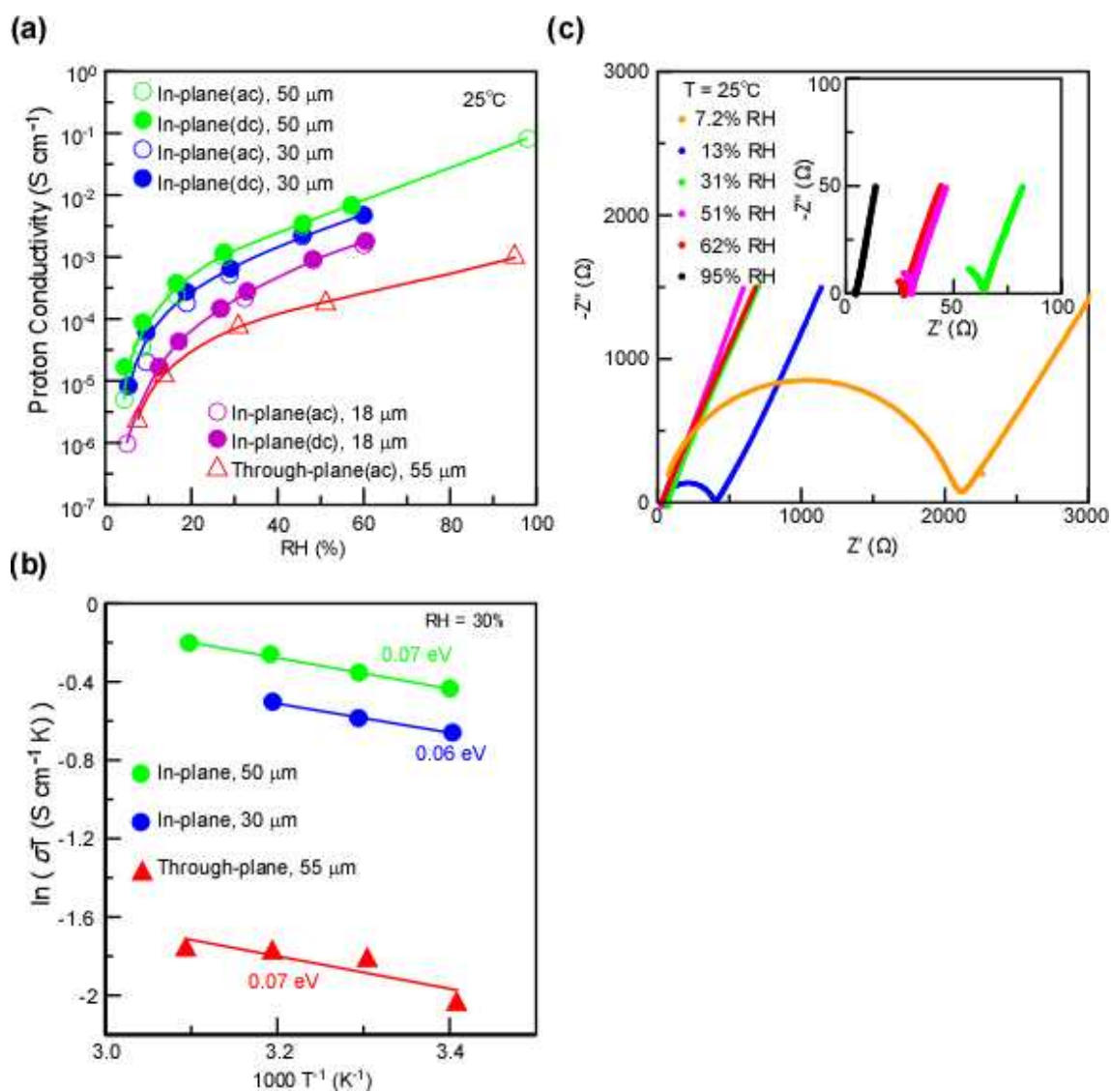


Figure 5-4. (a) In-plane and through-plane proton conductivities of the GO papers at $25^{\circ}C$. (b) Arrhenius plots of the proton conductivities, σ , of GO papers at 30% RH. The thicknesses of the GO papers are shown. (c) Typical Cole-Cole plots of the impedance spectra of the GO paper for the through-plane proton conductivity at $25^{\circ}C$ and 7.2~95% RH.

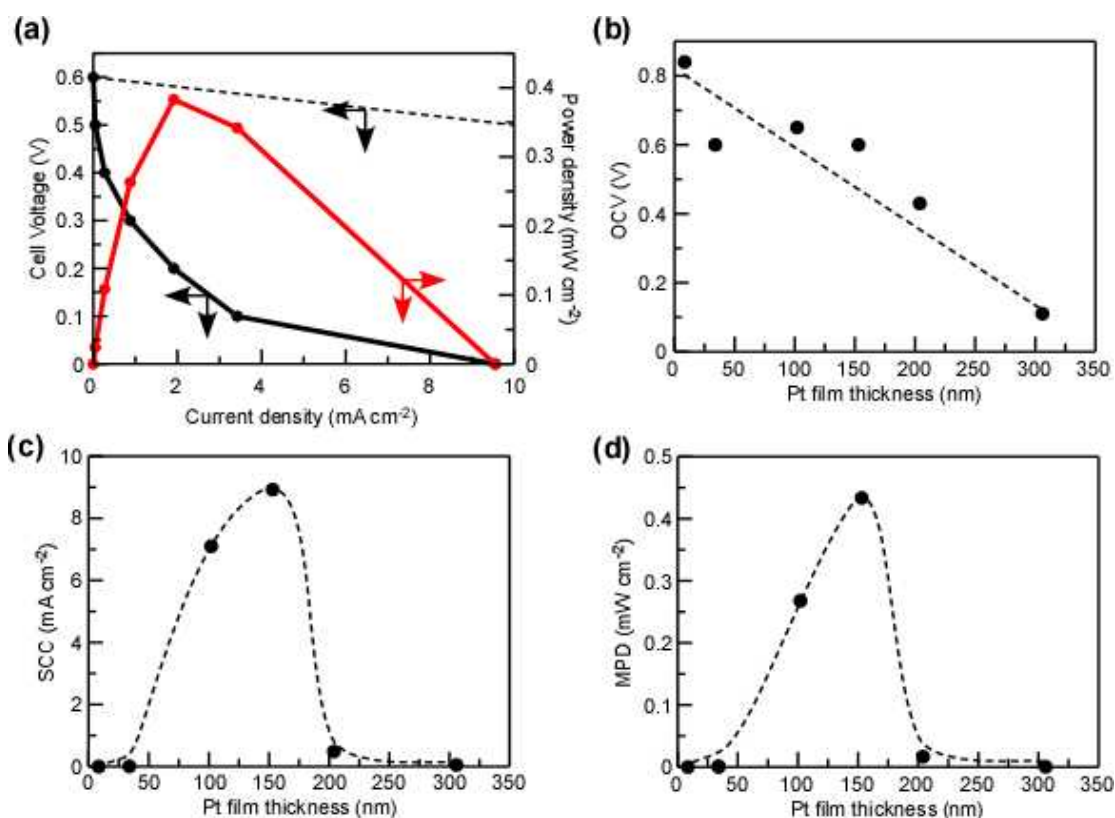


Figure 5-5. (a) Polarization (left Y axis) and power density (right Y axis) curves for the GOFC with the sputtered Pt electrodes at 23°C. Dependences of (b) OCV, (c) SCC, and (d) MPD on Pt film thickness of the GOFC at 25°C.

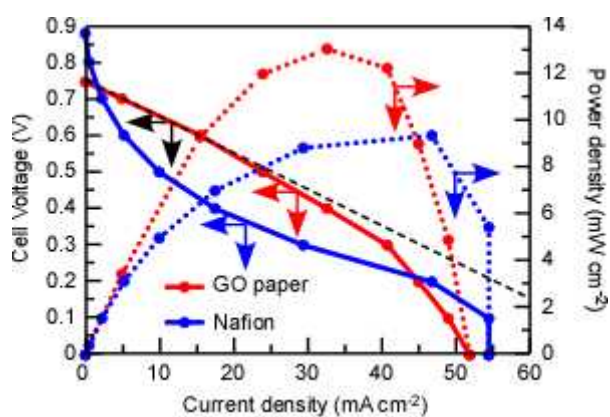


Figure 5-6. Polarization (left Y axis) and power density (right Y axis) curves for the MEA composed of GO electrolyte and Pt/C electrodes (red) and that composed of Nafion electrolyte and Pt/C electrodes (blue) at 25°C.

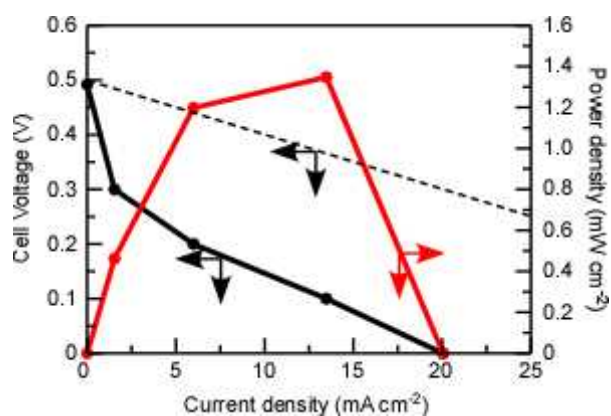


Figure 5-7. Polarization (left Y axis) and power density (right Y axis) curves for the GOFC consisting of nano-sized GO paper with the sputtered Pt electrodes at 24°C.

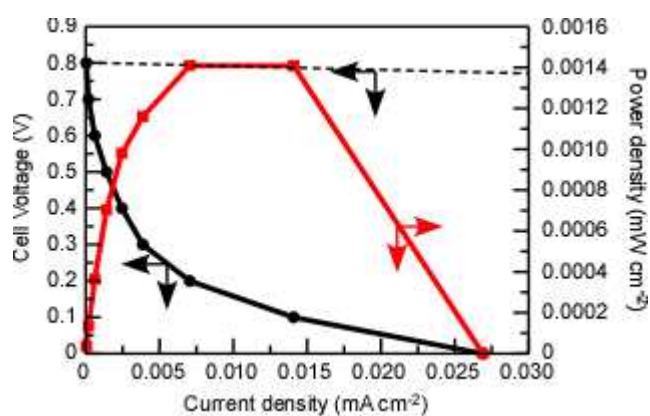


Figure 5-8. Polarization (left Y axis) and power density (right Y axis) curves for the GOFC with the PcFe/rGO/TiO₂ hybrid as cathode and the sputtered Pt as anode at 23°C.

CHAPTER 6

Graphene Oxide Lead Battery (GOLB)

Overview

Graphene oxide (GO) has a high proton conductivity and sulfuric acid affinity, which suggests that GO paper can be used as an electrolyte substitute for sulfuric acid in lead-acid batteries. In this chapter, we report a new type of graphene oxide lead battery (GOLB) that uses a GO paper electrolyte, i.e., a dry lead battery. The GOLB has a very thin (~2 mm) cell size, and the GO paper electrolyte has a thickness of 70 μm . The stable charge–discharge cycles of the GOLB indicate that it is suitable for its use as a small-sized, portable battery comparable to Li-ion batteries.

6.1 Introduction

Lead-acid batteries containing a H_2SO_4 solution have a long history of use as vehicle batteries. This is mainly attributed to their excellent cost performance, high voltage for a single cell (2 V), and nonmemory effect [1–4]. However, it cannot be used as a small-sized, portable cell battery because it has a H_2SO_4 solution as an electrolyte and low gravimetric energy density. These disadvantages may be overcome if a proton solid electrolyte is used instead of the H_2SO_4 solution. This would allow for the fabrication of very small or very thin (less than a few millimeters) cells without solution leakage, i.e. a dry cell.

Graphene oxide (GO) has a high proton conductivity [5–8] that can be used as an electrolyte in H_2/O_2 fuel cells, which are also known as graphene oxide fuel cells [9]. Although the proton conductivity of GO is lower than that of Nafion [6, 10], the total resistance of the electrolyte decreases with the use of 10- μm -thick films. In fact, 0.1- μm -thick films can be easily manufactured with GO

paper ^[11]. Moreover, from a commercial viewpoint, GO has the benefit of low cost compared to Nafion.

In this chapter, a small-sized and dry lead battery that uses GO paper, hereafter termed as graphene oxide lead battery (GOLB), as the electrolyte instead of a H₂SO₄ solution is presented along with data on its initial performance. The results indicate that the GOLB may serve as a substitute for practical field use in Li-ion batteries.

6.2 Experimental

6.2-1 Synthesis of GO paper

GO was prepared from natural graphite powder (special grade reagent, Wako Ltd.) using Hummers method ^[12]. Graphite powder (2.0 g), NaNO₃ (2.0 g, special grade reagent, Wako Ltd.), and 98% H₂SO₄ (92 mL, special grade reagent, Wako Ltd.) were mixed at 0°C in an ice water bath. KMnO₄ (12 g, special grade reagent, Wako Ltd.) was added to the mixture. The reaction mixture was removed from the ice water bath and stirred for 45 min at 95°C to oxidize the graphite powder. The resulting mixture was diluted with distilled water, and 30% H₂O₂ (5 mL, special grade reagent, Wako Ltd.) was added to neutralize any remaining KMnO₄. The product was washed with 5% HCl (special grade reagent, Wako Ltd.) and centrifuged several times at 3000 rpm to remove any excess HCl. The product was dried in an oven at 50°C for 1 day. The dried paper product was used as the GO paper (Figure 6-1).

6.2-2 Fabrication and tests of the GOLB

The GO paper was used as the electrolyte in GOLB (Figure 6-2(a)). The Pb powders in the active mass were obtained by shaving a Pb plate (99.99%, The Nilaco Corporation). The particle sizes were 50~100 μm (Figure 6-3(a)). The Pb paste, which served as the active mass, was prepared

by mixing the Pb powder (60 mg) with 6 M H₂SO₄ (12.5 μL), which was necessary for electrochemical reactions. A lignin (chemically pure reagent, Nacalai Tesque Ltd.) aqueous solution (1 mL, 10 g L⁻¹) was mixed with 6 M H₂SO₄ (9 mL), and then the Pb paste was further prepared by mixing the Pb powder (60 mg) with the lignin mixture (12.5 μL), which served as the negative active mass. The paste was interposed between the GO paper and Pb plate and served as the electrode (Figure 6-3(b)). The apparent areas of the active mass (Pb paste) in contact with the GO paper were 1 cm². All battery tests were performed at room temperature. The cell was charged at 10 mA cm⁻² for 20 min and then maintained in an open circuit for 1 min before the next discharge step. Discharge was conducted at 1.0 mA cm⁻² down to 1.8 V unless otherwise stated, and the experimental scheme is shown in Figure 6-4 (especially in the case of H₂SO₄ addition in GOLB). The discharge tests at different current densities were conducted from 0.1 to 1.0 mA cm⁻² to evaluate the dependence of capacitance on discharge current density.

6.3 Results and Discussion

Figure 6-2 shows schematics and photographs of the GOLB and its parts. Figure 6-1 shows SEM micrographs of the GO papers serving as the electrolyte. The thicknesses were in the range of 50~80 μm, and their resistances were around 10⁻² Ω for proton conduction at room temperature in the GOLB. This value is not problematic for electrolyte resistance when the GOLB is used; for example, the IR drop by the GO electrolyte will be around 10 mV when a current of 1 A flows in the GOLB. Figure 6-5 illustrates the models of the total reactions occurring in the GOLB. In the active mass paste consisting of Pb metal powders mixed with a H₂SO₄ solution, the electrode reactions at the interface of Pb/H₂SO₄ occur during both the discharge and charge steps. The products during the charge step are Pb (negative electrode) and PbO₂ (positive electrode) and PbSO₄

during the discharge step. The proton moves through the GO paper (through a plane), and the moving direction depends on the charge and discharge. In conclusion, all of the electrochemical reactions occur in the whole regions of the active masses, and the GO only acts as the proton conductor.

Figures 6-2 show a structural schematic and photograph of the GOLB, respectively. The total thickness of the present GOLB is very low, ranging from 1.5 to 2.0 mm. However, a much thinner cell can be obtained if the Pb is plated to be thinner than 0.2 mm, and/or smaller Pb particles are used as the current collector and active mass. Oozing of the H₂SO₄ solution in the active mass was not observed because it was only present in a limited amount. This remained true even when pressure was applied to both electrode sides. Thus, the present GOLB is a dry lead battery, and can be used as a very thin and small portable battery in small electric devices.

Figure 6-4 shows the various performances of the present GOLB in the initial charge–discharge cycles. Figure 6-4(a) shows typical charge and discharge curves when charge and discharge were carried out at 10 mA cm⁻² and 1.0 mA cm⁻², respectively. Clear discharge curves were observed at 2.2 V, and these same curves are also observed for a typical lead-acid battery [13]. Figure 6-4(b) shows the discharging time (capacity) as a function of the cycle number. Initially, the capacity increased, but then it decreased after approximately four cycles. The initial increase was attributed to the formation of the electrochemical active species, i.e., Pb, PbO₂, and PbSO₄, on the Pb particle surfaces in the active mass, and the decrease was attributed to their change to non-active forms after four cycles. The addition of small amounts of a H₂SO₄ solution (6 M, 6.25 μL) resulted in performance recovery, as shown in Figure 6-4(b). It is likely that almost all of the H₂O and SO₄²⁻ in the Pb paste will be consumed or sulfation will occur (as stated below) during the initial activation processes, resulting in non-activation from the lack of species required for the electrochemical reactions of Pb/PbSO₄ and Pb/PbO₂. The addition of the H₂SO₄ solution allows for the recovery of

these species. Again, oozing of the added H₂SO₄ solution was not observed. Relatively stable charge and discharge curves were observed after addition; as shown in Figure 6-4(b). Results similar to those reported above were obtained for the lead-acid battery and are shown in Figure 6-4(b). 6 M H₂SO₄ solution was used as the electrolyte instead of the GO paper, and the other compositions and conditions were the same as those of the present GOLB. In this case, automatic recovery was observed because of the presence of enough H₂SO₄ solution.

On the other hand, the addition of lignin into the active mass in the negative electrode brought about an automatic recovery after a similar non-activation at around four cycles. That is, the above non-activation phenomenon will be mainly based on that of the negative electrode, probably sulfation (crystallization of PbSO₄), because lignin suppresses the sulfation [14]. In conclusion, the present GOLB shows the same performance as that of a conventional lead-acid battery; although, some improvements in the activemasses and structures are necessary for practical use.

Figure 6-4(c) shows the dependence of the cell capacity as a function of discharge current density. The capacity barely decreased with an increase in current density. The gravimetric energy density of the present cell was calculated to be a few Wh kg⁻¹ (1.0 mA cm⁻² discharge), which was lower than that of a commercial lead-acid battery (30~40 Wh kg⁻¹). However, the value can easily be increased if active masses with high specific surface areas (very small Pb and/or PbO₂ particles) and additives, as well as lignin that promote activation are used in the present GOLB. The present GOLB is very promising for use as a small-sized, portable type battery comparable with Li-ion batteries since the H₂SO₄ electrolyte, which typically causes solution leakage, is barely used.

6.4 Conclusions

Graphene oxide (GO) paper with proton conduction was used as a solid electrolyte to

replace the H_2SO_4 solution electrolyte in a lead acid battery. The present graphene oxide lead battery (GOLB) consists of a small-sized $\text{PbO}_2/\text{PbSO}_4//\text{GO}//\text{PbSO}_4/\text{Pb}$ cell and does not have the disadvantage of solution leakage (dry cell), making it attractive for use in small-sized, portable cells. Good performance was observed in the initial charge-discharge cycles. Thus, the developed GOLB can be used as a small-sized cell, although some improvements in the active mass are necessary to increase the gravimetric power density.

References

- [1] K. Nakamura, M. Shiomi, K. Takahashi, M. Tsubota, *J. Power Sources* **1996**, 59, 153.
- [2] M. Shiomi, T. Funato, K. Nakamura, K. Takahashi, M. Tsubota, *J. Power Sources* **1997**, 64, 147.
- [3] D. Pavlov, P. Nikolov, T. Rogachev, *J. Power Sources* **2011**, 196, 5155.
- [4] D. Pavlov, *Lead-Acid Batteries: Science and Technology*, Elsevier, **2011**.
- [5] W. Gao, N. Singh, L. Song, Z. Liu, A. L. M. Reddy, L. J. Ci, R. Vajtai, Q. Zhang, B. Q. Wei, P. M. Ajayan, *Nat. Nanotech.* **2011**, 6, 496.
- [6] H. Zarrin, D. Higgins, Y. Jun, Z. W. Chen, M. Fowler, *J. Phys. Chem. C* **2011**, 115, 20774.
- [7] M. R. Karim, K. Hatakeyama, T. Matsui, H. Takehira, T. Taniguchi, M. Koinuma, Y. Matsumoto, T. Akutagawa, T. Nakamura, S. Noro, T. Yamada, H. Kitagawa, S. Hayami, *J. Am. Chem. Soc.* **2013**, 135, 8097.
- [8] M. Koinuma, C. Ogata, Y. Kamei, K. Hatakeyama, H. Tateishi, Y. Watanabe, T. Taniguchi, K. Gezuhara, S. Hayami, A. Funatsu, M. Sakata, Y. Kuwahara, S. Kurihara, Y. Matsumoto, *J. Phys. Chem. C* **2012**, 116, 19822.
- [9] H. Tateishi, K. Hatakeyama, C. Ogata, K. Gezuhara, J. Kuroda, A. Funatsu, M. Koinuma, T. Taniguchi, S. Hayami, Y. Matsumoto, *J. Electrochem. Soc.* **2013**, 160, F1175.
- [10] K. Ravikumar K. Scott, *Chem. Commun.* **2012**, 48, 5584.
- [11] R. R. Nair, H. A. Wu, P. N. Jayaram, I. V. Grigorieva, A. K. Geim, *Science* **2012**, 335, 442.
- [12] W. S. Hummers Jr., R. E. Offeman, *J. Am. Chem. Soc.* **1958**, 80, 1339.
- [13] A. Czerwinski, S. Obrebowski, J. Kotowski, Z. Rogulski, J. Skowronski, M. Bajsert, M. Przystalowski, M. Buczkowska-Biniecka, E. Jankowska, M. Baraniak, J. Rotnicki, M. Kopczyk, *J. Power Sources* **2010**, 195, 7530.
- [14] I. Ban, Y. Yamaguchi, Y. Nakayama, N. Hirai, S. Hara, *J. Power Sources* **2002**, 107, 167.

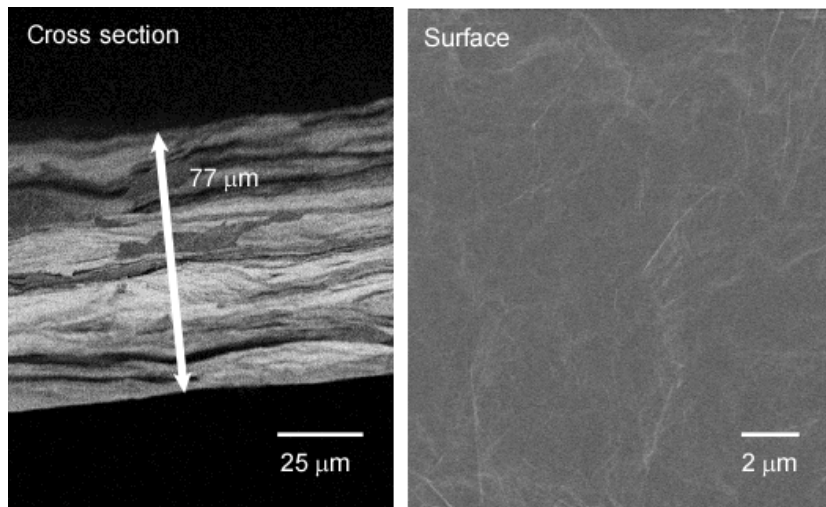


Figure 6-1. SEM images of the cross section (left) and surface (right) of GO paper.

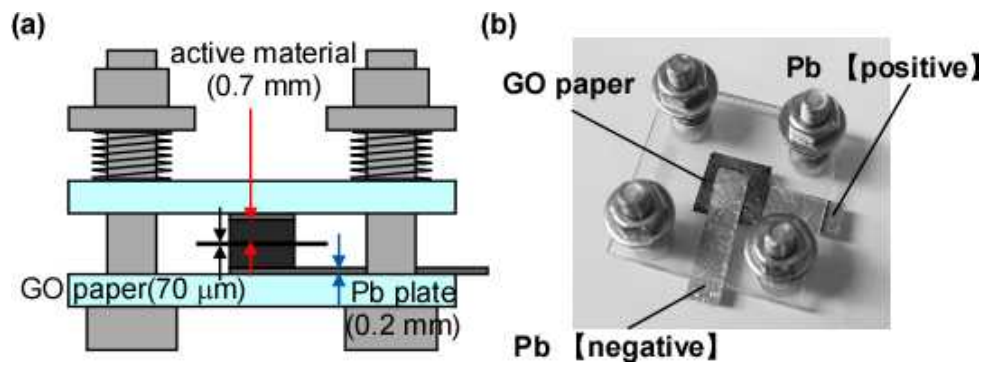


Figure 6-2. (a) Structural schematic of GOLB. (b) Photograph of GOLB.

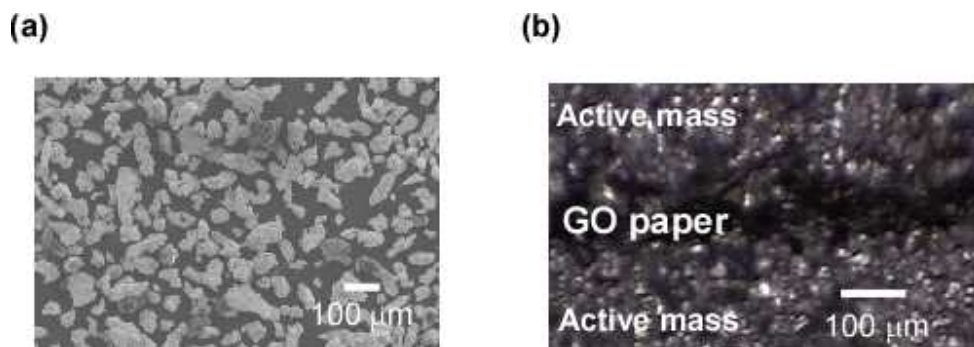


Figure 6-3. (a) SEM images of Pb powders used in the active mass. (b) Reflection optical microscope image of the cross section of GOLB.

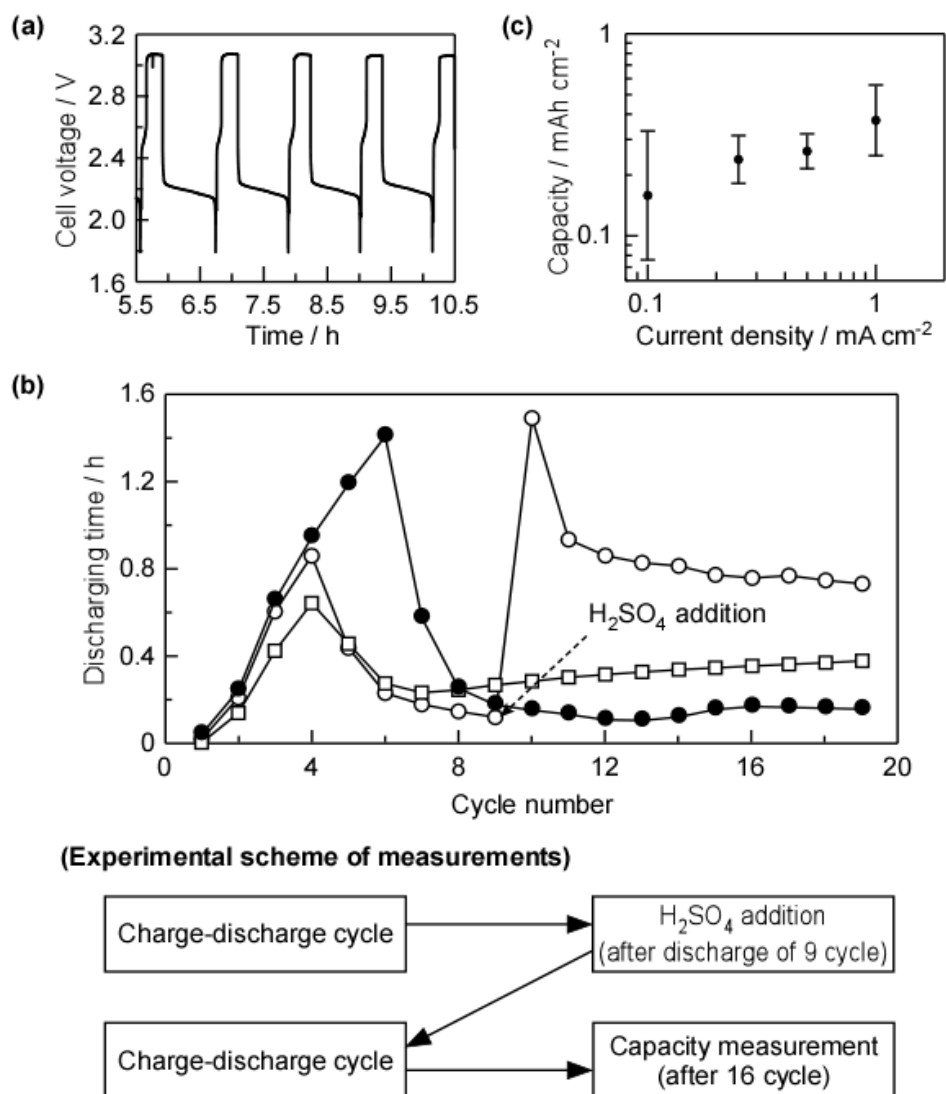


Figure 6-4. (a) Cell voltage vs. time response for GOLB after 12 charge-discharge cycles (after the addition of H₂SO₄). The cell was discharged at 1.0 mA cm⁻² down to 1.8 V. (b) Cycle performance of GOLB. Open and closed symbols correspond to GOLB and conventional lead-acid battery respectively. The arrow indicates the addition of 6 M H₂SO₄ into both Pb paste active masses. Open square symbol is the case of the lignin added cell. (c) Dependence of discharge capacity on discharge current density for GOLB. The tests were conducted after 16 discharge/charge cycles.

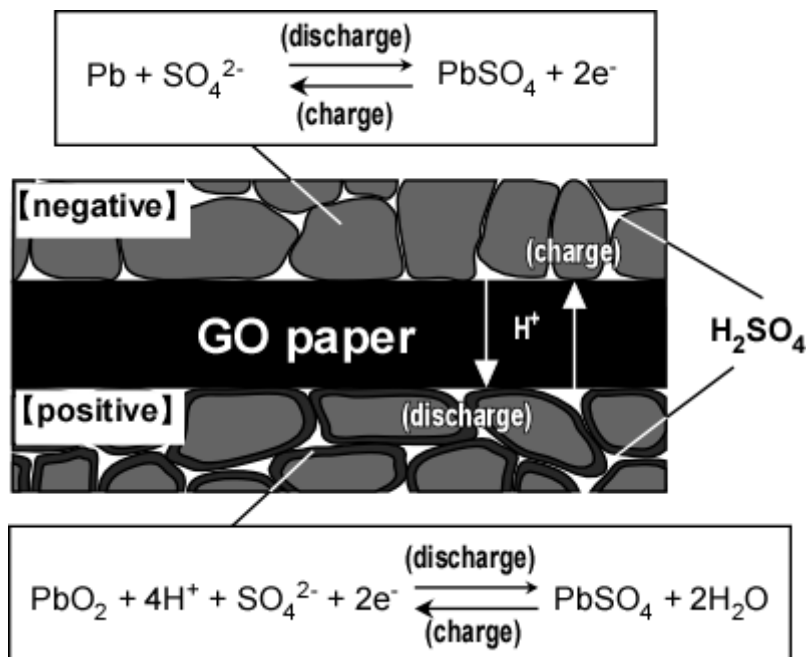


Figure 6-5. Illustrations of the models of the active masses and the overall electrochemical reactions that occurred in the GOLB.

CHAPTER 7

7. General conclusions

GO has traditionally served as a precursor for graphene, but is gradually attracting chemists for its own unique chemical properties due to its oxygen functional groups. Additionally, GO also can easily combine various nanomaterials. Moreover, reduced GO (rGO) is suitable for various electrodes materials because rGO is electronic conductor.

In this present study, we investigated its electrochemical properties, especially electrochemical capacitance and ORR properties, and aimed to develop new electrochemical device.

The summary of each chapter is described as follows:

- **Chapter 1** narrated the general backgrounds, preparation method, electrochemical properties, and application of GO.
- **Chapter 2** presented that the electrochemical properties of GO prepared by the facile one-step electrochemical method. This method can easily control oxidation degree of GO by adjusting the applied voltage and electrolysis time. The reduced GO electrodes exhibited high electrochemical capacitance and high electrocatalytic activity for ORR, and n-type semiconductor. We found these excellent electrochemical properties of rGO were due to the CH defects and/or OH groups transformed from COC groups at the basal plane of GO sheet. Moreover, these electrochemical properties were enhanced by electrodepositing metal oxides or hydroxides on rGO electrodes. Thus, this present method is very useful for preparing oxidation-controlled GO, and therefore will be useful in many applications.
- **Chapter 3** presented that we succeeded to research about effect of the reduction method and the electrochemical oxidation/reduction cycle on the electrochemical capacitance of GO. We analyzed GO and rGO by XPS and deconvoluting the C1s binding energies of the functional groups for the first time. The CH defects significantly affected the electrochemical capacitance.

We also discovered that the mechanism for oxidation/reduction cycle. COC groups were formed from GC by the first electrochemical oxidation. CH defects were produced from COC groups on GO by electrochemical reduction and then C=C bonds were produced from CH defects by electrochemical re-oxidation. The reversible reaction ($2\text{CH} \rightleftharpoons \text{C} = \text{C} + 2\text{H}^+ + 2\text{e}^-$) occurred for the electrochemical oxidation/reduction cycle.

- **Chapter 4** presented that we developed the new self-assembly pathway to FePc/rGO hybrid with excellent ORR activity. The Fe ion in an FePc was anchored by oxygen functional groups to form FePc nano-sized domains in the initial self-assembly step. The FePc/rGO hybrid catalysts exhibited more excellent ORR activity than that of Pt/C in alkaline solution owing to efficient electrochemical coupling between FePc and rGO, which was investigated. The self-assembly strategy could be broadly extended to the preparation of new hybrid materials comprising GO and nanomaterials exhibiting various functional properties.
- **Chapter 5** presented development of GOFC. We demonstrated that the performance of the GOFC with GO paper as electrolyte at a low *RH* and room temperature. The GOFC with Pt/C electrodes exhibited better fuel cell performance than a fuel cell with Nafion electrolyte and Pt/C electrodes. In the case of using nano-sized GO as electrolyte, the current density was increased due to increasing of active surface area which is three-phase interface; electrode, gas, and GO electrolyte. In the case of using Pt-free catalyst, i.e. FePc/rGO, as oxygen electrode, the large OCV can be obtained in that GOFC, while the current density must be increased for applications. These results suggested that it will be possible to open up fabricating cost-effective GOFC.
- **Chapter 6** presented development of GOLB. We fabricated small-sized dry GOLB with GO paper as solid electrolyte. The GOLB exhibited comparable performance to lead battery using H₂SO₄ solution electrolyte. Thus, GOLB suggested the high potential for development of a

portable cell.

We believe that GO have the potential to open up many electrochemical field such as supercapacitors, fuel cells, and secondary batteries.

ACKNOWLEDGEMENTS

I would like to express my sincerest thanks to **Professor Yasumichi Matsumoto** for his invaluable comments and suggestions, and his encouragements through the period of this study.

I would like to express my appreciation to Dr. Michio Koinuma and Assistant Professor Takaaki Taniguchi for their advices and encouragements.

I would also like to thank to other member of my committees: Professor Masato Machida and Professor Shinya Hayami.

I would like to express my deepest appreciation to Professor Seiji Kurihara, Associate Professor Yukihiro Yokoi, and Associate Professor Masahiro Hara for their advices and encouragements.

I would like to express my deepest appreciation to Ms. Kiyomi Tahara Secretary in this laboratory for her advices and assistance.

I am deeply thankful to Mr. Kazuto Hatakeyama, Ms. Chikako Ogata, Ms. Asami Funatsu, Mr. Shinsuke Miyamoto, Mr. Yusuke Watanabe, Mr. Yuki Kamei, Mr. Kengo Gezuhara, Mr. Tubasa Koga, Mr. Jun Kuroda, and Mr. Shuhei Kawakita for their encouragement and assistance.

I am also thankful to students in Matsumoto Laboratory.

Finally, I deeply thank my parents: Mr. Katsuhiro Tateishi and Ms. Ryoko Tateishi, grandparents: Mr. Yoshio Tateishi and Ms. Sueno Tateishi, brother: Mr. Kazuya Tateishi, sister: Ms. Rina Tateishi, and many friends for their supports and hearty encouragements through my student life.

Kumamoto

2015

Hikaru Tateishi